Addis Ababa University
School of Graduate Studies
College of Technology and Built Environment
School of Electrical and Computer Engineering

Optimizing Operation and Control Strategies for Distributed Energy Resource-Integrated Microgrids: Evolutionary and Neuroevolutionary-Based Decentralized Primary Control in Islanded Mode

Yared Bekele Beyene

A dissertation submitted in partial fulfillment of the requirements
for the degree of Doctor of Philosophy
in
Power Engineering

Supervisor: Dr.-Ing. Getachew Biru Worku
Co-supervisor: Prof. Lina Bertling Tjernberg

July 2025

Approval

It is certified that the contents and form of the thesis entitled "**Optimizing Operation and Control Strategies for Distributed Energy Resource-Integrated Microgrids: Evolutionary and Neuroevolutionary-Based Decentralized Primary Control in Islanded Mode**" submitted by **Yared Bekele Beyene** have been found satisfactory for the requirement of the degree of Doctor of Philosophy in Power Engineering.

Supervisor: **Dr.-Ing. Getachew Biru Worku**

Signature: _____

Date: _____

Co-supervisor: **Prof. Lina Bertling Tjernberg**

Signature: _____

Date: _____

External Examiner: **Prof. Henry Louie**

Signature: _____

Date: _____

Internal Examiner: **Dr. Getachew Bekele Beyene**

Signature: _____

Date: _____

Abstract

The accelerating global climate crisis—combined with the uneven distribution of fossil fuel resources, rising oil prices, increasing demand for modern energy systems, and the global shift toward low-carbon economies—has necessitated a fundamental transformation in how energy is produced, distributed, and consumed. Renewable energy sources (RES) such as solar and wind are central to this transition. However, their integration into power systems presents persistent challenges due to intermittency, decentralization, and the limitations of traditional grid infrastructure.

Microgrids (MGs) have emerged as a flexible and resilient solution for the decentralized integration of distributed energy resources (DER), playing a key role in advancing intelligent, low-carbon power networks. As the demand for sustainable, secure, and responsive energy systems grows globally, MGs—especially those incorporating DER and hydrogen technologies—are becoming indispensable components of the evolving energy landscape.

While MGs hold promise for energy resilience and sustainability, their implementation faces challenges like high initial capital investment for infrastructure, technical complexity in integrating diverse DER, and interoperability issues with legacy grids. These barriers affect stable operation and the broader scalability of MG solutions. Accordingly, this research is directed toward addressing these multifaceted issues to enable more effective localized generation and control, advancing sustainability, energy independence, and resilience.

The study begins by developing and evaluating integrated strategies to overcome the technical, economic, and environmental hurdles associated with MG deployment as a first objective. It focuses on the optimized design of a sustainable MG architecture that incorporates solar, wind, and hydrogen-based storage alongside sector coupling mechanisms. Through system-level analysis, the research underscores hydrogen's pivotal role in increasing grid flexibility, compensating for the intermittency of renewable resources, and enhancing long-term energy security. This foundational investigation affirms the value of MGs in supporting decarbonization and improving energy resilience through hydrogen-enabled sector coupling and cross-sectoral integration.

In regions where utility grids are unreliable—characterized by frequent outages—MGs are often required to operate in islanded mode. While islanded operation enhances energy autonomy and resilience, it also introduces significant technical complexity. Without main grid support, islanded MGs must coordinate energy balance and economic operation across both short-term dynamics and long-term planning. Moreover, islanded MGs dominated by converter-interfaced DERs face considerable challenges in maintaining voltage and frequency stability under dynamic load and generation conditions. These operational challenges highlight the need for robust and well-coordinated control strategies specifically designed for islanded MG environments.

In response, the subsequent phase of the thesis develops and evaluates advanced decentralized primary control strategies for islanded MGs. Within this framework, two distinct approaches are pursued: a virtual complex impedance-based method, which enhances transient response, system stability, and power-sharing accuracy by shaping the converter's output impedance; and a computationally guided optimization framework, which systematically tunes control parameters to better coordinate with the dynamic characteristics of the interfacing filter and electrical network. These strategies are grounded in a detailed analysis of VSCs, including their control architectures and interfacing filters, which are vital for maintaining system stability and ensuring power quality.

Building on these strategies, the final phase of the thesis introduces an Adaptive Hybrid PSO-Embedded Genetic Algorithm (AHPEGA) for the neuroevolutionary training of Multilayer Perceptron Controllers (MLPCs) in VSC-based islanded MG. This approach combines the global search efficiency of GA with the fine-tuning capabilities of PSO to dynamically optimize both the weights and biases, as well as hyperparameters, of the neural network—resulting in improved convergence and generalization in nonlinear control tasks.

Overall, this thesis presents a comprehensive, multi-layered approach to MG control—encompassing sustainable system design and advanced decentralized control strategies—and delivers scalable, sustainable, and computationally guided solutions for resilient operation in islanded mode. These contributions establish a foundation for advancing intelligent control in islanded MGs integrated with renewable resources, thereby supporting the broader transition toward robust, efficient, and sustainable power systems.

Keywords: Power grid, Microgrids, FCEVs, Electrolytic hydrogen, Emission reduction, Renewable energy curtailment, Islanded operation, Virtual complex impedance, Control parameter optimization, PSO-MLPNN, PSO-embedded GA, Neuroevolutionary training, Multilayer Perceptron Controllers (MLPCs)

Acknowledgments

Although my desire to continue my studies began immediately after completing my second degree, pursuing this path required more than personal ambition—it demanded guidance, encouragement, and support from others. I am profoundly grateful to Dr.-Ing. Getachew Biru and Dr. Getachew Bekele, who have been not only my instructors but also my mentors and supervisors. Their steadfast support and encouragement enabled me to compete for and join the AAU-Sida Project under the Ph.D. Program in Electrical Power and Control Engineering. I sincerely thank them for their guidance, belief in my potential, and invaluable mentorship.

I am incredibly grateful to my supervisors, Dr.-Ing. Getachew Biru and Prof. Lina Bertling Tjernberg, for their unwavering support, patience, and dedication in guiding and reviewing my work. This achievement would not have been possible without their commitment. I owe special thanks to Prof. Lina Bertling Tjernberg, whose support extended far beyond academic supervision. She has been a true mentor and friend—offering thoughtful insights, patiently reviewing my work, and consistently providing constructive feedback. Her kindness, humility, and encouraging nature made our collaboration both positive and inspiring. For her mentorship, friendship, and steadfast belief in my potential, I am sincerely thankful.

I would like to express my sincere appreciation to the faculty of the Division of Electrical Power and Energy at KTH. The division's professional and supportive research environment played a significant role in my development as a research student. I am also grateful to the staff and Power Chair of the School of Electrical and Computer Engineering at Addis Ababa University for their ongoing support and collaboration. Special thanks go to Dr. Mengesha Mamo, Principal Investigator of the AAU-Sida Project under the PhD Program in Electrical Power and Control Engineering, for his exemplary leadership and unwavering support. I also acknowledge the management and administrative teams of the School of Electrical and Computer Engineering and the College of Technology and Built Environment of AAU for their efficient coordination of project logistics and financial processes. Lastly, I extend my heartfelt gratitude to the Swedish International Development Cooperation Agency (SIDA) for funding this research through Addis Ababa University's research, training, and capacity-building program.

I am also deeply grateful to my AAU/KTH colleagues—Kena Likassa, Mesfin Tilahune, Teshome Hambissa, Firehiwot Girma, Henok Girma, Alebachew Tilahun, Micheal Getachew—as well as all the AAU/Chalmers students, for their kindness, support, and for creating a warm and welcoming environment throughout my time abroad. I sincerely appreciate the care and companionship they offered, especially during challenging times. I would also like to acknowledge all those with whom I shared the office over the years at KTH—their presence made the research environment more enjoyable and collegial.

To my family, whose sacrifices and unwavering support have brought me to this point—I am deeply grateful. You have empowered me to reach higher while keeping me anchored in love and care. My heartfelt thanks go especially to my wife, Feyise Buruse, for managing all family responsibilities in my absence; to my son, Milki Yared, born at the beginning of this journey; and to my niece, Feyise Humne, who has been the pillar holding our family together throughout these years.

Declaration

This Ph.D. dissertation is a presentation of my own work, and any material used from other sources has been clearly identified, properly acknowledged, and cited.

Signed …….. Date ……..

Yared Bekele Beyene

Contents

List of Tables

List of Figures

List of Abbreviations

AIP	Adama Industrial Park
AHPEGA	Adaptive Hybrid PSO-Embedded GA
ACO	Ant Colony Optimization
AI	Artificial Intelligence
BESS	Battery Energy Storage Systems
BOA	Butterfly Optimization Algorithm
CNN	Convolutional Neural Network
CS	Cuckoo Search
CSC	Current Source Converter
CC	Cycle-Charging
DL	Deep learning
DRL	Deep Reinforcement Learning
DoD	Depth of Discharge
DG	Distributed Generator
DRER	Distributed Renewable Energy Resources
EMS	Energy Management Systems
ESS	Energy Storage Systems
EEU	Ethiopian Electric Utility
FCEV	Fuel Cell Electric Vehicle
GA	Genetic Algorithm
GOA	Grasshopper Optimization Algorithm
GWO	Grey Wolf Optimization
HHO	Harris Hawks Optimization
HOMER	Hybrid Optimization Model for Multiple Energy Resources
HRES	Hybrid Renewable Energy Systems
ICT	Information and Communication Technologies
IEA	International Energy Agency
IGBT	Insulated Gate Bipolar Transistors
IRENA	International Renewable Energy Agency

LCOE	Levelized Cost of Energy
LP	linear programming
LF	Load following
LC	Local Controller
ML	Machine Learning
MG	Microgrid
MILP	Mixed-integer Linear Programming
MLPC	Multilayer Perceptron Controller
MLP	Multilayer Perceptron
PSO	Particle Swarm Optimization
PV	Photovoltaic
PCC	Point of Common Coupling
PEC	Power Electronic Converter
PEME	Proton Exchange Membrane Electrolyzer
PEMFC	Proton Exchange Membrane Fuel Cells
RESs	Renewable Energy Sources
SCR	Short-Circuit Ratio
SA	Simulated Annealing
SOC	State of Charge
TS	Tabu Search
THD	Total Harmonic Distortion
UPQC	Unified Power Quality Conditioner
VRE	Variable Renewable Energy
VSC	Voltage Source Converter
WT	wind turbine

Chapter 1

Introduction

1.1 Evolving Electric Power Grid

The global climate change crisis, driven by human-caused greenhouse gas emissions, poses one of the most formidable challenges humanity has ever faced. These emissions come predominantly from the energy sectors, accounting for approximately 75 % of the total [1]. Notably, electricity and heat production is a major contributor to these emissions. Consequently, aligning with the recommendations of the International Energy Agency (IEA) requires a radical transformation in energy production, transportation, and consumption. Rather than relying on fossil fuels, the transition to renewable energy sources (RES), including wind, solar, bioenergy, geothermal, and hydro, plays a pivotal role in the achievement of sustainable energy goals [2], [3]. Attaining this transition requires collaborative efforts among governments, development partners, and the private sector as they invest in innovative strategic plans and cutting-edge technologies to unlock the full potential of renewable energy.

In the coming years, renewables, particularly wind and solar photovoltaic (PV) technologies, are expected to account for an increasingly larger proportion of global electricity generation [1], [2]. These technologies play a key role in reducing carbon emissions across the transportation, buildings, and industry sectors. Moreover, the transition to renewables is essential for enabling the production of low-emission fuels such as hydrogen — particularly for hard-to-electrify sectors like heavy industry, aviation, shipping, and long-haul transport, where direct electrification remains technically or economically challenging [3], [4].

To support the global transition toward a cleaner and more resilient energy future, the electrical power system is evolving into a Smart Grid—an intelligent infrastructure designed to meet climate targets, integrate high shares of renewable energy, and enhance reliability and efficiency across the network [5]. At the core of this evolution is the deployment of information

and communication technologies (ICT), which enable real-time coordination between generation and consumption. The Smart Grid aims to deliver clean, secure, and efficient electricity through a paradigm that is decarbonized (minimizing reliance on carbon-intensive generation), decentralized (integrating distributed energy resources), digitized (utilizing data-driven automation), and democratized (empowering end-users to actively participate in energy production and decision-making) [6], [7]. These capabilities facilitate competitive electricity trading among producers and consumers, ensure reliable supply for critical loads, reduce operational costs, modernize aging infrastructure, and expand energy access to underserved communities [8], [9]. Within this context, microgrids (MGs) are key enablers of smart grids, providing a flexible framework for managing distributed energy resources (DER)—including renewable and non-renewable distributed generators, energy storage systems (ESS), and local electrical loads—by coordinating them as a locally controlled energy system that can operate either in connection with the main grid or independently [10], [11]. As MGs continue to evolve, they are increasingly valued for enabling emerging energy technologies such as green hydrogen, next-generation battery systems, and vehicle-to-grid (V2G) integration. Among these, green hydrogen holds particular promise for decarbonizing sectors that are difficult to electrify. Produced through electrolysis powered by renewable energy, it offers significant emissions reductions in industries such as heavy transport and manufacturing [3], [4].

While these technical advancements are crucial, realizing the expanded role of MGs—not only as decentralized energy nodes but also as integration platforms bridging multiple energy sectors—demands enabling policies, adaptive regulatory frameworks, and supportive market designs that foster flexibility, resilience, and innovation. As the global push for sustainable, intelligent, and robust energy systems intensifies, MGs are positioned to play a pivotal role in shaping the energy landscape of the future [12].

1.2 Microgrids as a Means of Integrating Distributed Energy Resources: Opportunities and Challenges

The traditional centralized power generation model has long been the backbone of modern electrical grids. However, it faces numerous challenges, including transmission losses, vulnerability to large-scale outages, high dependency on fossil fuels, limited scalability to meet growing energy demand, and inherent incompatibility with the distributed and variable nature of RES [6]. These shortcomings highlight the growing need for more flexible, resilient, and sustainable energy systems.

In this context, decentralized generation has emerged as a viable alternative, offering localized energy production that reduces transmission inefficiencies and alleviates stress on centralized

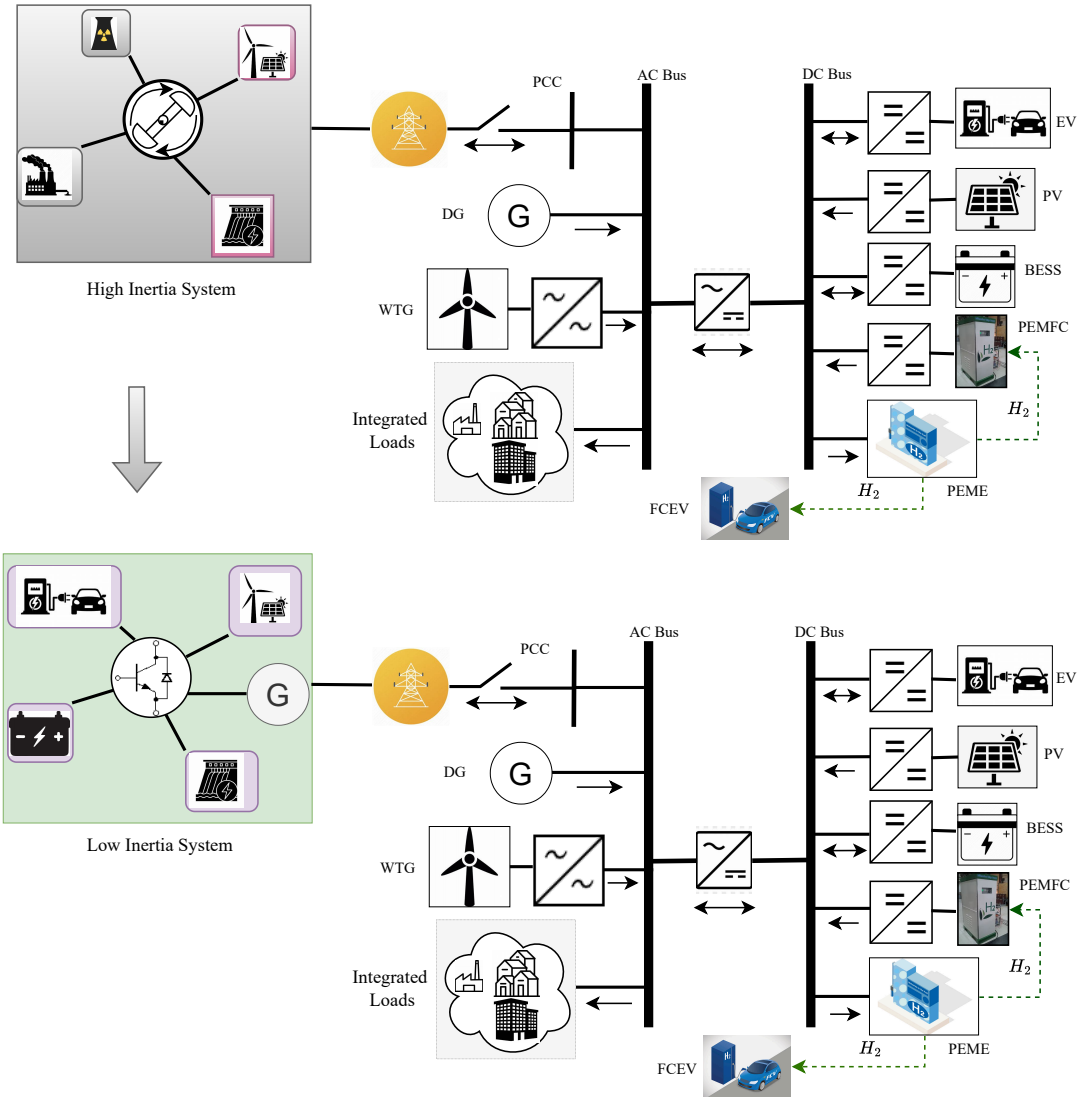

Fig. 1.1: Evolution of power systems toward converter-dominated architectures.

infrastructure. Renewable DERs—such as solar PV and wind turbines—and supporting technologies like ESS are key drivers of decentralized generation, providing cleaner and more sustainable power options [6], [7]. To enable the effective integration of renewable DERs and ESS, MGs have gained traction as adaptable, self-sustaining energy systems capable of operating both in grid-connected and islanded modes [11], [13]. MGs act as controllable entities that enhance local energy management, increase renewable penetration, and improve system flexibility [12].

Unlike conventional power systems that rely on synchronous generators for both energy conversion and inherent system stability, MGs depend largely on power electronic converters

(PECs) to interface DERs. This marks a fundamental shift toward converter-dominated architectures, where power electronics play a central role in control and energy management functions [14]. In this transition, the natural inertia and damping traditionally provided by synchronous machines are significantly reduced, weakening the system's ability to passively respond to disturbances.

As MGs and the broader grid evolve toward such converter-based configurations—as illustrated in Fig. 1.1—ensuring stability becomes increasingly reliant on advanced control strategies. While this shift enhances flexibility and controllability—especially in accommodating high penetrations of renewable energy—it also introduces important technical challenges, particularly during MG islanded operation. These include diminished frequency stability due to low system inertia, increased complexity in real-time control, and the need for accurate coordination and synchronization among DERs—challenges that are further compounded by the variable nature of renewable generation [12], [15].

Additionally, PECs can impact power quality by introducing harmonics and electromagnetic interference and may trigger adverse control interactions—such as resonance or instability in weak or low-inertia grids—thereby affecting overall system robustness and dynamic performance [10], [16]. The limited fault current contribution from PECs also complicates protection design, requiring more sophisticated detection and isolation mechanisms tailored to converter-based architectures, rather than conventional schemes used in traditional grids.

Addressing these challenges requires innovative approaches in both hardware and control domains. Advanced energy storage technologies—such as next-generation batteries and hydrogen-based systems—play a critical role in mitigating power fluctuations and ensuring energy availability amid variable renewable generation. Equally important are advanced decentralized control strategies specifically designed to manage the complexity and dynamic behavior of modern MGs. To contribute to this evolving field, this thesis aims to design and optimize sustainable MG systems that integrate DER for long-term energy balance and cost minimization, while developing computational intelligence–based optimization and control techniques to enhance the dynamic performance, efficiency, and adaptability of islanded MGs under decentralized primary control.

1.3 Research Objectives

The primary aim of this thesis is to design and optimize sustainable MG systems that effectively integrate DER for long-term energy balance and cost minimization, while developing advanced control techniques to enhance the dynamic performance, efficiency, and adaptability of MG operation. In line with this aim, the dissertation sets out to achieve the following specific research objectives:

Objective 1: To design and optimize MG systems that effectively integrate DER, focusing on long-term energy balance and cost minimization, while incorporating hydrogen-based storage solutions. This objective aims to enhance the sustainability and operational efficiency of MG by leveraging renewable energy sources and advanced storage technologies.

Objective 2: To develop advanced control and optimization techniques for VSC-based islanded MG, including the implementation of virtual complex impedance-based control strategies to improve power sharing accuracy and voltage and frequency regulation, and the development of a computationally guided, simulation-based optimization framework for coordinated tuning of filter and controller parameters to enhance dynamic performance, efficiency, and adaptability under varying operating conditions.

Objective 3: To enhance voltage and frequency regulation in VSC-based islanded MG by developing MLP-based controllers trained through a neuroevolutionary approach, thereby improving control adaptability, robustness against disturbances, and generalization to varying operating conditions.

1.4 Key Contributions of the Research

In line with the objectives outlined earlier, this dissertation presents the following key contributions, which directly address and fulfill the research aims:

Contribution I: Optimizing Hydrogen Integration and Distributed Energy Resources in Sustainable Microgrids

- Investigated how renewable hydrogen produced from excess renewable energy from PV and WT can reduce carbon emissions, minimize electricity wastage, and lower lifetime energy costs in MG. By utilizing surplus energy for green hydrogen production through electrolysis and charging the battery energy storage system (BESS), the overall system efficiency is enhanced and battery lifetime extended.
- Developed a comprehensive framework for integrating renewable energy sources with hydrogen production and utilization across power generation and transportation sectors, focusing on long-term energy balance, cost minimization, and enhanced operational efficiency.
- Implemented a dual strategy for storing surplus renewable electricity in BESS and producing renewable hydrogen onsite through electrolysis, maximizing the use of renewable energy and improving system efficiency and battery lifetime.
- Highlighted renewable hydrogen's dual role in decarbonizing both the electricity and transportation sectors, thus reinforcing sector coupling and enhancing sustainability.

Table 1.1: Mapping of Research Objectives, Contributions, and Corresponding Publications in the Dissertation.

Objectives		**Contributions**
Objective 1	P_1 & P_2	Contribution I
Objective 2	P_3 & P_4	Contribution II & Contribution III
Objective 3	P_5 & P_6	Contribution IV

- Demonstrated that injecting excess renewable electricity into the grid during surplus periods can reduce operational costs, enhancing the economic and environmental benefits of integrating hydrogen-based energy systems into sustainable microgrid architectures.

Contribution II: Development of Virtual Complex Impedance-Based Decentralized Control Strategy for VSC-based Islanded MG

- Developed a virtual complex impedance shaping strategy to enhance voltage and frequency regulation, improve transient performance, and achieve accurate decentralized active and reactive power sharing among multiple VSCs operating under islanded MG conditions.
- Validated the proposed strategy through detailed simulation studies, demonstrating robust performance against various system disturbances and dynamic load changes.

Contribution III: . Development of a computationally guided, simulation-based optimization framework for VSC parameter tuning

- A computationally guided simulation-based framework was developed in MATLAB/Simulink to optimize the LCL filter and controller parameters of VSCs.
- The framework improves the adaptability and dynamic performance of VSCs under varying operating scenarios, contributing to more robust and efficient MG control.
- It ensures compliance with IEEE-519 standards, achieving improvements in transient response and maintaining acceptable THD levels, thereby supporting high-quality power delivery even under disturbances.

Contribution IV: Development of Neuroevolutionary Training of MLP Controllers for Voltage and Frequency Control in VSC-based islanded MG

- Developed the Adaptive Hybrid PSO-Embedded GA (AHPEGA) approach, which integrates particle swarm optimization (PSO) and genetic algorithm (GA) with a local search

mechanism to optimize both MLP parameters and hyperparameters, overcoming limitations of conventional training methods and enhancing convergence, robustness, and generalization.

- Benchmarking results demonstrate AHPEGA's superior accuracy, stability, and rapid convergence, showcasing its potential to revolutionize neural network training and advanced MG control systems.
- Validated the robustness of the proposed controller under step load changes involving both linear and nonlinear loads, confirming improved dynamic response and reliable primary control performance.

1.5 List of Related Publications

The following are lists of publications included in the dissertation:

P_1. **Y. Bekele**, G. Biru, and L. B. Tjernberg, "Sustainable off-grid systems with integration of renewable generation and hydrogen-fuel cell," in 2022 IEEE PES Innovative Smart Grid Technologies Conference Europe (ISGT-Europe), 2022, pp. 1–5, https://10.1109/ISGT-Europe54678.2022.9960622.

P_2. **Y. B. Beyene**, G. B. Worku, and L. B. Tjernberg, "On the design and optimization of distributed energy resources for sustainable grid-integrated microgrid in Ethiopia," International Journal of Hydrogen Energy, 2023, https://10.1016/j.ijhydene.2023.04.192.

P_3. **Y. B. Beyene**, G. B. Worku, and L. B. Tjernberg, "On virtual complex impedance droop control of vsc-based islanded microgrids," in 2023 IEEE PES Innovative Smart Grid Technologies Europe (ISGT EUROPE), 2023, pp. 1–5, https://10.1109/ISGTEUROPE56780.2023.10408653.

P_4. **Y. B. Beyene**, G. B. Worku, and L. B. Tjernberg, "Developing a novel approach for passive damped LCL filter and controller parameter design using PSO algorithm in VSC-based islanded microgrids," Array, 100414. https://doi.org/10.1016/j.array.2025.100414.

P_5. **Y. B. Beyene**, G. B. Worku, and L. B. Tjernberg, "Enhancing Voltage and Frequency Control in Islanded VSC-Based Microgrids: A PSO-Driven Multilayer Perceptron Approach" in 2024 IEEE PES Innovative Smart Grid Technologies Europe (ISGT EUROPE), 2024, pp. 1–5, https://10.1109/ISGTEUROPE62998. 2024.10863686.

P_6. **Y. B. Beyene**, G. B. Worku, and L. B. Tjernberg, "Adaptive Hybrid PSO-Embedded GA for Neuroevolutionary Training of Multilayer Perceptron Controllers in VSC-Based Islanded Microgrids," Energy and AI, 21, 100551. https://doi.org/10.1016/j.egyai.2025.100551.

P7. Yi-Chun Lin, **Y. B. Beyene**, and L. B. Tjernberg, "Implications of EU Battery Regulation on Circular Economy: Barriers and Opportunities for Repurposing Electric Vehicle Batteries" in 2024 IEEE PES Innovative Smart Grid Technologies Europe (ISGT EUROPE), 2024, pp. 1–5, https://10.1109/ISGTEUROPE62998.2024.10863545.

1.6 Outline of the Thesis

This dissertation is structured around the key publications listed in Section 1.5 and is organized into six chapters, as outlined below:

Chapter 1 provides the general introduction, outlining the research objectives, main contributions, and associated publications.

Chapter 2 addresses MGs optimization, emphasizing the objectives and techniques for effective integration of DER.

Chapter 3 presents the optimized design of sustainable MG, highlighting the incorporation of DER and hydrogen integration strategies.

Chapter 4 details advanced control techniques for VSC-based islanded MG, including virtual complex impedance-based control and computationally-guided optimization frameworks.

Chapter 5 explores the neuroevolutionary training of MLP controllers for voltage and frequency control in VSC-based islanded MG.

Chapter 6 concludes the dissertation and proposes future work in the addressed research area.

Chapter 2

Microgrid Optimization

2.1 Objectives of Microgrid Optimization

The design and optimization of MGs are shaped by the diverse and sometimes conflicting interests of various stakeholders within the electricity supply chain. These stakeholders include system and network operators, owners and operators of DG units, energy suppliers, consumers, and regulatory authorities [17]. A critical aspect of MG design and optimization is the clear identification of design objectives. These objectives can be singular or encompass multiple specific targets that the MGs must achieve [18]. The primary design and optimization goals for MGs revolve around economic efficiency, environmental sustainability, and technical performance. Additionally, MGs can be engineered to simultaneously address multiple design objectives, striving to achieve an optimal balance among them.

2.1.1 Optimization of Microgrids Based on Economic Objective

The economic objective of MG optimization focuses on achieving cost-effectiveness, financial sustainability, and efficient energy production, consumption, and revenue generation. This objective balances economic benefits with reliability and environmental considerations. The design objective aims to reduce operational costs by continuously optimizing the economical dispatch while serving consumers [17]. In the economic option, the goal is to minimize total costs regardless of network impact or performance, which may be preferred by DG owners or operators. However, this approach operates DG without concern for grid or emission obligations, and its main limitations stem from the physical constraints of DG systems.

Optimizing MGs with a focus on economic objectives involves various strategies designed to cut costs while ensuring an efficient and reliable energy supply. One crucial approach is the optimal dispatch of DER, which entails scheduling energy generation and storage to minimize

fuel consumption and maximize the use of renewable sources [3]. By leveraging renewable energy sources like solar and wind, MGs can significantly reduce fuel costs and decrease reliance on traditional energy sources, thereby enhancing both economic efficiency and energy security. Additionally, the implementation of ESS plays a vital role in balancing supply and demand. ESS allows for the storage of excess energy during periods of low demand and its release during peak demand, reducing the need for costly peaking power plants and lowering overall energy expenses. Studies have demonstrated that ESS can enhance the economic performance of MGs by optimizing energy usage and decreasing dependence on grid power [3], [4].

2.1.2 Optimization of Microgrids Based on Environmental Objective

The environmental objective of MG optimization aims to minimize environmental impact by promoting renewable energy sources, reducing greenhouse gas emissions, and enhancing sustainability. This involves operating the MG in an eco-friendly manner, prioritizing the dispatch of DG units with lower emissions, regardless of financial or technical considerations [17], [18]. This approach aligns with environmental targets and regulatory schemes, focusing solely on emission quotas and the physical limitations of DG systems.

To achieve these environmental objectives, MGs integrate renewable energy sources and advanced energy storage systems. Combining batteries and hydrogen production systems is an effective strategy. Excess energy from PV panels and wind turbines can be stored in batteries for short-term use, providing quick response times to balance supply and demand [3], [4]. For long-term storage, excess energy can produce hydrogen through electrolysis, which splits water into hydrogen and oxygen using electricity [4].

Hydrogen serves multiple purposes. It can fuel hydrogen fuel cell vehicles (FCEVs), where the fuel cell generates electricity through a reaction between hydrogen and oxygen, producing only water as a byproduct. This transition from fossil-fuel-based vehicles to FCEVs significantly reduces greenhouse gas emissions and fossil fuel dependency [3], [4]. Additionally, hydrogen can be used as a backup power source. During periods of low renewable energy

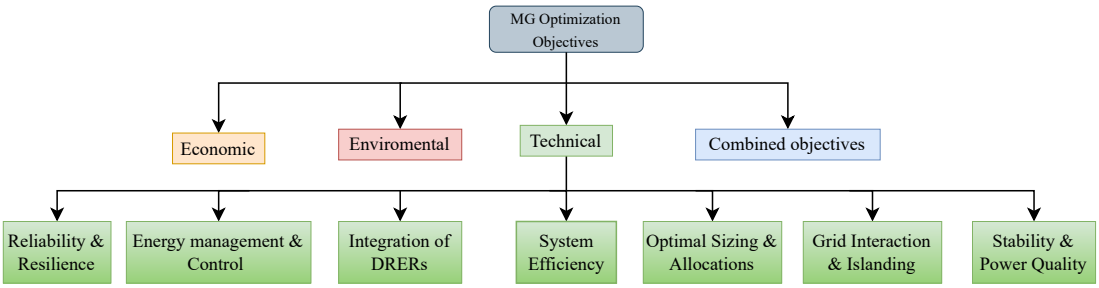

Fig. 2.1: Different Microgrid optimization objectives

production or high demand, stored hydrogen can be converted back into electricity using hydrogen fuel cells, ensuring a reliable power supply with zero emissions.

By integrating batteries and hydrogen-based energy storage systems, MGs achieve a balanced and resilient energy storage solution. Batteries provide immediate energy support, while hydrogen offers long-term storage and additional applications, such as fueling vehicles and backup power generation. This integrated approach optimizes the environmental performance of MGs, enhancing their overall efficiency and reliability.

2.1.3 Optimization of Microgrids Based on Technical Objectives

Technical optimization of MG focuses on enhancing reliability, efficiency, and stability while ensuring optimal resource utilization. It prioritizes minimizing power losses, voltage variations, and device loading without considering DG production costs and revenues. System operators favor this approach due to its emphasis on technical performance. As illustrated in Fig. 2.1, different technical objectives have been presented in the literature.

Reliability and Resilience

Ensuring reliability and resilience is a key technical objective, particularly for critical loads. MGs must withstand disruptions such as natural disasters and grid outages while maintaining a stable power supply. This capability is crucial for critical infrastructure, such as hospitals, emergency services, and data centers, which require uninterrupted power to function effectively. MGs enhance resilience by providing localized power generation and storage, which can operate independently from the main grid during outages. The integration of renewable energy sources and advanced storage technologies further strengthens the resilience of MGs by ensuring a sustainable and reliable power supply [19].

Energy Management and Control

Advanced Energy Management Systems (EMS) and real-time control strategies are essential for optimizing MG operations, ensuring stability, reliability, and cost-effectiveness. These systems dynamically regulate power generation, storage, and distribution to maintain a demand-supply balance while adapting to fluctuations using predictive control and real-time optimization techniques [20]. Given the diverse nature of MG—integrating renewable energy sources, dispatchable units, storage systems, and loads—an EMS is critical for coordinating these elements to ensure efficient and sustainable operation.

Since each DER has different operational costs and constraints, optimal dispatch is necessary for continuous supply and economic viability. In grid-connected mode, EMS maximizes efficiency by strategically trading power with the grid and optimizing DER usage to enhance

profits. Conversely, in islanded mode, the focus shifts to extending MG operation without external support, requiring intelligent resource allocation. To achieve these goals, EMS employs optimization algorithms that schedule energy resources based on predefined objectives, ensuring cost reduction, energy efficiency, and reliable integration of renewables.

Beyond optimization, EMS incorporates hardware and software components to monitor, control, and forecast energy flow. By continuously analyzing load demand, renewable generation patterns, and storage levels, EMS ensures that microgrids operate at peak efficiency. Through intelligent energy dispatch, and real-time forecasting, EMS plays a pivotal role in enhancing resilience, sustainability, and economic viability, making it indispensable in modern MG operations.

Integration of Distributed Energy Resources

Incorporating renewable sources such as solar and wind requires addressing their intermittency. ESS, including hybrid storage solutions like battery-hydrogen combinations, play a crucial role in ensuring a stable and reliable energy supply. These systems balance short-term and long-term storage needs, enhancing overall MG stability [21]. Key objectives include minimizing costs, maximizing renewable energy integration, reducing load shedding, and achieving an optimal levelized cost of energy (LCOE). Peak shaving is also considered to enhance energy efficiency and reduce emissions.

Optimal Sizing and Allocation

Optimal sizing and allocation of DER are crucial for ensuring MG efficiency, reliability, and cost-effectiveness. Proper sizing and placement help balance technical and economic constraints while meeting demand effectively [22]. MG sizing involves architecture selection and energy flux optimization to enhance performance. Optimization studies may focus on component sizing, energy management, or a combined approach using advanced algorithms. Renewable energy utilization depends on geographic factors and resource availability. Ultimately, efficient MG sizing and energy management are essential for cost reduction, reliability, and sustainability [23].

Grid Interaction and Islanding

MGs operate in both grid-connected and islanded modes. Technical optimization ensures seamless transitions between these modes while maintaining stability and reliability. In grid-connected mode, MGs provide ancillary services, whereas in islanded mode, they independently manage energy supply and demand. Advanced control algorithms facilitate smooth transitions, ensuring continuous operation [21].

System Efficiency

Maximizing system efficiency in MG involves minimizing energy losses and optimizing energy conversion processes. Advanced monitoring systems help identify and mitigate energy losses, ensuring each component operates within its optimal range. Intelligent control systems and optimization algorithms play a vital role in ensuring optimal resource utilization and reducing waste within MG. Techniques such as GA, PSO, and reinforcement learning dynamically adjust the operation of energy systems based on real-time data, improving efficiency and stability. By integrating these strategies, MGs achieve higher efficiency, reliability, and sustainability, leading to cost reductions and improved performance [24], [25].

Stability and Power Quality

Stability and power quality are critical for smooth MG operation. Stability ensures steady-state operation despite supply and demand fluctuations, while power quality maintains voltage stability and minimizes disturbances such as harmonics or flicker. Techniques like the Unified Power Quality Conditioner (UPQC) with coordinated PQ theory controller-based optimization enhance both stability and power quality, ensuring reliable and efficient MG operation [12], [15].

2.1.4 Optimization of Microgrids Based on Combined Objectives

The combined objective approach addresses the multi-objective problem of optimal dispatch for distributed generation (DG), considering economic, technical, and environmental factors. Specifically, it converts technical and environmental criteria into economic equivalents while considering constraints imposed by both the network and DG physical limits [26]. This approach is particularly relevant for actors who participate not only in traditional energy markets but also in other potential markets related to network services and emission certificates.

2.2 Techniques for Microgrid Optimization

Optimization techniques for MGs aim to enhance efficiency, reliability, and stability by utilizing various computational and analytical methods. These techniques can be broadly categorized into artificial intelligence (AI)-based optimization, metaheuristic algorithms, and classical analytical methods, as illustrated in Fig. 2.2.

2.2.1 Artificial Intelligence (AI)-Based Optimization

AI-driven techniques, including machine learning (ML) and deep learning (DL), are increasingly applied in MG optimization. For instance, reinforcement learning (RL) has been utilized

to develop real-time optimization strategies for MGs, addressing challenges such as the variability of renewable energy sources and the complexity of mixed-integer nonlinear programming problems [27]. Additionally, convolutional neural networks (CNN) have been proposed for economic dispatch in MG, offering efficient and reliable solutions compared to traditional methods [28].

2.2.2 Population-Based Metaheuristics

These algorithms operate on a population of potential solutions, iteratively improving them through mechanisms inspired by natural processes. Techniques such as GA, PSO, and Ant Colony Optimization (ACO) have been effectively applied to optimize MG operations. A comparative study demonstrated the efficacy of these algorithms in determining the optimal sizing of hybrid standalone MG, highlighting their ability to handle complex, nonlinear optimization problems [29], [30].

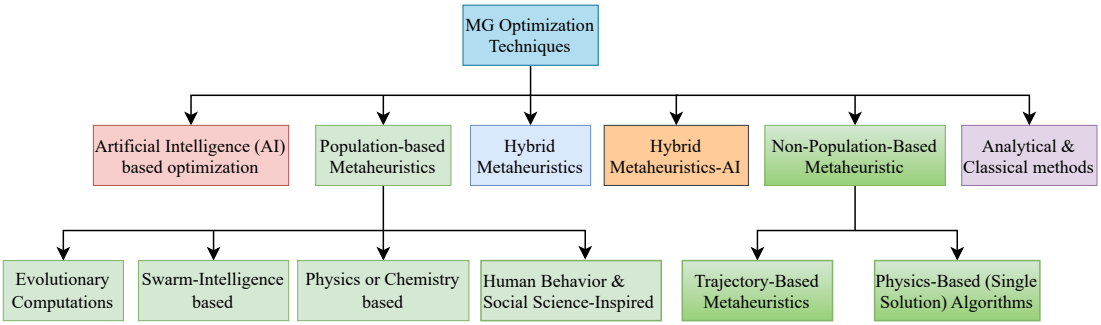

Fig. 2.2: Classification of Microgrid Optimization Techniques

2.2.3 Hybrid Metaheuristics

Combining multiple metaheuristic algorithms can balance exploration and exploitation capabilities, leading to improved optimization performance. For example, integrating GA with PSO has been shown to enhance the convergence rate and solution quality in MG optimization tasks. Such hybrid approaches address the limitations of individual algorithms, providing more robust solutions for complex energy management problems [20].

2.2.4 Hybrid Metaheuristics-AI

The integration of AI techniques with metaheuristic algorithms further enhances MGs optimization. For instance, combining deep reinforcement learning (DRL) with PSO enables adaptive energy management in dynamic environments, effectively addressing the uncertainties associated with renewable energy sources [27]. This hybridization leverages the strengths of both AI and metaheuristics, offering improved adaptability and efficiency in MG operations.

2.2.5 Non-Population-Based Metaheuristics

These methods focus on iteratively improving a single solution. Algorithms such as Simulated Annealing (SA) and Tabu Search (TS) have been applied to MG optimization problems. Their effectiveness lies in their ability to escape local optima and efficiently search the solution space, making them suitable for specific optimization challenges in microgrid management [31].

2.2.6 Analytical and Classical Methods

Traditional optimization approaches, including linear programming (LP) and mixed-integer linear programming (MILP), provide mathematically rigorous solutions for MG optimization. While these methods are well-suited for problems with well-defined constraints, they may face challenges when dealing with highly nonlinear and uncertain systems. Nonetheless, they remain relevant, especially when integrated with AI and metaheuristic techniques to enhance overall optimization performance [32].

2.3 Control Strategies for Microgrids

Control systems are essential for the real-time operation and stability of MG, managing power flow, voltage, and frequency to ensure smooth operation, whether connected to the main grid or operating independently. The primary goals are to maintain stability, prevent outages, and respond to real-time changes in energy demand and supply [33].

MGs control strategies ensure stability, reliability, and efficiency through power generation, load balancing, and grid interaction. These strategies are divided based on time response and functionality into three hierarchical levels: primary, secondary, and tertiary control [34], as illustrated in Fig. 2.3. Each level can be further categorized into centralized, decentralized, and distributed approaches based on control architecture, decision-making processes, and communication requirements [35].

2.3.1 Hierarchical Control

This control method is structured into three levels: primary, secondary, and tertiary, each differing in response speed and duties.

Primary Control: Primary control is the first and fastest level in the hierarchical control system, focusing on local controllers. It requires minimal or no communication to address power network issues quickly, stabilizing frequency and voltage, though not at nominal values [36], [37]. In the case of MGs, the main functions include controlling active power and voltage

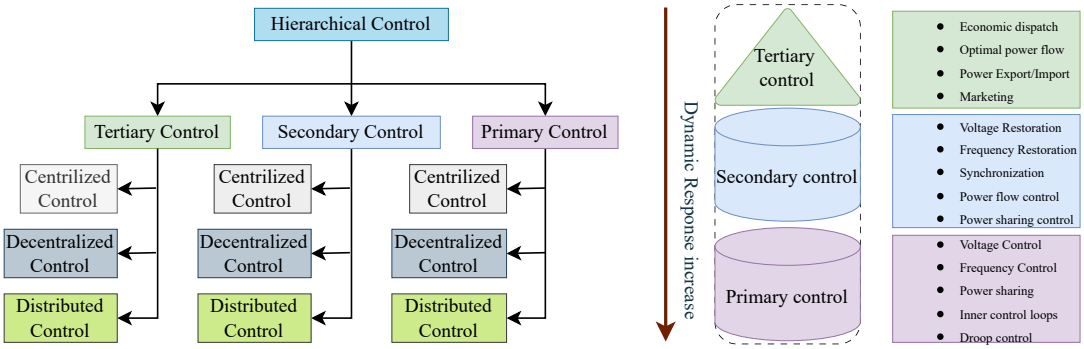

Fig. 2.3: Microgrid hierarchical control

in island mode and regulating MG frequency when disconnected from the main grid. Primary control manages inner voltage and current control loops, frequency regulation, and power sharing, with droop control being the most common decentralized approach. Other communication-based techniques, such as master-slave control, can also be used, though they are less common. The appropriate selection of control strategies depends on various factors, including the nature of the MG, the types of DG used, and the specific requirements of the system.

Secondary Control: Secondary control focuses on restoring the system to its nominal operating conditions after a disturbance, operating on a slower timescale than primary control and often involving coordination among multiple controllers. It compensates for steady-state errors in voltage and frequency, bringing them back to nominal values after primary control stabilization [36], [37].

Tertiary Control: Tertiary control operates on a slower timescale and involves higher-level decision-making in the hierarchical control of MG. It manages power exchange between the MG and the main grid, optimizing operation by controlling active and reactive power references for each DER based on economic criteria. In grid-connected mode, it considers load changes, generation forecasts, energy storage, demand requirements, and market signals to minimize costs while meeting demand. In island mode, it restores reserves, manages congestion, and adjusts power based on resource availability. An EMS at this level coordinates DER, forecasts supply and demand, and ensures compliance with grid codes, optimizing overall grid operation and maintaining stability [36], [37].

2.3.2 Centralized Control

A centralized control strategy, commonly used in traditional power systems, involves a single central controller that collects data from each local controller (LC) and generates commands

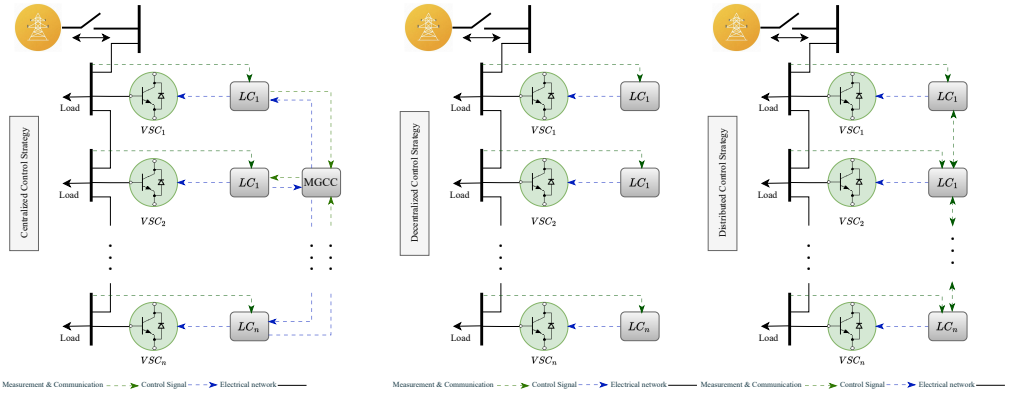

(a) (b) (c)

Fig. 2.4: Microgrid control strategies. (a) Centralized control. (b) Decentralized control. (c) Distributed control.

for them. In this setup, LCs do not communicate with each other and cannot act independently. The central controller processes the information and issues commands via a communication network, as shown in Fig. 2.4a. This centralized scheme offers the advantage of controlling the entire system from a single point. However, it is susceptible to a single point of failure, which could lead to the collapse of the entire MG. Other drawbacks include potential performance issues due to communication delays and measurement errors, as well as a high computational burden on the central controller, especially in geographically large MG. Additionally, expanding or reconfiguring the system requires redesigning the central controller, adding to its complexity. Despite these drawbacks, centralized control can be effective where communication is reliable and system stability is paramount.

2.3.3 Decentralized Control

In decentralized control, each unit is managed by its LC without digital communication links between units, as shown in Fig. 2.4b. Each controller operates independently, relying solely on local measurements to manage a specific part of the MG. This approach is well-suited for diverse, complex, and large-scale systems, offering plug-and-play capability and computational efficiency [38]. It enhances system reliability by preventing disturbances from propagating, allowing continued operation even if multiple units fail.

Decentralized control addresses several limitations associated with centralized and distributed control strategies by enhancing economic feasibility, scalability, and operational reliability. Unlike centralized schemes, it avoids single points of failure and reduces infrastructure costs, as it does not rely on a central controller or extensive communication infrastructure. Furthermore, unlike distributed control, which still requires communication among local agents, decentralized control operates fully autonomously—each unit makes decisions based solely

on local measurements. However, its lack of coordination mechanisms poses challenges in systems with multiple DERs. Strong electrical coupling among units can lead to suboptimal performance, power sharing inaccuracies, and dynamic instabilities, especially under varying load or generation conditions.

2.3.4 Distributed Control

Distributed control offers a balanced compromise between the global coordination of centralized approaches and the autonomy of decentralized schemes. In this strategy, each DER operates with its own local controller while exchanging limited information with neighboring units through a communication network. Local controllers communicate directly with one another, facilitating a distributed cooperative effort, as shown in Fig. 2.4c. This structure enhances scalability, fault tolerance, and adaptability, making it suitable for complex microgrid architectures with multiple DERs. Unlike centralized control, it avoids single points of failure and reduces computational bottlenecks by distributing decision-making responsibilities. Compared to purely decentralized control, distributed schemes enable cooperative behavior among units, which significantly improves power-sharing accuracy, voltage and frequency regulation, and dynamic performance [38].

However, distributed control still depends on a reliable communication infrastructure. Latency, synchronization issues, or communication failures can degrade system performance or even jeopardize stability. Additionally, implementing consensus algorithms or distributed optimization protocols introduces complexity in controller design and real-time operation [38].

Chapter 3

Optimized Microgrid Design with Renewable Energy and Hydrogen Integration

3.1 Introduction

In an era where climate change and energy security are at the forefront of global concerns, the international energy landscape is undergoing a pivotal transformation as the demand for clean, resilient, and efficient power solutions continues to rise [1], [39]. As traditional centralized power systems remain heavily dependent on fossil fuels, they face mounting challenges, including resource depletion, environmental degradation, supply volatility, and grid instability. These pressing issues underscore the urgent need for innovative and sustainable energy alternatives [40].

In response, MGs designed with DER and hydrogen integration have emerged as a transformative solution. By facilitating independent operation and the seamless integration of diverse energy sources, MGs enhance both resilience and sustainability. This chapter explores the optimized design of sustainable MGs, highlighting the critical role of DER and hydrogen technology in overcoming contemporary energy challenges and enabling a more robust and flexible energy system.

By harnessing RES such as solar, wind, and bioenergy, MG offers a decentralized and resilient energy infrastructure that reduces reliance on fossil fuels while promoting sustainability [3], [4]. When integrated with advanced storage and management systems, these RES can enhance grid stability and supply reliability. The incorporation of hydrogen technology further

strengthens MG capabilities, providing increased energy security, grid independence, and carbon neutrality. Hydrogen plays a crucial role not only in energy storage and distribution but also in enabling sector coupling, where energy is efficiently integrated across electricity, industry, and transportation sectors [41], [42]. This integration allows MG to function as hubs for optimized energy management, utilizing surplus renewable energy for hydrogen production. The hydrogen produced can then be used for backup power generation, fuel cell vehicles, or heating systems. By addressing the intermittency challenges of renewable energy, hydrogen ensures flexible and reliable energy storage, thus further boosting grid resilience and supporting long-term carbon neutrality [3].

3.2 Enhancing Renewable Energy Integration in Microgrids through Sector Coupling

The integration of RES in MG marks a significant shift in energy systems. As demand for cleaner energy grows, MG with renewable technologies are crucial for addressing environmental and energy security challenges. MG offer decentralized energy generation and distribution, integrating RES, reducing fossil fuel dependency, and enhancing system resilience. However, the variability of RES such as solar and wind necessitates addressing intermittency challenges to ensure a stable and reliable power supply [42].

Addressing intermittency challenges is crucial for the successful integration of RES in MG. The variability in solar and wind generation can disrupt a stable power supply, necessitating advanced solutions to enhance grid flexibility. According to the International Renewable Energy Agency (IRENA), renewable electricity could supply 86% of global power consumption by 2050 under the 1.5°C scenario, with solar PV and wind energy contributing 74% of this share [1], [40]. Accommodating such high shares of variable renewables requires significant advancements in grid flexibility, further underscoring the need for integrated energy solutions [40]. Key strategies include advanced energy storage systems, demand response mechanisms, and optimization techniques to balance supply and demand effectively. However, these approaches often focus solely on electricity. A more comprehensive solution is sector coupling, which integrates electricity, heating & cooling, industrial processes, and transportation. By interconnecting these sectors, MG can enhance resilience, optimize energy utilization, and drive broader decarbonization efforts [41]. Sector coupling enables the efficient use of surplus renewable energy across these sectors. For instance, in addition to charging BESS, excess electricity can be used to produce hydrogen, an energy carrier for various applications. Hydrogen, through fuel cells, can provide backup power, heating, or fuel for electric vehicles, ensuring efficient utilization of generated energy and improving overall efficiency and stability. Hydrogen as a storage and transport medium creates a holistic energy ecosystem, supporting decarbonization and optimizing energy use [40]. Moreover, hydrogen can be utilized

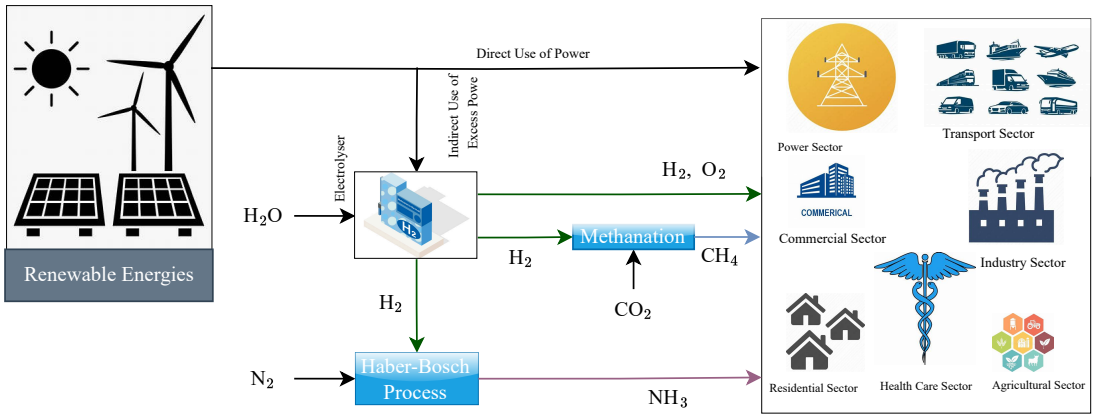

Fig. 3.1: Representation of sector coupling and its role in enhancing energy system flexibility.

in industrial processes, such as steel production, and as a feedstock for chemical industries, further expanding its role in achieving a sustainable energy system (see Fig. 3.1). Furthermore, sector coupling technologies, such as electrolysers for hydrogen production, enable demand to respond more dynamically to grid control signals in renewable energy-integrated MG, enhancing grid flexibility and stability [4], [43].

In addition to the benefits of hydrogen in sector-coupled technologies, its integration with BESS in hybrid storage systems enhances MG efficiency, flexibility, and resilience. This combination allows MG to effectively manage both short-term power fluctuations and long-term energy demands [3], [4]. While BESS is ideal for rapid response and high power demands, hydrogen storage supports long-duration energy storage and provides backup during extended outages.

By shifting long-duration storage to hydrogen, the hybrid system reduces stress on BESS, enabling it to operate with shallower discharge depths. This results in fewer cycles, less degradation, longer battery lifespan, and reduced maintenance costs.

3.3 Optimized Microgrid Architecture and System Physical Modeling

3.3.1 Optimized Microgrid Architecture

The optimized MG architecture, designed to integrate renewable energy sources and hydrogen technology for enhanced efficiency and resilience, is being developed to meet the energy demands of an industrial park in Adama, Ethiopia, located approximately 100 km from the capital, Addis Ababa [3]. This industrial hub primarily depends on the national utility grid for its power supply. However, frequent grid interruptions disrupt manufacturing operations, necessitating a diesel generator as a backup to sustain continuous production during outages.

According to Ethiopian Electric Utility (EEU) data from 2020 and 2021, the industry experienced an average of 50 outages per year, with a mean repair duration of 66.21 hours [3], [44]. The primary causes of these interruptions include system blackouts, under-frequency events, and transmission line overloading. Given these persistent power challenges, integrating alternative energy sources at the production site is a strategic move to enhance energy reliability, alleviate pressure on the national grid, and reduce dependency on fossil fuel-based backup systems [45], [46].

Previous feasibility studies conducted at the site [3], [43], [47] have identified solar and wind energy as the most viable renewable energy options for integration. The region exhibits promising resource potential, with average wind speeds exceeding 4 m/s at 10 meters and daily solar radiation surpassing 6 kWh/m²/d [47], [48]. Leveraging these abundant local resources, the proposed MG architecture is designed to provide a reliable, resilient, and sustainable power supply. The MG integrates DER, including PV systems and wind energy, supported by a hybrid storage system that combines BESS and hydrogen storage. This setup ensures a stable and flexible power supply by addressing the intermittency challenges of renewable energy sources, enabling the industrial park to operate efficiently while advancing sustainability and energy independence.

Building on this foundation, various configurations of PV panels, WT, and hybrid storage solutions are explored to determine the most efficient and reliable energy supply strategy for the industrial park [3]. By integrating both short-term (BESS) and long-term (hydrogen) storage, the system ensures grid energy balance and flexibility while maximizing the utilization of locally available renewable resources.

As part of the transition to a more sustainable and self-sufficient energy system, the model in Fig. 3.2 replaces the dependency on the utility grid and diesel generator backup with a

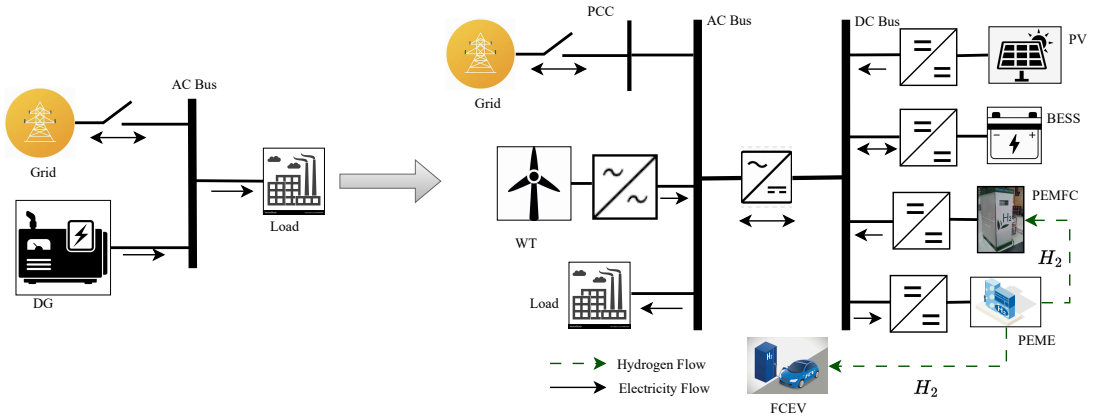

Fig. 3.2: System transition from diesel-supported grids to renewable-dominated configurations with integrated hydrogen systems.

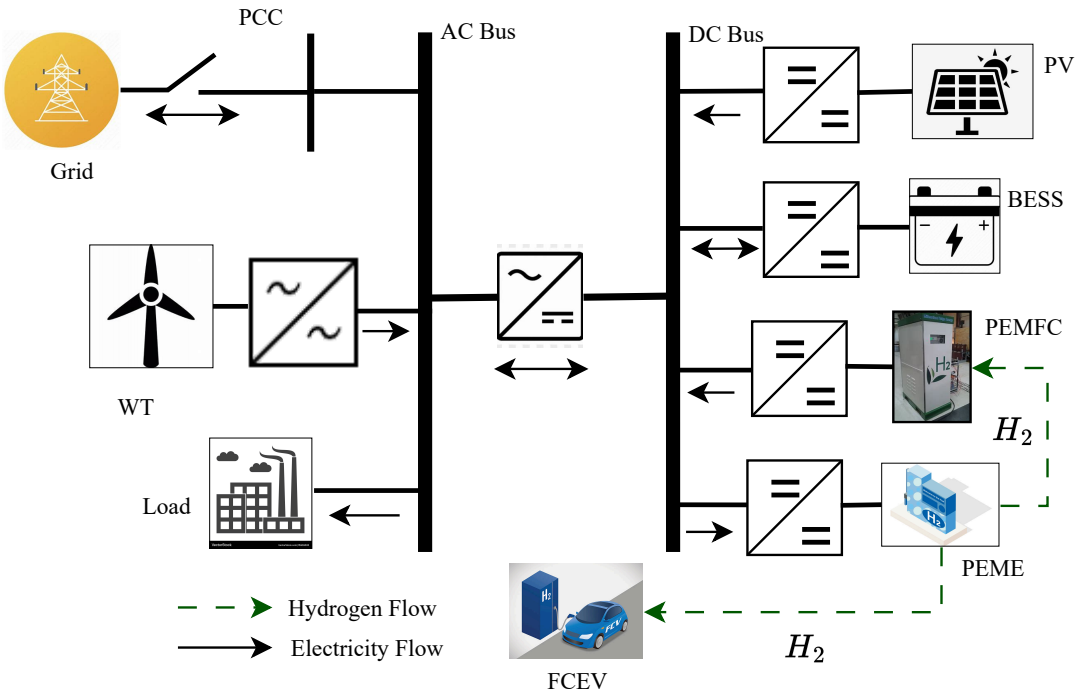

Fig. 3.3: Optimized Microgrid Architecture for the Case Study.

fully renewable-based approach. By tailoring the MG's design to the industrial park's load profile and local renewable resource potential, the proposed architecture (Fig. 3.3) enhances energy self-sufficiency while maintaining economic feasibility and promoting environmental sustainability. In this optimized MG architecture, PV and WT are the primary power sources, with hybrid storage managing supply and demand. Excess electricity is stored in BESS for short-term fluctuations or converted into hydrogen through electrolysis for long-term storage, supporting grid reliability and sector coupling applications [3], [4].

Beyond providing backup power through Proton Exchange Membrane Fuel Cells (PEMFC), the electrolytic hydrogen produced from renewable sources is also used to fuel 30 FCEVs, representing an initial step toward reducing fossil fuel dependence in transportation [3]. This underscores hydrogen as a key energy carrier, crucial for enabling sector coupling.

3.3.2 System Physical Modeling

Renewable Energy Potential and Demand Analysis

In the MG modeling and optimization process, energy potential and demand analysis are conducted beforehand to assess the effectiveness and suitability of the renewable energy-integrated MG for the case study. As shown in Fig. 3.4a, the site receives an annual average solar radiation of 6.06 kWh/m^2/d. The clearness index, which represents the ratio of global

horizontal irradiance to the extraterrestrial irradiance, ranges from 0.51 to 0.68, indicating favorable conditions for PV system deployment [3]. Similarly, Fig. 3.4b depicts the monthly mean wind speed at the site, where the annual average, computed from hourly wind speed data, is 4.95 m/s, with monthly variations between 3.6 m/s and 5.5 m/s [3].

Following the energy potential, the industrial park's hourly electrical and hydrogen load profiles were synthesized from daily average data to generate 8,760 hourly values for a full year. The total daily electrical load profile was obtained from the AIP, showing an average energy consumption of 60.462 MWh/d with an annual peak demand of 4.23 MW.

Additionally, a hypothetical hydrogen refueling station, powered by renewable sources, was assumed to be located in AIP, meeting a daily hydrogen demand of 180 kg/d. Given a 6 kg FCEV tank capacity [49]–[51], this station could refuel 30 FCEVs daily. With a hydrogen

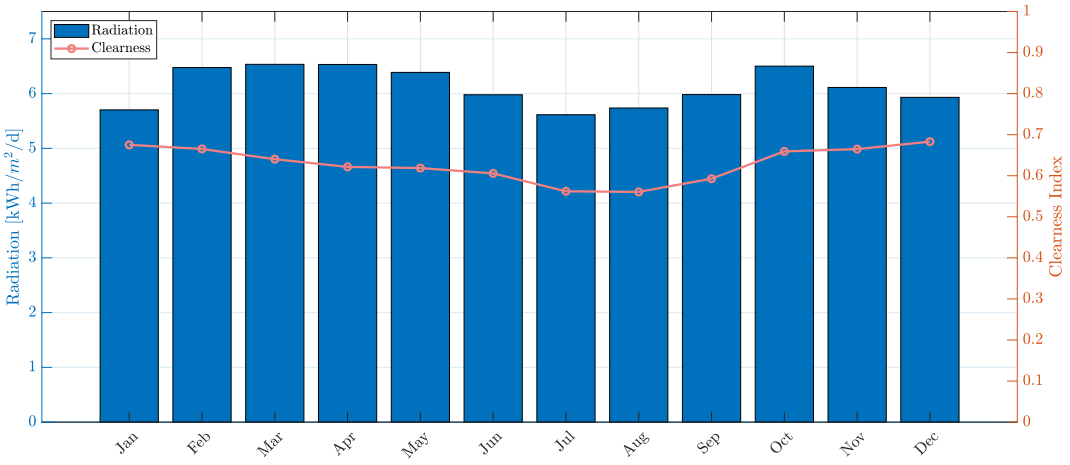

(a)

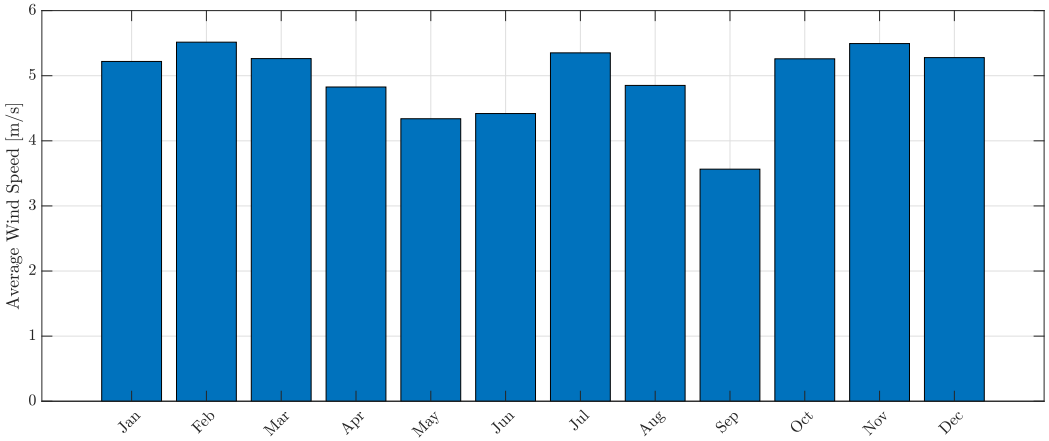

(b)

Fig. 3.4: Site meteorological data: (a) Solar radiation and (b) wind speed measurements.

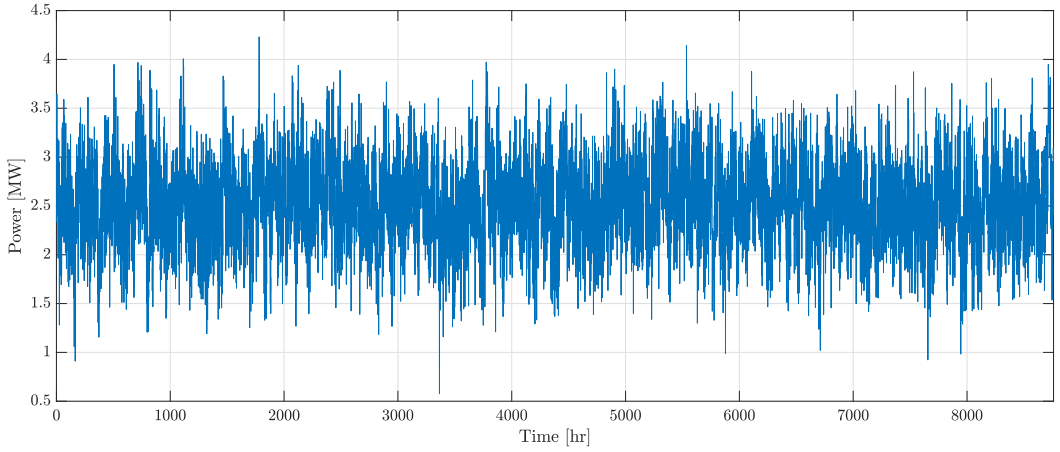

(a)

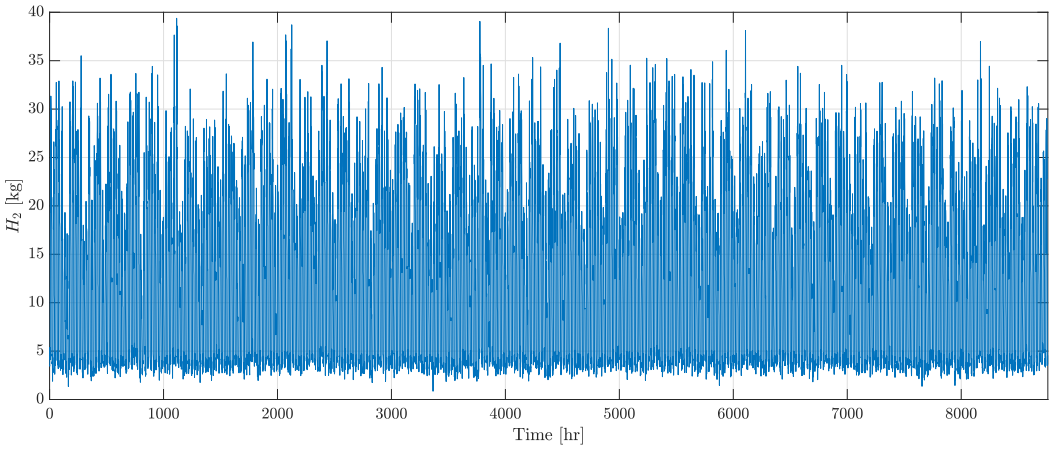

(b)

Fig. 3.5: (a) Hourly electrical load profile. (b) Hourly hydrogen load profile.

consumption rate of 0.6 kg/100 km [3], [50], each vehicle could achieve a range of 1 000 km per refuel.

To make the hourly load profile more realistic, daily and hourly random variability (15% and 10%, respectively) were considered to add randomness to the load profile. Then, in each time step, the value in that time step is multiplied by a perturbation factor (α_L) [3]:

$$\alpha_L = 1 + \delta_d + \delta_h \tag{3.1}$$

where δ_d and δ_h represent the daily and hourly perturbation factors, respectively. The synthesized hourly electrical and hydrogen load profiles are illustrated in Fig. 3.5a and Fig. 3.5b.

Components Physical Modeling

PV System Modeling: Solar irradiance and ambient temperature are key factors that significantly impact the output of the PV system. The power generated by the PV system (P_{PV}) is mathematically expressed as [3], [4], [52]:

$$P_{PV} = Y_{PV} f_{PV} \left(\frac{G_T}{G_{T,STC}} \right) \left[1 + \alpha_P \left(\frac{T_C}{T_{C,STC}} \right) \right] \tag{3.2}$$

where Y_{PV} is the rated capacity of the PV array [kW], f_{PV} is the PV derating factor [%], G_T represents the solar irradiance, $G_{T,STC}$ is the standard test condition (STC) irradiance, T_C is the cell temperature, and $T_{C,STC}$ is the standard test condition temperature. This equation captures how variations in solar irradiance and temperature affect the system's performance.

Wind Turbine Modeling: The electrical output of a wind turbine is influenced by factors such as wind speed, air density, and turbine characteristics, which vary by location, making wind power highly intermittent and nondispatchable. To estimate the wind speed at hub height, the following equations are used [3], [53], [54]:

$$v_{hub} = v_{anem} \left(\frac{z_{hub}}{z_{anem}} \right)^{\alpha} \tag{3.3}$$

$$v_{hub} = v_{anem} \frac{ln\left(z_{hub}/z_0\right)}{ln\left(z_{anem}/z_0\right)} \tag{3.4}$$

where v_{hub} is the wind speed at hub height, v_{anem} is the anemometer wind speed, z_{hub} is the hub height, and α is the power law exponent.

The expected power output of the wind turbine at hub height wind speed is determined by the wind turbine's power curve, which relates wind speed to electrical output. If the wind speed is outside the turbine's operating range (below the cut-in or above the cut-out speed), no power is produced [3], [54]. The actual wind turbine power output (P_{WTG}) is then calculated by adjusting the standard power output at standard conditions ($P_{WTG,STC}$) by using the air density ratio, as given below [3], [49]:

$$P_{WTG} = P_{WTG,STC} \left(\frac{\rho}{\rho_0} \right) \tag{3.5}$$

where ρ is the actual air density, and ρ_0 is the standard air density (1.225 kg/m^3).

PEMFC Modeling: A PEMFC is an electrochemical device that converts chemical energy from hydrogen into electrical energy through an electrolytic reaction, with water vapor being

the primary byproduct [3], [55]. The PEMFC power output is calculated as:

$$P_{FC} = V \times I \times N \tag{3.6}$$

Where P_{FC} is the power output, V is the voltage of a single cell under load, I is the current, calculated by multiplying the current density by the active cell area, N is the number of cells in the stack. The fuel consumption of the generator as a function of its electrical power output is given by the following equation [3], [56]:

$$F = F_0 Y_{FC} + F_1 P_{FC} \tag{3.7}$$

where F is a fuel consumption rate [kg/hr], F_0 is a generator fuel curve intercept coefficient [kg/hr/kW$_{rated}$], F_1 is the fuel curve slope in [kg/hr/kW$_{output}$], Y_{FC} is the rated capacity of the generator [kW].

The PEMFC F_0 is the ratio of its no-load fuel consumption to its rated capacity. In this research F_0 and F_1 are set to zero and 0.05 kg/hr/kW, respectively, which gives a constant efficiency of about 60 % [3].

The PEMFC fixed cost ($C_{FC,fix}$) and marginal cost ($C_{FC,mar}$) of energy can be calculated as [3], [56]:

$$C_{FC,fix} = C_{FC,O\&M} + \frac{C_{FC,r}}{R_{FC}} + F_0 Y_{FC} C_{fuel,eff}; \quad C_{FC,mar} = F_1 C_{fuel,eff} \tag{3.8}$$

where $C_{FC,fiX}$ is a fixed cost of energy [$/hr], $C_{FC,mar}$ is the marginal cost of energy [$/kWh], $C_{FC,O\&M}$ is the operation and maintenance cost [$/hr], $C_{FC,r}$ is the replacement cost [$], R_{FC} is the generator lifetime [hr], Y_{FC} is the capacity of the generator [kW], and $C_{fuel,eff}$ is the effective price of fuel [$/kg]. As hydrogen is produced onsite from excess power generated by PV and WT, the marginal cost of energy for the PEMFC generator is zero.

PEME Modeling: Electrolysis is a well-established method for hydrogen production and more attractive if integrated with power generation systems based on renewable energy sources [3]. The most common types of electrolysers are alkaline and Proton Exchange Membrane electrolyzers [57]–[59]. In a renewable energy-integrated microgrid, a Proton Exchange Membrane electrolyzer (PEME) serves as both a hydrogen production unit and a flexible load, dynamically adjusting its operation based on real-time energy availability [60], [61]. Its high efficiency and rapid response time make it ideal for managing the intermittency of solar and wind energy, allowing excess electricity to be utilized effectively for hydrogen production [62], [63]. As a flexible load, PEME can scale its consumption up or down to balance supply-demand fluctuations, enhancing grid stability [64]. Its compact and scalable design ensures

seamless integration into microgrid systems, while its ability to operate efficiently under variable loads maximizes hydrogen yield without straining the power network [65], [66]. Additionally, PEME produces high-purity hydrogen, crucial for applications such as fuel cells and industrial processes, further reinforcing its role in optimizing energy utilization within the microgrid [67], [68].

BESS Modeling: Integrating BESS into grid-connected MGs enhances reliability, supports energy arbitrage, and improves renewable utilization, though economic viability depends on system design, market dynamics, and policy support [3], [45], [69]. In weak-grid areas, BESS is vital for outage resilience, renewable fluctuation management, and peak demand support [70], [71]. The operational performance of BESS is governed by its state of charge (SOC), charging/discharging efficiency, and technical constraints such as capacity limits and degradation characteristics [54], [72]. The power output of the battery (P_{BESS}) is calculated as:

$$P_{BESS} = \eta_B P_{dis}, \quad \text{(discharging mode)}; \quad P_{BESS} = \frac{P_{ch}}{\eta_B}, \quad \text{(charging mode)} \tag{3.9}$$

where P_{BESS} is net power output/input of the battery [kW], P_{dis} is power discharged from the battery [kW], P_{ch} is power used to charge the battery [kW], η_B is battery efficiency (includes round-trip efficiency).

The SOC of the battery is updated at each time step t using:

$$SOC_t = SOC_{t-1} + \frac{P_{ch}\eta_B - P_{dis}/\eta_B}{C_{BESS}} \tag{3.10}$$

where SOC_t is battery state of charge at time t, C_{BESS} is total battery capacity [kWh]. The battery operates within defined constraints to ensure longevity and optimal performance. Charging ceases once the SOC reaches its maximum limit (SOC_{max}), while discharging stops when the SOC drops to its minimum threshold (SOC_{min}). Additionally, a depth of discharge (DoD) limit is enforced to prevent excessive depletion, minimizing degradation and extending the battery's lifespan.

The lifetime throughput of the BESS for each point in the lifetime curve is calculated using the following equation [3], [54]:

$$Q_{Lifetime} = f\left(\frac{q_{max}V_{nom}}{1000}\right) DoD \tag{3.11}$$

where $Q_{Lifetime}$ is the lifetime throughput [kWh], f is the number of cycles to failure, DoD is the depth of discharge [%], q_{max} is the maximum capacity [Ah], V_{nom} is the nominal voltage [V].

Unlike generators, BESS incur no fuel costs, leading to an effectively zero fixed energy cost.

The marginal energy cost includes both battery wear and energy costs. The battery energy cost is calculated by dividing the total charging cost by the total energy stored. In a load-following strategy (LF), the energy cost is nearly zero, as the battery charges with surplus energy [3]. However, in a cycle-charging strategy (CC), where the generator operates at full capacity and excess energy is used to charge the battery, the energy cost becomes important. The battery wear cost (C_{bw}) is calculated as [3], [56]:

$$C_{bw} = \frac{C_{r,b}}{N_b Q_{Lifetime} \sqrt{\eta_{rt}}} \tag{3.12}$$

where C_{bw} is the battery wear cost [$/kWh], $C_{r,b}$ is the replacement cost of the battery bank [$], N_b is the number of batteries in the battery bank, $Q_{Lifetime}$ is the lifetime throughput of a single battery [kWh], and η_{rt} is the round-trip efficiency [%].

The formula for calculating battery energy cost ($C_{be,n}$) which is significant in a CC strategy, is given as:

$$C_{be,n} = \frac{\sum_{i=1}^{n} C_{cc,i}}{\sum_{i=1}^{n} E_{bc,i}} \tag{3.13}$$

where $C_{be,n}$ is the battery energy cost at time step n [$/kWh], $C_{cc,i}$ is the cost associated with charging the battery storage at time step i [$], $E_{bc,i}$ is the amount of energy put into the battery at time step i [kWh].

Grid Modeling: In a grid-integrated MG system, the grid can be considered as a component from which the MG system can purchase AC electricity and to which it can sell AC electricity [3], [56]. Accurate grid modeling is essential for optimizing performance, ensuring reliability, and achieving economic efficiency. This involves simulating interactions between the MG and the main grid while considering key parameters such as grid sell and purchase capacity (kW), net metering policies, energy pricing ($/kWh) including grid tariffs and sell-back rates, demand charges ($/kW/mo), grid emissions, interconnection fees ($), standby charges ($/yr), and grid outages.

Grid outages are modeled as time periods during which no electricity can be exchanged with the grid. Parameters such as mean failure frequency, mean repair time, and repair time variability define random outages throughout the year [54]. During these events, the MG transitions to island mode, ensuring an uninterrupted power supply to critical loads and enhancing system resilience.

As a dispatchable power source, the grid's fixed and marginal energy costs are also considered. The fixed cost is zero, while the marginal cost equals the real-time grid power price plus any emission-related penalties [56]. In this research, grid emissions are assumed to be negligible, given that wind and hydro dominate the power generation mix [3].

3.3.3 Energy System Dispatch Strategy

Beyond modeling individual components, it is essential to analyze their collective operation as a system. This requires making real-time decisions at each time step, including which generators to activate, their output levels, battery charge or discharge status, and grid transactions [54], [56], [73]. The dispatch strategy in MG governs these decisions to ensure efficient, reliable, and cost-effective operation. It directly influences economic performance, fuel consumption, and overall sustainability by balancing supply and demand while considering operational constraints, grid interaction, and energy storage. To maintain system reliability, the simulation ensures that available capacity always meets or exceeds the required demand at each time step [3], [56]. The required operating capacity (P_{rc}) and required operating reserve (P_{res}) are given as:

$$P_{rc} = P_{Ld} + P_{res}; \quad P_{res} = 10\% * P_{Ld} + 20\% * P_{PV} + 30\% * P_{WTG} \tag{3.14}$$

where P_{Ld} is the electrical load demand [kW], P_{res} is the required operating reserve [kW], P_{PV} is the PV power output [kW] and P_{WTG} is the WTG power output [kW].

At each time step, the output from non-dispatchable sources, PV and WT, is expected to meet the load demand and the required operating reserve. If their generation is insufficient to meet

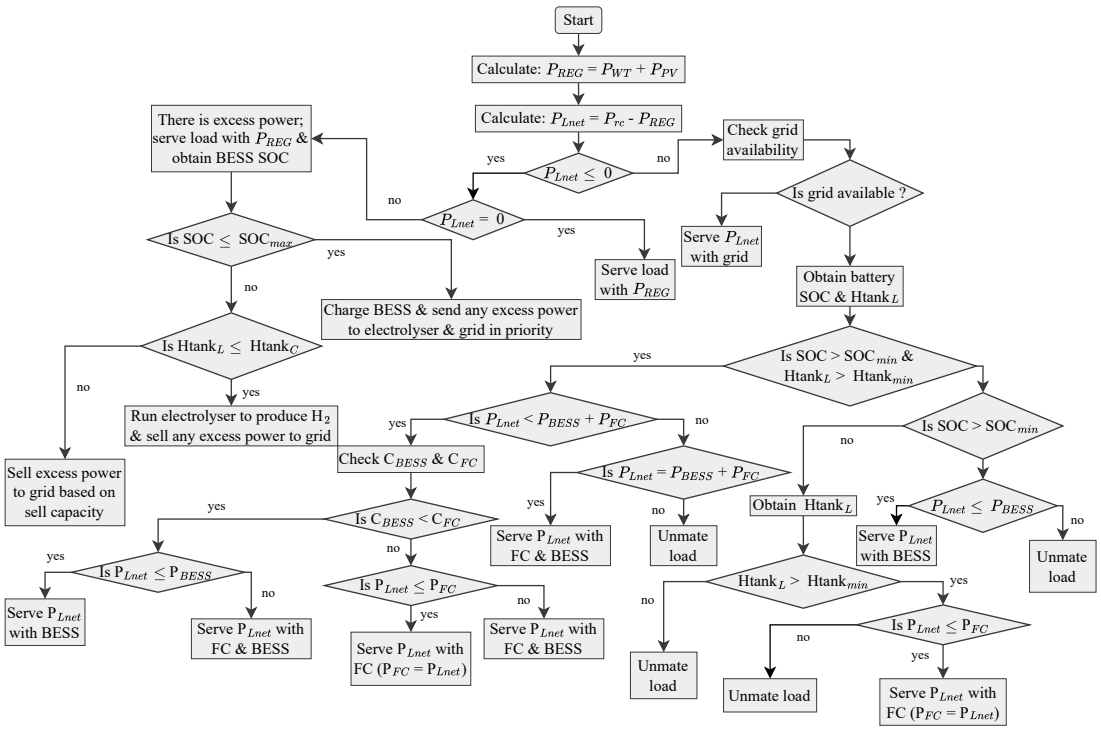

Fig. 3.6: Load-following dispatch strategy in a grid-integrated microgrid showing interaction between local generation, storage, and the utility grid.

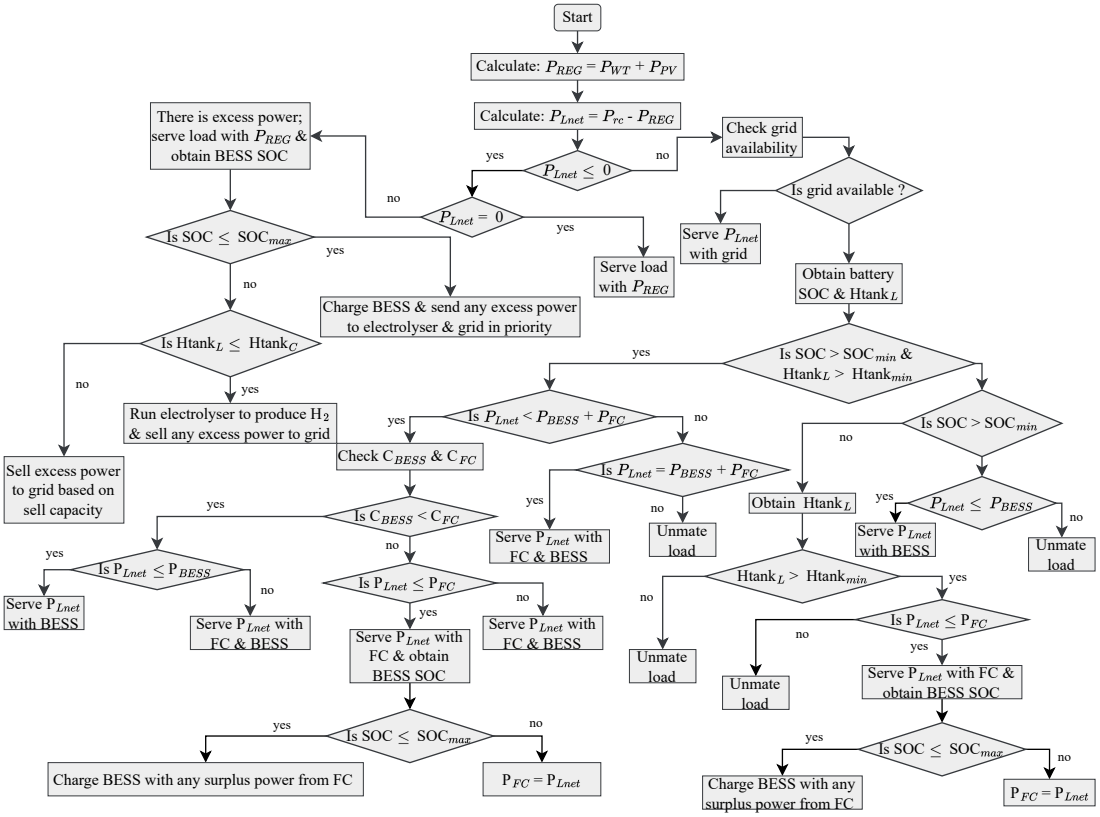

Fig. 3.7: Cycle-charging dispatch strategy in a grid-integrated microgrid showing interaction between local generation, storage, and the utility grid.

load demand, dispatchable sources, including PEMFC, BESS, and the utility grid, are allocated to supply the remaining net load and maintain system energy balance [3], [54], [56]. The net load is calculated as:

$$P_{Lnet} = P_{rc} - P_{REG}; \quad P_{REG} = P_{WTGs} + P_{PV} \tag{3.15}$$

where P_{Lnet} represents the net load demand [kW], and P_{REG} is the total renewable power generation [kW]. The net load P_{Lnet} can be negative (excess generation), zero (balanced demand and supply), or positive (deficit requiring dispatchable sources).

An optimized dispatch strategy is essential for balancing economic efficiency, environmental performance, and system resilience. By prioritizing renewable energy and minimizing fuel consumption, the strategy reduces both operating costs and emissions. In hybrid systems that prioritize local generation, the utility grid may function as a secondary source during periods of insufficient local supply. The environmental benefits depend on the grid's generation mix: renewable-dominated grids reduce emissions, while fossil fuel-reliant grids can increase the

overall carbon footprint, offsetting local gains.

Building on this, MG can operate in grid-connected or islanded mode, and the dispatch strategy must be adaptable to both scenarios. In grid-connected mode, the utility grid serves as a secondary source, providing power when local renewable generation is insufficient or when grid electricity is economically favorable (see Fig.3.8). The surplus energy from local generation is prioritized to charge the BESS. Any remaining excess energy powers the electrolyzer for hydrogen production. Further surplus energy is then exported to the grid, subject to net metering policies and tariff structures. During grid outages, the MG transitions to island mode, prioritizing local generation and storage to support critical loads. In dynamic studies, advanced control mechanisms facilitate seamless transitions between modes, enhancing overall system resilience and reliability.

Energy dispatch strategies in MG differ in how generators operate to meet real-time load demand and manage surplus energy. One approach ensures that the generator produces only the power required to meet the net load at any given moment, while excess renewable energy is utilized for secondary purposes such as charging the battery or supplying deferrable loads [3], [54]. This method reduces fuel consumption and unnecessary generator operation, leading to lower costs and emissions (see Fig.3.6). However, since the generator does not always run at optimal efficiency, its fuel utilization may be suboptimal. In contrast, another strategy runs the generator at full capacity whenever it is turned on, with surplus energy directed to battery charging, deferrable loads, or even electrolyzer operations (see Fig.3.7). Although this approach maximizes generator efficiency, it can lead to higher operational costs, particularly when fuel prices are high [56], [73]. For generators with high fuel costs, such as hydrogen-powered PEMFC systems, the preferred strategy is to follow the net load demand. This approach minimizes fuel consumption by prioritizing the generator to supply only the net load [3].

3.3.4 System Economic Modeling

To achieve minimum total investment costs and meet technical and emission constraints, one of the key issues in renewable integrated MG design is optimal planning of DER in the MG setup. The optimization tools and techniques used for the optimal design of renewable-integrated MG are reviewed in [74]. One of the most powerful tools for this purpose is HOMER Pro [3], [4]. Table 3.1 provides possible decision variables and limits for optimal components sizing. The component specifications and economic parameters for the DER used in this research are given in the article [3], where detailed information can be found. Based on the input data, the optimal planning and optimization of grid-integrated MG are determined.

Determining the optimal sizing of DER involves various methods and techniques, one of which is evaluating the life cycle cost (or net present cost) of each component. Life cycle

Table 3.1: The input data for components possible decision variables.

Component	Decision Variables	Unit
Grid	2, 2.52, 4.23	MW
PV	0 - 20	MW
WTG	0, 1, 2, 3, 4	no
PEMFC	2.5, 3, 3.5, 4, 4.5	MW
BESS	0 - 1600	no
PEME	3, 3.5, 4, 4.5	MW
HTank	3, 3.5, 4, 4.5	MW
Conv	0 - 6	MW
DS	LF, CC	-

cost represents the present value of all installation and operational costs throughout the lifetime of the project, minus the present value of all revenues earned during the same period [3], [54], [57]. A key objective in optimizing DER is to minimize the total life cycle cost, which is treated as the objective function in the optimization problem. This objective aims to minimize costs while simultaneously meeting relevant constraints, such as energy balance and economic feasibility. The cost (objective function) to be minimized is formulated as:

$$\min\ C_{NPC} = \sum_{t=0}^{n} f_{d,n}\left(C_c + C_r + C_{O\&M} + C_{Fg} + C_G - C_R\right) \tag{3.16}$$

where C_c, C_r, $C_{O\&M}$, C_{Fg}, C_G, and C_R are the capital cost, replacement cost, operation and maintenance cost, generator fuel cost, cost of purchase of power from the grid, and revenue cost, respectively. $f_{d,n}$ is the discount factor.

By minimizing the objective function C_{NPC} while satisfying these constraints, the optimal sizing and dispatch of DERs are determined to ensure both economic and technical efficiency.

The discount factor and the annual real discount rate can be calculated from the nominal discount rate and expected inflation rate as [57], [59], [75]:

$$f_{d,n} = \frac{1}{(1+i)^n}; \quad i = \frac{i^{'} - f}{1+f} \tag{3.17}$$

where n is the project life time which is 25 year in this project, where i is real discount rate, $i^{'}$ is nominal discount rate which is taken as 8 % and f is expected inflation rate which is taken as 7 %.

3.4 Results and Discussion

This section presents the key optimization results, comprehensively evaluating the proposed system's performance. The analysis highlights the advantages and sustainability of the optimized supply option, demonstrating its technical and economic feasibility for the selected industrial load. Furthermore, the results offer insights into the system's potential to enhance energy resilience, minimize carbon footprint, and ensure long-term operational viability.

3.4.1 Evaluation of Optimization Results

In pursuit of a sustainable and resilient energy transition, the proposed system shifts from the unreliable utility grid, which typically relies on diesel generators as backup during interruptions, to a fully renewable-based solution. This is achieved through an optimized hybrid configuration that integrates PV panels, WT, BESS, and hydrogen technology, as shown in Fig. 3.3.

In the conventional system, the industrial load is served primarily by the grid, with a 5 MW diesel generator available as backup during outages. While this setup requires no upfront capital investment (CAPEX), its economic and environmental drawbacks are substantial. The frequent and prolonged grid outages necessitate extensive diesel generator operation, leading to excessive fuel consumption, high operating expenses (OPEX), and significant carbon emissions. Specifically, the DG operates for 3 746 hours annually, consuming $\$2.5\ M/yr$ in fuel costs and emitting 6 677.8 t/yr of CO_2. Consequently, the conventional system incurs the highest total net present cost (NPC) of $\$108\ M$ and an annual OPEX of $\$4.87\ M$, as detailed in Table 3.2. Moreover, the system incurs higher demand and energy costs, further intensifying its financial inefficiency (Fig. 3.9b).

To address the economic and environmental drawbacks of the conventional system, the proposed hybrid configuration transitions to a fully renewable-based approach (see Fig. 3.3). This system integrates solar PV, WT, BESS, and hydrogen technologies to ensure a sustainable and self-sufficient power supply. By harnessing on-site renewable resources, it reduces reliance on imported diesel fuel, significantly lowering OPEX and emissions. Notably, the system achieves a 67.87% reduction in LCOE, dropping from 0.221 $/kWh in the conventional system to just 0.071 $/kWh. This reduction underscores the long-term cost-effectiveness of the optimized hybrid system, even with its higher initial CAPEX.

Table 3.2: Optimal economic and environmental results of the base case and proposed system.

System Configuration	NPC [$M]	CAPEX [$M]	OPEX [$M]	C_{Fg} [$M/yr]	CO_2e [t/yr]	$LCOE$ [$/kWh]
Base Case	108	0	4.87	2.5	6,677.8	0.221
Proposed System	57.9	41.9	0.72	0	0	0.071

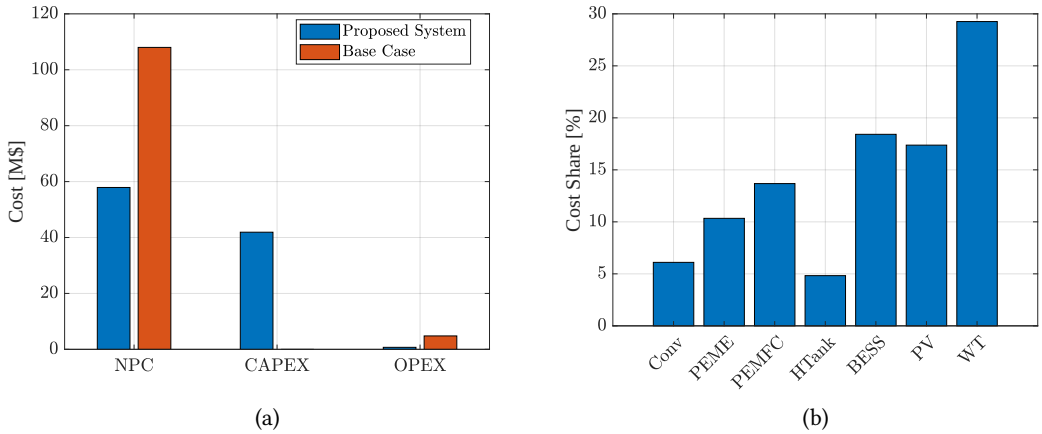

Fig. 3.8: (a) Financial Metrics Overview. (b) Components Cost Share.

To effectively implement this transition, the system is designed with an optimal configuration that balances generation, storage, and reliability. The optimized system configuration consists of a 4.23 MW grid connection, 15.2 MW of solar PV capacity, and four WT, each rated at 3 MW. Additionally, the system includes a 3 MW PEMFC, 3.5 MW PEME, 815 BESS units (each with a 60 Ah rated capacity), and a 6 MW power converter. Despite requiring the highest CAPEX of $\$41.\ M$, this configuration achieves a remarkable cost reduction by eliminating fossil fuel dependency. As a result, the total NPC is significantly lowered to $\$57.9\ M$, and the OPEX is minimized to $\$0.72\ M$, as indicated in Table 3.2. From the component cost breakdown shown in Fig. 3.8b, it can be observed that the investment in wind turbines accounts for the highest share, followed by BESS, PV, and PEMFC.

To efficiently manage power generation and consumption, the system employs a cost-effective dispatch strategy: non-dispatchable sources (PV and WT) are utilized to their maximum potential, while dispatchable units (grid, BESS, and PEMFC) are engaged as needed to ensure a balanced power supply and reliability.

The BESS stores surplus energy from PV and WT and discharges it when needed to meet the load. If both renewable generation and BESS discharge are insufficient, the PEMFC is activated to supply the net demand. The dispatch of each unit is guided by its marginal production cost, as summarized in Table 3.3.

According to the demand charge rate of 2.84 \$/kW of EEU for 15 kV & 33 kV lines [44], the demand charge is high as depicted in Fig.3.9b (left-side y-axis), which needs revising EEU demand charge regulations to support grid integration of DER. However, the system takes only 6.07% of total annual electrical energy from the utility grid while 93.93% of total electricity demand is supplied by renewable energy sources, as illustrated in Fig. 3.9a. This implies that

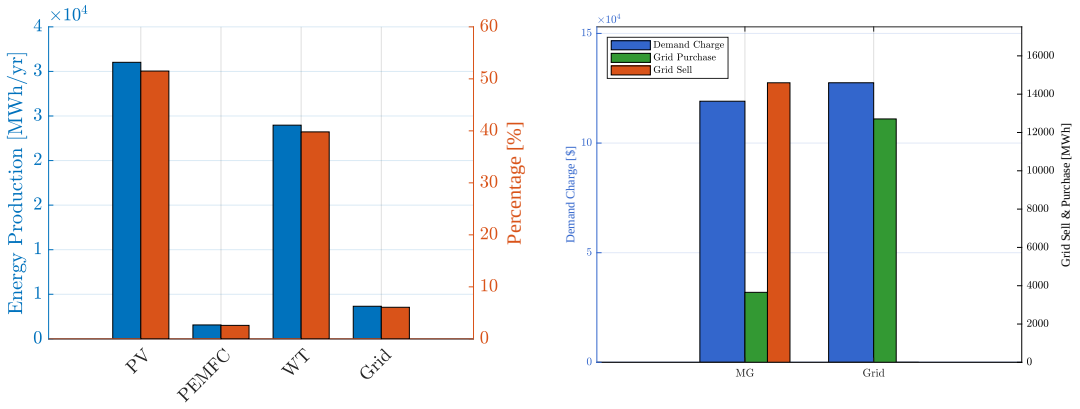

Fig. 3.9: (a) Energy production. (b) Demand Charges, Grid Sales, and Grid Purchases

the system depends less on grid electricity consumption which in turn saves much on utility bills. Even though the initial capital investment dominates, which is about 73% of total system cost, it is noted that the operation cost is very low and no fuel costs are incurred (see Table 3.2). When we see the annual electrical energy production of each generation unit as shown in Fig.3.9a, the PV system and WT hold a high share of electrical energy production. From the total annual electricity production of 60 207.0 MWh, the PV system and WT share 51.5% and 39.8% with capacity factor of 23.3 % and 22.8 %, respectively. The annual electricity production share of the grid and PEMFC generator account for 6.07% and 2.59% respectively. As shown in Fig.3.9b (right-side y-axis), this system not only charges the battery bank and produces hydrogen but also generates revenue by selling approximately 33.5 % of excess electricity to the grid. This additional income contributes to the system's lower NPC. This implies the deployment of PV and WT at the site is achievable and productive.

3.4.2 Evaluation of the Impact of Renewable Energy Integrated Microgrid Based on Energy Balance Simulation Outputs

A renewable energy-integrated MG, illustrated in Fig. 3.3, offers a promising solution to the challenges of an unreliable utility grid with frequent outages. This system leverages PV panels, WT, BESS, and PEMFC to ensure a reliable energy supply. Under normal grid-connected

Table 3.3: Results of energy production cost of dispatchable units.

Dispatchable Unit	Fixed Cost	Marginal Cost
BESS	0 $/hr	0.102 $/kWh
PEMFC	530 $/hr	0
Grid	0 $/hr	0.07 $/kWh

conditions, PV and WT serve as the primary energy sources, meeting the industrial load while excess energy is either stored in BESS, used for hydrogen production via electrolyzers, or exported to the grid [3]. When renewable generation is insufficient, the grid supplies the net load, ensuring uninterrupted power for the industrial facility. By incorporating flexible loads like electrolyzers and grid connectivity, the system actively manages the net load, adjusting power consumption based on renewable energy availability while ensuring uninterrupted operation of the industrial facility. This optimization improves efficiency, reliability, and overall cost-effectiveness.

However, during a grid outage, the microgrid seamlessly transitions into island mode, ensuring uninterrupted power delivery. This transition occurs when there is no power exchange with the grid, indicated by the absence of both imports and exports, as shown in Fig. 3.11a. In island mode, the microgrid prioritizes renewable resources, solar PV and WT, to meet the industrial load demand. When renewable generation is insufficient, BESS provides an immediate response, while PEMFC serves as a long-duration backup. The dispatch priority between BESS and PEMFC is determined based on energy production costs (Table 3.3) and an optimized dispatch strategy, as detailed in Fig. 3.5. By coordinating energy dispatch efficiently, this approach enhances resilience and ensures critical loads remain powered without disruption.

To further analyze the role of energy storage and flexible loads in maintaining a reliable power supply, the simulation results for the grid-integrated MG in Fig. 3.3 provide insights into the optimized hybrid MG configuration under different conditions. The optimal dispatch strategy, illustrated in Fig. 3.5a, ensures a balance between supply and demand at each time step. The MG adjusts generation unit output based on resource availability, prioritizing renewable sources whenever possible. However, due to the inherent variability of solar and wind resources, generation fluctuates, resulting in surplus power at certain times and supply deficits at others. In such cases, dispatchable sources, including the grid (when available), PEMFC, and BESS, operate according to their designated priority (Table 3.3) to minimize unmet load. This coordinated dispatch strategy enhances energy reliability and reduces renewable power curtailment, ensuring efficient resource utilization.

The simulation output identifies two operating modes: island mode, where there are no grid transactions (i.e., no import or export of power), and grid-connected mode, where power is either imported from or exported to the grid (see Fig. 3.11a). The optimal dispatch strategy for the microgrid, depicted in Fig. 3.3, is detailed in Fig. 3.5a. To maintain a balance between supply and demand in each time step, each generation unit dispatches power according to the system's optimal dispatch strategy. The simulation data is based on the first two weeks of January. Fig. 3.10 depicts the hourly power generation from renewable sources, PV and WT (Fig. 3.10a), and hourly energy consumption, including electrical load (Fig. 3.10b) and electrolyzer usage (Fig. 3.10c).

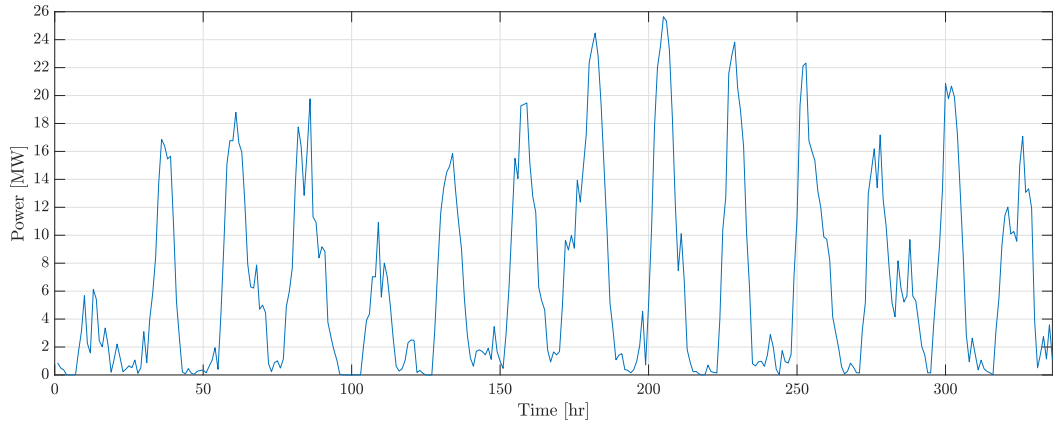

(a)

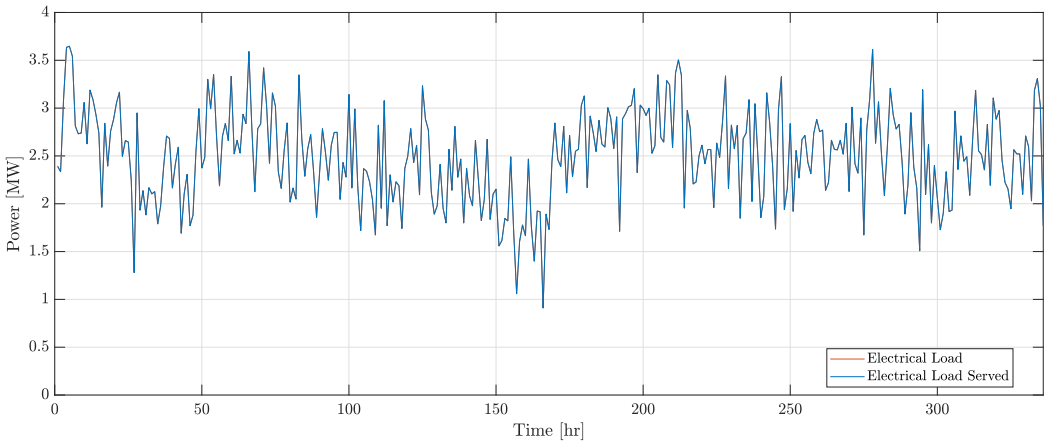

(b)

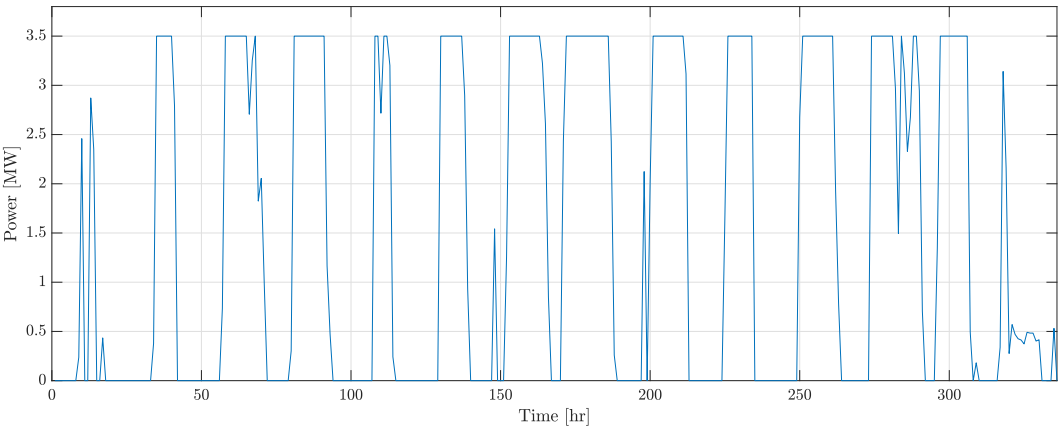

(c)

Fig. 3.10: Hourly power output from renewable energy sources alongside load demand: a) Power output from renewable energy sources (PV and WT), (b) Electrical load and load served, (c) Power consumption of electrolyzer.

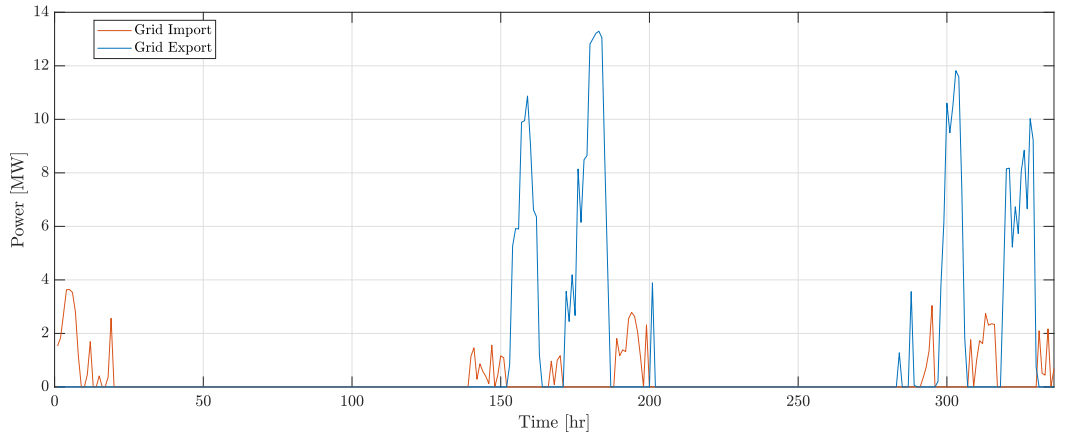

(a)

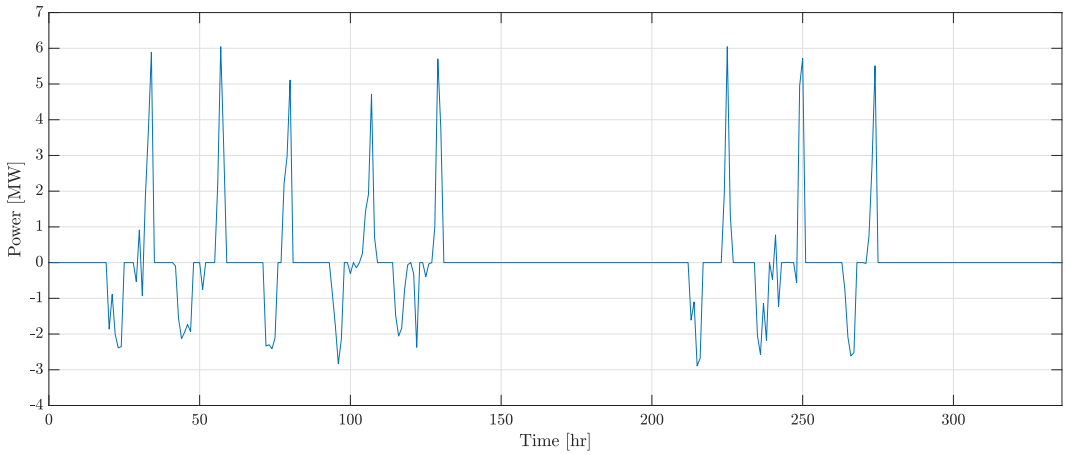

(b)

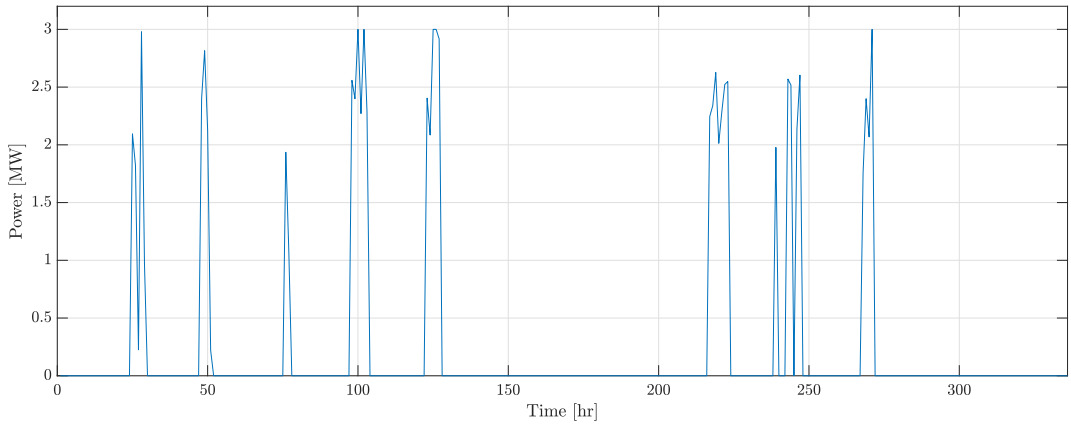

(c)

Fig. 3.11: Power output of dispatchable energy sources: (a) Power transactions with the grid, (b) BESS input power, (c) PEMFC power output.

Electrolyzers serve as flexible energy assets, capable of quickly adjusting to grid conditions [76]. They can absorb excess electricity during periods of oversupply or generate electricity when paired with fuel cells to meet peak demand (Fig. 3.10c). In addition, electrolyzer systems can store surplus electricity by converting it into hydrogen through a Power-to-Gas (PtG) process. This dual functionality makes electrolyzers essential for maintaining energy balance in our study. They also play a crucial role in providing ancillary services, such as frequency regulation, voltage control, and congestion management, as part of dynamic grid management [76], [77].

Fig. 3.11 illustrates the hourly output of dispatchable sources, which supply power according to their designated dispatch strategy. The hourly grid import and export are shown in Fig. 3.11a, where the absence of grid transactions indicates island mode, while the presence of either import or export signifies grid-connected operation during the first two weeks of January. Additionally, Figs. 3.11b and 3.11c depict the power input to BESS and the power output from PEMFC, respectively, under both operating modes, emphasizing the distinct dispatch characteristics of each mode.

In each time step, the dispatchable sources operate to minimize (or avoid) unmet load. Given the trade-off between high system reliability and minimizing renewable energy curtailment in systems with high renewable penetration, the optimal sizing of energy storage devices is crucial. This comprehensive energy management strategy ensures a reliable and sustainable power supply, positioning the microgrid as a resilient solution for industrial applications in areas with unreliable grid infrastructure.

3.4.3 Hydrogen Production and Decarbonization Potential of the Proposed System

In the proposed system configuration, surplus electricity, beyond what is injected into the grid, is harnessed to charge the battery bank and produce electrolytic hydrogen, thereby maximizing the utilization of renewable energy. The electrolyzer consumes 6 852.44 MWh annually, producing 147 665 kg of hydrogen per year. The simulation results of the optimized MG (see Fig.3.1) show that 65 656 kg/yr of hydrogen is allocated to FCEVs, while 77 964 kg/yr is consumed by the PEMFC generator, as detailed in Table 3.4. This efficient integration of renewable hydrogen serves dual purposes, both for power generation and transportation, further enhancing the system's sustainability and energy independence.

The integration of renewable hydrogen into both power generation and road transportation represents a significant advancement in reducing dependence on fossil fuels. By substituting gasoline consumption in both backup diesel generator and conventional vehicles, this system presents a practical pathway toward deep decarbonization. According to existing literature [59], [78], 1 kg of hydrogen is equivalent to 2.75 kg of gasoline in terms of lower heating value.

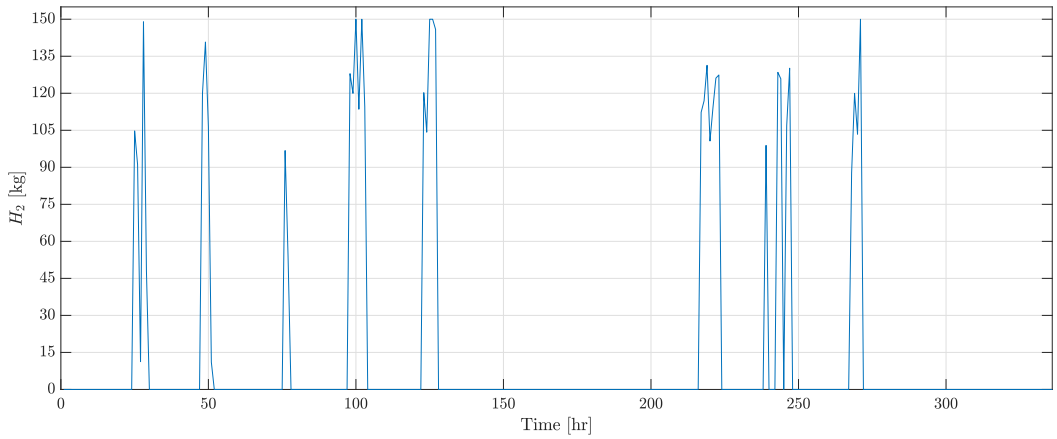

(a)

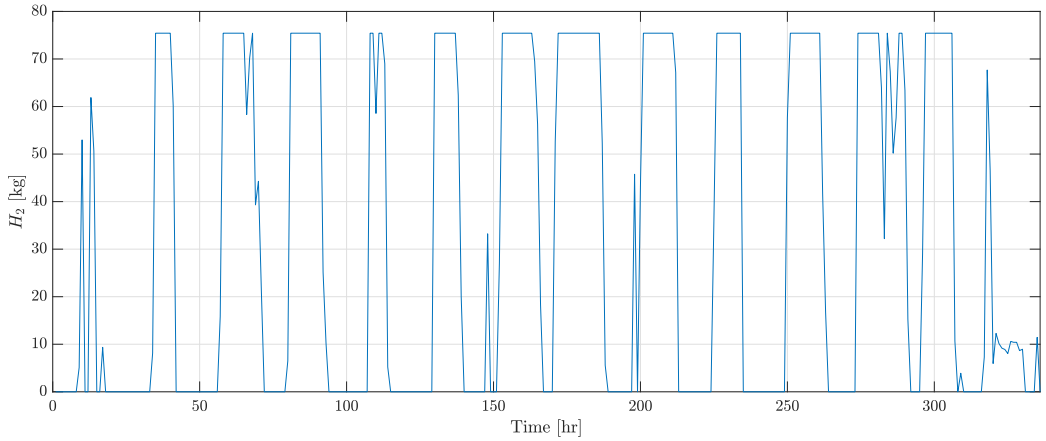

(b)

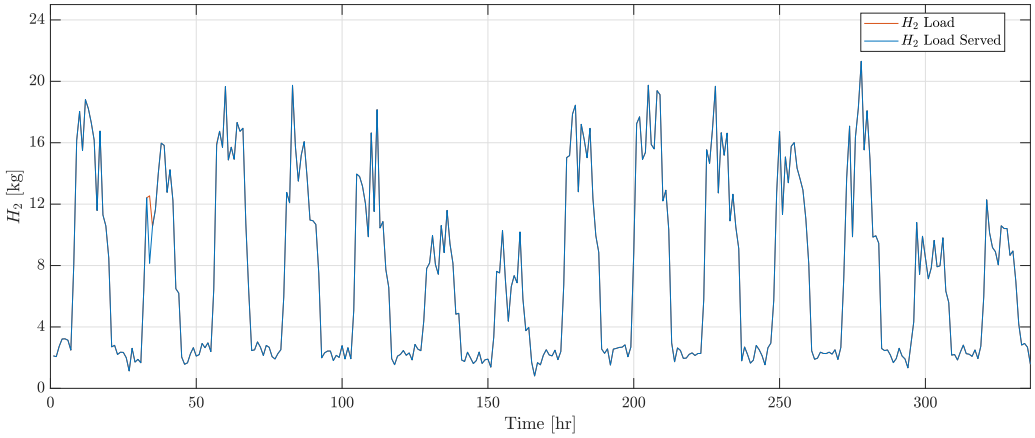

(c)

Fig. 3.12: (a) Hourly hydrogen input to the PEMFC. (b) Hourly hydrogen output from the PEME. (c) Hourly hydrogen load profile and the load served.

Table 3.4: Decarbonization potential of renewable hydrogen production.

Hydrogen Consumers (Hydrogen Loads)	Total Hydrogen Consumption [kg/yr]	Equivalent Gasoline Consumption [kg/yr]	Corresponding CO_2 Emissions [kg/yr]	Money Saved [$/yr]
PEMFC	77 964	214 401	643 203	328 805.4
FCEV	65 656	180 554	541 662	276 897.6
Total	143 620	394 955	1 184 865	605 703.0

Based on this conversion factor, the proposed system's hydrogen adoption replaces 394 955 kg of gasoline annually, as shown in Table 3.4.

Beyond displacing fossil fuels, the system delivers notable environmental and economic advantages. The combustion of 1 kg of gasoline generates approximately 3 kg of CO_2 emissions [59], [79]. Based on this conversion factor, the values reported in Table 3.4 indicate that the system prevents the release of 1,184,865 kg of CO_2 emissions annually. Additionally, it achieves annual fuel cost savings of$605,703 through the use of 143,620 kg/yr of hydrogen.

Fig. 3.12a illustrates the hourly hydrogen input to the PEMFC during the first week of January, highlighting the system's hydrogen consumption patterns. In parallel, Fig. 3.12b presents the hourly hydrogen output from the electrolyzer over the same period, demonstrating the production of hydrogen to support both the PEMFC and 30 FCEVs. Notably, as shown in Fig. 3.12c, there is no unmet hydrogen demand during each hour of the simulation for the first week of January, ensuring that the system operates smoothly without any shortfall in hydrogen supply. This consistency in supply and demand highlights the system's efficiency in balancing hydrogen production and consumption, ensuring reliable operation throughout the period.

These results underscore the transformative potential of renewable hydrogen in industrial MGs. By offering a sustainable, cost-effective, and emissions-free alternative to conventional fossil fuel-based systems, this integrated solution not only contributes to environmental preservation but also fosters long-term economic resilience.

Chapter 4

Advanced VSC-Based Islanded Microgrid Control: Impedance Method and Computational Intelligence-Driven Optimization

4.1 Introduction

In recent years, the growing demand for cleaner and smarter power supply has accelerated the deployment of DER, including RES, conventional DG, and ESS, within low and medium voltage power networks. These resources, however, introduce operational complexities due to their intermittent nature, decentralized configuration, and the absence of inherent inertia. As a result, advanced power electronic interfaces are essential to ensure reliable integration, effective control, and flexible operation under diverse grid conditions.

The Voltage Source Converter (VSC) has emerged as a key enabling technology in modern power systems. Serving as the primary interface between distributed energy resources (DER) and the grid, the VSC converts DC voltage to AC and enables independent control of active and reactive power. Its use of self-commutated semiconductor switches, such as Insulated Gate Bipolar Transistors (IGBTs), allows it to generate stable AC outputs without relying on an external voltage source. These capabilities offer crucial advantages, including voltage and frequency regulation, black start capability, and reliable operation in islanded or weak grid environments [80]–[82]. Compared to the Current Source Converter (CSC), which depends on synchronous AC voltages for commutation, the VSC provides faster dynamic response, improved power quality, and greater flexibility—making it especially well-suited for modern

DER-integrated MGs [80]–[83].

Building upon the capabilities of VSCs, MGs enhance the coordination and operation of DER by clustering them within a defined electrical boundary. MGs can operate in either grid-connected or islanded mode, with the latter being essential when the main grid is unavailable—requiring the MG to maintain voltage and frequency stability independently. In such scenarios, VSCs play a critical role as grid-forming units, providing the necessary control and flexibility to ensure seamless transitions and sustained operation without reliance on the main utility supply [3], [4], [84]–[87].

To facilitate autonomous operation in islanded mode, VSCs often adopt a cascaded control structure, with each layer responsible for a specific control objective. This hierarchical scheme typically consists of an inner current control loop, an outer voltage control loop, and a power-sharing control loop. The inner current loop provides fast dynamic response and protects the converter from overcurrent conditions. The outer voltage loop regulates the output voltage by generating appropriate current references for the inner loop. Meanwhile, the power-sharing loop manages the distribution of active and reactive power among DER, adjusting voltage amplitude and frequency to remain within statutory limits.

While optimizing external power control is important for enhancing the performance of islanded MG, this study focuses on refining the low-level control loops within the VSC—specifically, the inner current and outer voltage control loops. These loops are responsible for current tracking and voltage regulation, respectively, and their effectiveness is critical for maintaining system stability and performance under islanded conditions. However, the dynamic behavior of these control loops is strongly influenced by the characteristics of the AC-side interfacing filter, which introduces significant challenges in control design and tuning [88].

To ensure effective attenuation of high-frequency switching harmonics while maintaining control performance, filter design has evolved from simple L filters to more advanced configurations such as LC and LCL filters. Among these, the LCL filter is particularly attractive due to its superior harmonic suppression, offering an attenuation slope of 60 dB/decade beyond the resonance frequency—compared to 40 dB/decade for LC and 20 dB/decade for L filters. Despite the added design complexity, LCL filters provide improved power quality without substantially increasing system cost [89], [90].

However, the use of LCL filters introduces additional control challenges. The resonance inherent in these filters can compromise system stability if not properly mitigated, particularly in islanded operation where converter-based regulation is critical. Both passive and active damping strategies are commonly applied to address this issue. Active damping offers superior performance but at the cost of added control complexity. Passive damping—typically

implemented by placing resistors in series or parallel with the filter capacitor—offers a simpler alternative but can lead to increased losses, reduced efficiency, and degraded dynamic response if not carefully designed [91]–[93].

To address these interrelated challenges—specifically, improving current tracking, voltage regulation, and the effective damping of resonance in LCL filters—this study proposes two distinct control approaches that strengthen the low-level performance of VSC-based microgrids. These improvements at the converter level inherently support more stable frequency behavior and enable more accurate power sharing in islanded operation. The first approach introduces a virtual complex impedance-based control strategy, which enhances transient response, system stability, and power sharing accuracy by shaping the converter's output impedance to better coordinate with the dynamic characteristics of the interfacing filter and electrical network. The second approach applies a simulation-based, computational optimization framework that systematically tunes control parameters to adapt to varying operating conditions, further enhancing the robustness and responsiveness of the converter's inner and outer control loops.

Each approach is introduced and evaluated in turn, with attention to both their capabilities and the inherent design trade-offs they entail. This dual-perspective analysis illustrates the transition from impedance-based coordination strategies toward optimization-driven control methods for advanced MG applications.

4.2 System Description and Modeling

Fig. 4.1 illustrates an MG composed of interconnected loads and DER, including RES, ESS, and controllable loads with their respective interfaces. The MG can operate in islanded mode either intentionally—for maintenance or economic purposes—or unintentionally due to main grid failures caused by network faults [87], [94]. Islanding is achieved by opening the isolating switch (shown in Fig. 4.1), which disconnects the MG from the main grid. Once islanded, the DER units must independently regulate the system's voltage and frequency while coordinating their output to meet load demand through appropriate active and reactive power sharing.

Fig. 4.2 shows a typical islanded single DER unit with a two-level VSC connected to an ideal DC voltage source and cascaded control loops. This unit supplies a local load and connects to a common AC bus via an LCL filter, with L_f and L_c as the inverter-side and coupling inductors, R_f and R_c as their parasitic resistances, and C_f as the filter capacitor. The DC-side voltage is assumed to be tightly regulated by the DER unit, allowing the DC-side dynamics to be considered negligible. Additionally, because the inverter operates at a high switching frequency (typically between 4 and 15 kHz), the effects of individual switching events are

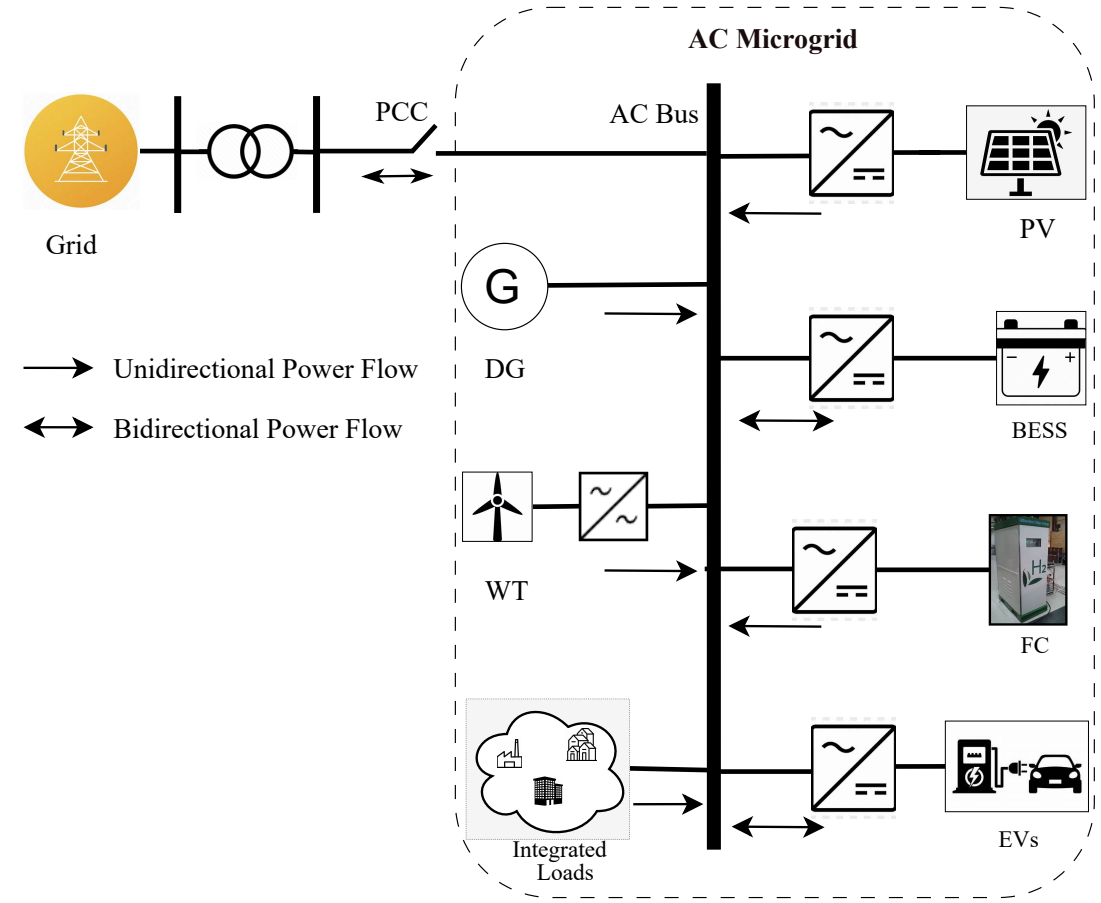

Fig. 4.1: Schematic of an Islanded AC Microgrid and Its Main Components

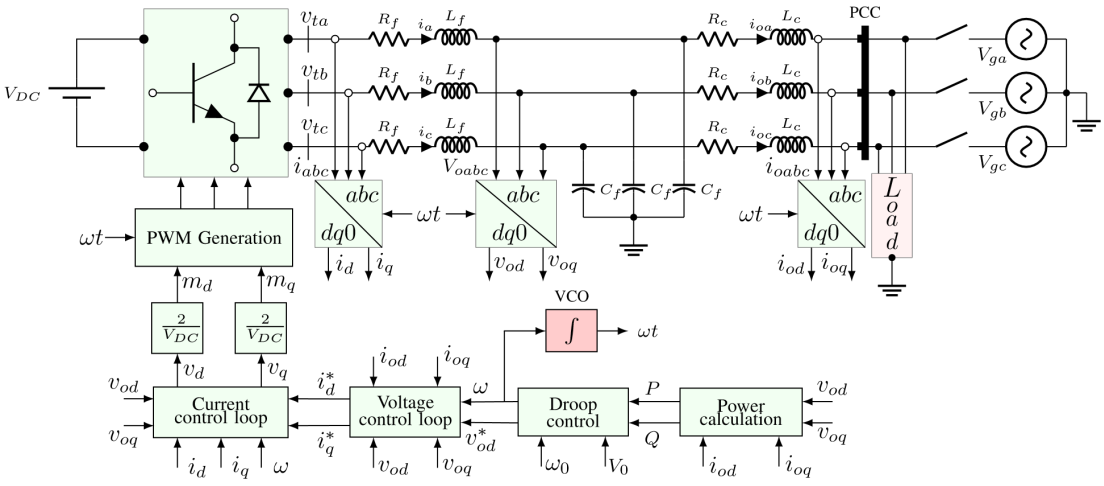

Fig. 4.2: The schematic depicts a VSC system employed in the case study.

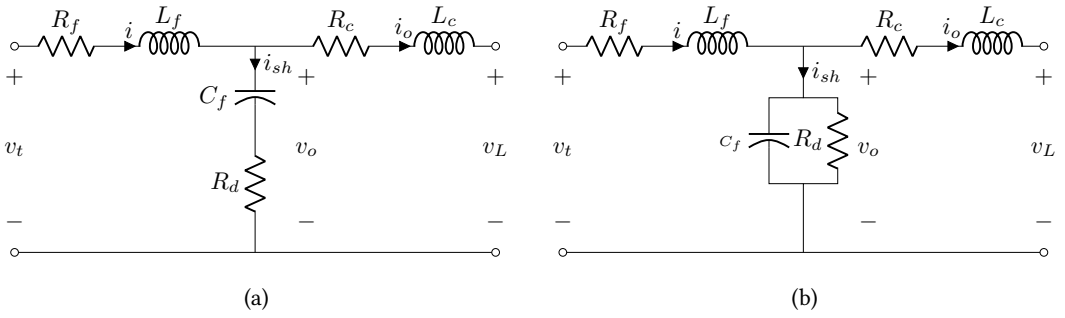

Fig. 4.3: Common configurations of passive damping techniques applied to the LCL filter.

averaged out and can be neglected in the system-level analysis [95], [96].

Figs. 4.3a and 4.3b show the per-phase representation of the LCL filter from Fig. 4.2, incorporating both series and parallel damping resistors to mitigate resonance. This allows for a comparison between the two configurations. Ignoring parasitic resistors in Fig. 4.3, one can analyze the transfer functions relating the output current i_o and the inverter-side current i to the inverter terminal voltage v_t as:

$$\frac{i_o(s)}{v_t(s)} = \frac{1}{L_f L_c C_f s^3 + (L_f + L_c)s} \tag{4.1}$$

$$\frac{i(s)}{v_t(s)} = \frac{L_c C_f s^2 + 1}{L_f L_c C_f s^3 + (L_f + L_c)s} \tag{4.2}$$

These transfer functions represent the worst-case damping performance. Based on Eqs. (4.1) and (4.2), the undamped resonance frequency ω_{res} of the LCL filter is given by:

$$\omega_{res} = \sqrt{\frac{L_f + L_c}{L_f L_c C_f}} \tag{4.3}$$

In this thesis, the authors propose a simple and cost-effective method to mitigate the resonance effect in LCL filter components by inserting resistors in series or parallel with the filter capacitor, as shown in Figs. 4.3a and 4.3b. This approach offers economic benefits, ease of construction, and a reduced component count [97], [98]. At high frequencies, the impedances of the resistors R_f and R_c are much lower than those of the inductors L_f and L_c, allowing the resistors' impact to be safely neglected. As a result, the transfer functions for series damping (Fig. 4.3a) and parallel damping (Fig. 4.3b) are modified from Eqs. (4.1) and (4.2) to Eqs. (4.4)

and (4.5), respectively.

$$\frac{i_o(s)}{v_t(s)} = \frac{R_d C_f s + 1}{L_f L_c C_f s^3 + (L_f + L_c) R_d C_f s^2 + (L_f + L_c) s} \tag{4.4}$$

$$\frac{i_o(s)}{v_t(s)} = \frac{1}{L_f L_c C_f s^3 + \frac{L_f L_c}{R_d} s^2 + (L_f + L_c) s} \tag{4.5}$$

As shown in Eqs. (4.4) and (4.5), series and parallel damping exhibit distinct characteristics. Series damping results in a 20 dB/decade attenuation slope due to a zero at $s = -1/R_d C_f$, but it also leads to higher power dissipation because of the filter capacitor's lower impedance at higher frequencies. In contrast, parallel damping maintains a steeper attenuation rate of 60 dB/decade (as shown in Fig. 4.4) and reduces power dissipation by exploiting the filter capacitor's lower impedance at higher frequencies. For high-power applications, parallel damping is typically the preferred choice.

The mathematical modeling of the VSC system depicted in Fig. 4.2 is based on the parallel damping configuration presented in Fig. 4.3b. The corresponding expressions for its active

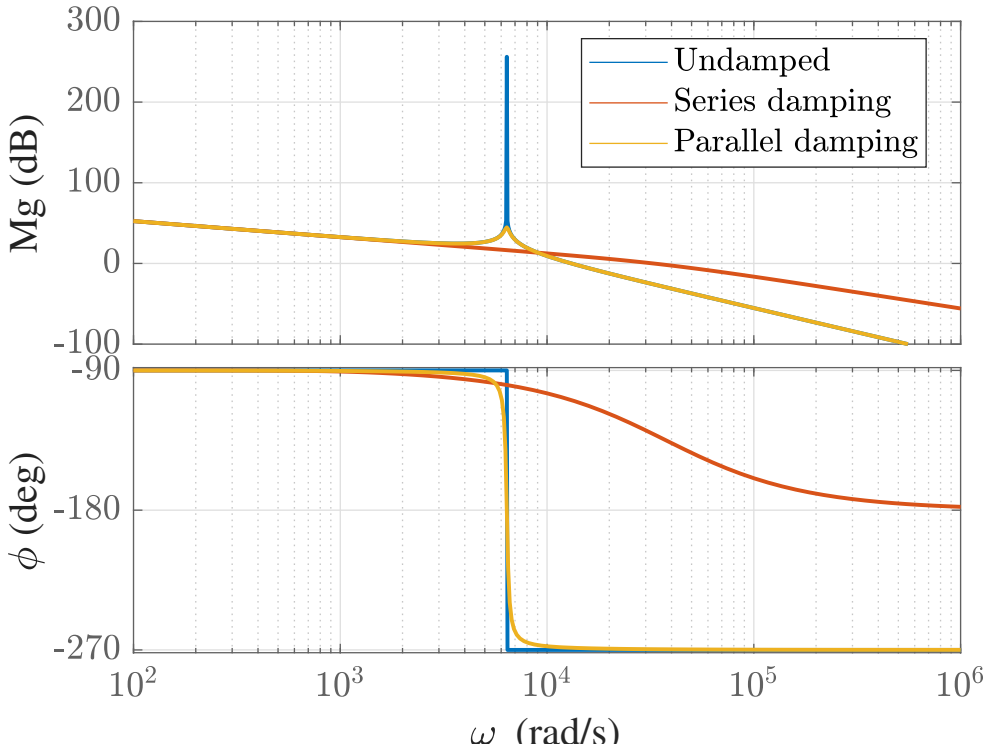

Fig. 4.4: Comparison of different configurations for passive damping strategies.

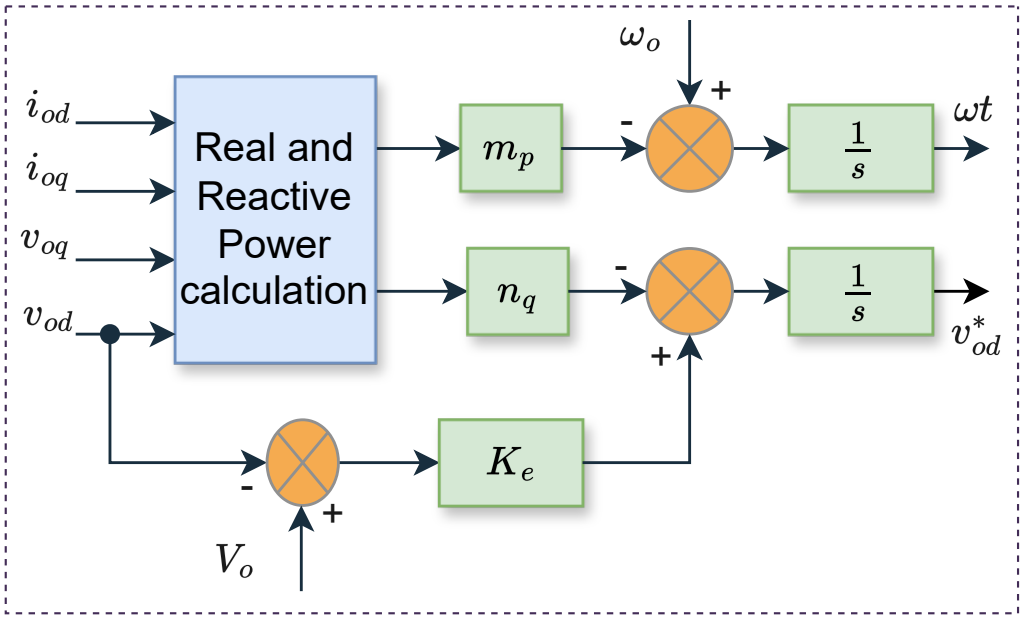

Fig. 4.5: Power controller.

and reactive power outputs, P and Q, are derived using the d–q frame transformation and are given by:

$$P = \frac{\omega_f}{s+\omega_f}\frac{3}{2}(v_{od}i_{od} + v_{oq}i_{oq})$$
$$Q = \frac{\omega_f}{s+\omega_f}\frac{3}{2}(v_{oq}i_{od} - v_{od}i_{oq}) \tag{4.6}$$

where ω_f is a cutoff frequency of a first-order low pass filter, which is one or two decades below the nominal frequency and employed to guarantee high noise rejection and fast transient response. In the power-sharing control loop, the VSC regulates the amplitude and frequency of its fundamental output voltage based on a predefined droop characteristic [87], [99]. As described in Eq. (4.6), the control of P and Q are governed by the control of the converter's dq-axis output currents, i_{od} and i_{oq}. By regulating the q-axis voltage component (v_{oq} to zero, the control of P and Q becomes decoupled, allowing them to be independently managed through i_{od} and i_{oq}, respectively. Based on methods from [100], [101], this study implements droop control in coordination with cascaded current and voltage control loops, all designed and analyzed within the synchronous dq reference frame. The corresponding control equations are given as:

$$\omega = \omega_0 - m_p P$$
$$\dot{v}^*_{od} = K_e(V_o - v_{od}) - n_q Q \tag{4.7}$$

For voltage amplitude control at steady state, the input to the integrator should be zero [100], and Eq. (4.7) can be given as:

$$v_{od} = V_o - \frac{n_q}{K_e} Q = V_o - \frac{n_q Q}{K_e V_o} V_o \tag{4.8}$$

in which v_{od} can be maintained within the desired range by selecting a large value of K_e. The droop coefficients n_q and m_p can be determined as usual by:

$$n_q = \Delta V \frac{K_e}{Q_n}; \qquad m_p = \frac{\Delta \omega}{P_n} \tag{4.9}$$

where $\Delta\omega$ and ΔV are the frequency droop and desired voltage drop ratio, P_n and Q_n are rated real power and reactive power, and V_0 is a nominal reference voltage amplitude.

With reference to Fig. 4.3b, the dynamic equation of a parallel C_f and R_d can be expressed in dq-frame as:

$$\begin{aligned} C_f \frac{dv_{od}}{dt} + \frac{v_{od}}{R_d} &= i_d - i_{od} + \omega C_f v_{oq} \\ C_f \frac{dv_{oq}}{dt} + \frac{v_{oq}}{R_d} &= i_q - i_{oq} - \omega C_f v_{od} \end{aligned} \tag{4.10}$$

Likewise, the inner current controller is designed based on the dynamics of the converter-side inductor current i, described in the dq-frame as:

$$\begin{aligned} L_f \frac{di_d}{dt} + R_f i_d - \omega L_f i_q + v_{od} &= \frac{V_{DC}}{2} m_d \\ L_f \frac{di_q}{dt} + R_f i_q + \omega L_f i_q + v_{oq} &= \frac{V_{DC}}{2} m_q \end{aligned} \tag{4.11}$$

where V_{DC} is the DC input voltage of VSC, and m_d and m_q are modulation indexes.

While droop control governs steady-state power sharing, its effectiveness depends on the dynamic behavior of the lower-level voltage and current control loops. To ensure fast and stable tracking of the voltage and current references generated by the droop mechanism, proper design of these lower control loops is essential.

To this end, this study investigates two distinct approaches aimed at improving the dynamic response of the control system: a virtual complex impedance-based method and a computationally enhanced, simulation-based optimization framework.

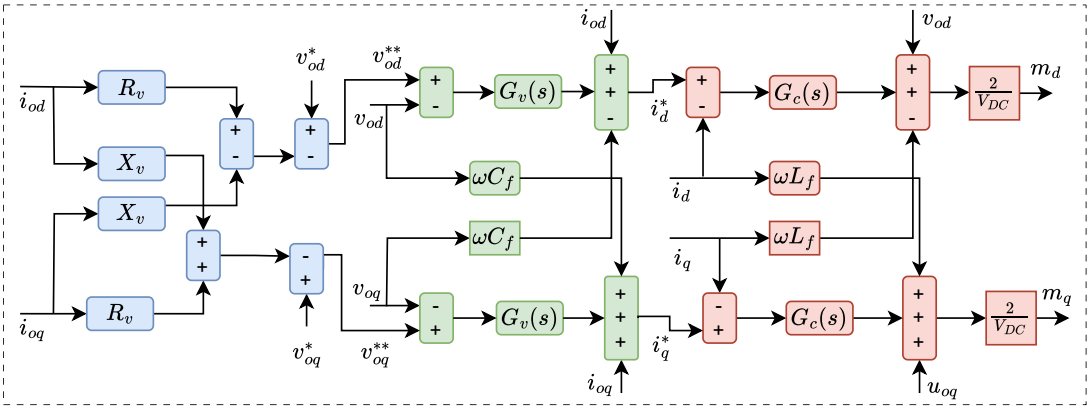

Fig. 4.6: Schematic of the lower-level control loops with virtual complex impedance augmentation.

4.3 Virtual Complex Impedance-Based Control

In modern MG, especially under islanded operation, ensuring stable and efficient power sharing among parallel converters presents a significant challenge. Variations in line impedance can lead to unequal power distribution, voltage deviations, and instability. Conventional control strategies often fall short under such impedance mismatches. To address this, virtual impedance is commonly introduced by emulating additional impedance within the converter's control loop. This approach is intended to mitigate the impact of line impedance mismatch, promote more balanced power sharing, support voltage regulation, and contribute to improved system reliability.

Resistive and inductive virtual impedances are commonly employed to improve power sharing and system stability. However, since distribution lines inherently exhibit both resistive and inductive characteristics, relying solely on either type can be problematic. Resistive virtual impedance may lead to increased voltage drops and reduced power output, while inductive virtual impedance can introduce reactive power sharing errors and compromise dynamic performance. These limitations highlight the need for more advanced virtual impedance strategies capable of handling the complex impedance profiles typical in practical microgrids.

Virtual complex impedance, which combines resistive and inductive components, has been widely explored to address the limitations of purely resistive or inductive methods. This approach is especially suited for microgrids, where the output impedance naturally exhibits both resistive and inductive characteristics [88]. By avoiding reliance on detailed knowledge of the network and load conditions, it provides a more flexible and adaptive control solution. In this research, a virtual complex impedance loop is integrated into the feedback path of the voltage control loop, as shown in Fig. 4.6, to improve power sharing accuracy and ensure stable operation among parallel-connected inverters. In this way, the inverter output voltage is

controlled by adjusting the virtual impedance Z_v.The virtual complex impedance is expressed using resistive (R_v) and inductive (L_v) components as follows:

$$Z_v = R_v + jX_v \tag{4.12}$$

As depicted in Fig.4.6, the modified voltage reference v_{od}^{**} is obtained as:

$$\begin{aligned} v_{od}^{**} &= v_{od}^{*} - (i_{od}R_v - i_{oq}X_v) \\ v_{oq}^{**} &= v_{oq}^{*} - (i_{oq}R_v + i_{od}X_v) \end{aligned} \tag{4.13}$$

The virtual impedance modifies the power converter output voltage reference as indicated in Eq. (4.13), where the modified voltage reference v_{od}^{**} and v_{oq}^{**} are obtained by subtracting the virtual voltage drop across the virtual impedance Z_v from the reference value originally provided by the droop equations, v_{od}^{*} and v_{oq}^{*} .

To determine the value of R_v and L_v, the dominant inductive behavior of the output impedance is guaranteed with $\theta > 65^0$ [102]. Taking this into consideration, the design equation can be expressed as:

$$tan\theta = \frac{\omega_0(L_v + L_c)}{R_v + R_c} > 2.14 \tag{4.14}$$

where R_c and L_c are the resistive and inductive components of the output impedance of the system.

4.4 VSC Parameterization for Computational Optimization-Based Control

4.4.1 Current Controller Design

The cross-coupling in Eq. (4.11) due to the presence of ωL_f terms should be decoupled to control i_d and i_q separately. The decoupling can be obtained by using the feedforward compensation technique as follows [95], [103]:

$$\begin{aligned} m_d &= \frac{2}{V_{DC}}(u_d - L_f\omega i_q + v_{od}) \\ m_q &= \frac{2}{V_{DC}}(u_q + L_f\omega i_d + v_{oq}) \end{aligned} \tag{4.15}$$

where u_d and u_q are control variables produced by the current controller $G_c(s)$, as shown in Fig. 4.7. The decoupling process is carried out by substituting the expressions for m_d and m_q

from Eq. (4.15) into Eq. (4.11), followed by algebraic rearrangement, resulting in:

$$L_f \frac{di_d}{dt} + R_f i_d = u_d; \qquad L_f \frac{di_q}{dt} + R_f i_q = u_q \tag{4.16}$$

The error signals e_{cd} and e_{cq} input to the compensator $G_c(s)$ are given by:

$$e_{cd} = i_d^\star - i_d; \qquad e_{cq} = i_q^\star - i_q \tag{4.17}$$

where $i_d^\star$ and $i_q^\star$ are reference currents generated by the voltage control loop shown in Fig. 4.7a. Based on Eqs. (4.16) and (4.17), one can sketch the simplified control block diagram of the current control loop as shown in Fig. 4.7b. Thus, the open loop gain is given as:

$$l(s) = \left(\frac{k_{pc}}{L_f s}\right)\left(\frac{s + k_{ic}/k_{pc}}{s + R_f/L_f}\right) \tag{4.18}$$

where $G_c(s)$ is PI compensator. The open-loop transfer function $l(s)$ has a stable pole at $s = -R_f/L_f$. To enhance the frequency response, this pole can be canceled by the PI compensator zero [95], [104], [105]. By selecting $k_{ic}/k_{pc} = R_f/L_f$ and $k_{pc}/L_f = 1/\tau_i$, where τ_i is the desired time constant of the closed-loop current controller, the resulting closed-loop transfer function becomes:

$$i_{dq}(s) = G_i(s) i_{dq}^*(s) = \frac{1}{\tau_i s + 1} i_{dq}^*(s) \tag{4.19}$$

where $G_i(s)$ is the closed-loop transfer function of the current control loop. The time constant τ_i is chosen to be 4 to 10 times the switching time constant of the VSC [95], [104]. The upper boundaries of the PI parameters are selected as:

$$k_{\mathrm{pc}}^{max} = \frac{L_{fmax}}{\tau_i}; \qquad k_{ic}^{max} = \frac{R_{fmax}}{\tau_i} \tag{4.20}$$

Then, the PI controller parameters, k_{pc} and k_{ic}, are determined through computational optimization techniques to ensure effective current control performance.

4.4.2 Voltage Controller Design

Since the voltage equations also exhibit cross-coupling between the d- and q-axes, a feedforward decoupling strategy—similar to that employed in the current control loop—is introduced to mitigate the interaction between v_{od} and v_{oq}. As indicated in Eq. (4.10), effective voltage regulation is achieved by adjusting the converter-side current i_{dq}. This is necessary because the output current i_{odq} is not directly controllable, being affected by external factors such as load variations and network dynamics. Therefore, the voltage control loop generates the reference current i_{dq}^* based on the desired voltage profile and system behavior, which is

defined as follows:

$$
\begin{aligned}
i_d^* &= v_d + i_{od} - \omega C_f v_{oq} \\
i_q^* &= v_q + i_{oq} + \omega C_f v_{od}
\end{aligned} \tag{4.21}
$$

where v_d and v_q are control input variables [104]. Substituting for i_d^* and i_q^*, from Eq. (5.4) into Eq. (4.19) one obtains:

$$
\begin{aligned}
i_d(s) &= G_i(s)u_d(s) - (C_f\omega_0)G_i(s)v_{oq}(s) + G_i(s)i_{od}(s) \\
i_q(s) &= G_i(s)u_q(s) - (C_f\omega_0)G_i(s)v_{od}(s) + G_i(s)i_{oq}(s)
\end{aligned} \tag{4.22}
$$

Taking Laplace transform from both sides of Eq. (4.10), and substituting for i_d(s) and i_q(s) from Eq. (4.22) in the resultants, one has:

$$
\begin{aligned}
\frac{\tau_d s+1}{R_d} s v_{od}(s) &= G_i(s)u_d(s) + \frac{\tau_i s}{\tau_i s+1} C_f\omega_0 v_{oq}(s) - \frac{\tau_i s}{\tau_i s+1} i_{od}(s) \\
\frac{\tau_d s+1}{R_d} s v_{oq}(s) &= G_i(s)u_d(s) + \frac{\tau_i s}{\tau_i s+1} C_f\omega_0 v_{od}(s) - \frac{\tau_i s}{\tau_i s+1} i_{oq}(s)
\end{aligned} \tag{4.23}
$$

where $\tau_d = R_d C_f$ is the time constant of parallel R_d and C_f. The term $\tau_i s/(\tau_i s+1)$ has a zero DC gain which can rapidly decay to zero in steady state by selecting a small value of τ_i [104]. Hence, Eq. (4.23) can be approximated as:

$$
\begin{aligned}
\frac{v_{od}(s)}{u_d(s)} &\approx G_i(s)\frac{R_d}{\tau_d s+1} = \frac{R_d}{(\tau_i s+1)(\tau_d s+1)} \\
\frac{v_{oq}(s)}{u_q(s)} &\approx G_i(s)\frac{R_d}{\tau_d s+1} = \frac{R_d}{(\tau_i s+1)(\tau_d s+1)}
\end{aligned} \tag{4.24}
$$

Based Eq. (4.24), the control signals v_d and v_q which are the outputs of the voltage compensator $G_v(s)$ can independently control v_{od} and v_{oq}, respectively. The error signals e_{vd} and e_{vq} input to the compensator $G_v(s)$ are given by:

$$
e_{vd} = v_{od}^\star - v_{od}; \qquad e_{vq} = v_{oq}^\star - v_{oq} \tag{4.25}
$$

Equation (4.24) describes a type zero system, which inherently results in steady-state error under a step input. To ensure fast regulation and eliminate this error, a PI compensator is employed. The corresponding simplified closed-loop system from Eq. (4.22) is illustrated in Fig. 4.7b, where $G_v(s)$ denotes the PI controller. The selection of k_{pv} and k_{iv} gains is guided by the open-loop gain, as provided below:

$$
l(s) = \frac{R_d}{s(\tau_d s+1)}\left(K_{iv}\frac{\tau_v s+1}{\tau_i s+1}\right) \tag{4.26}
$$

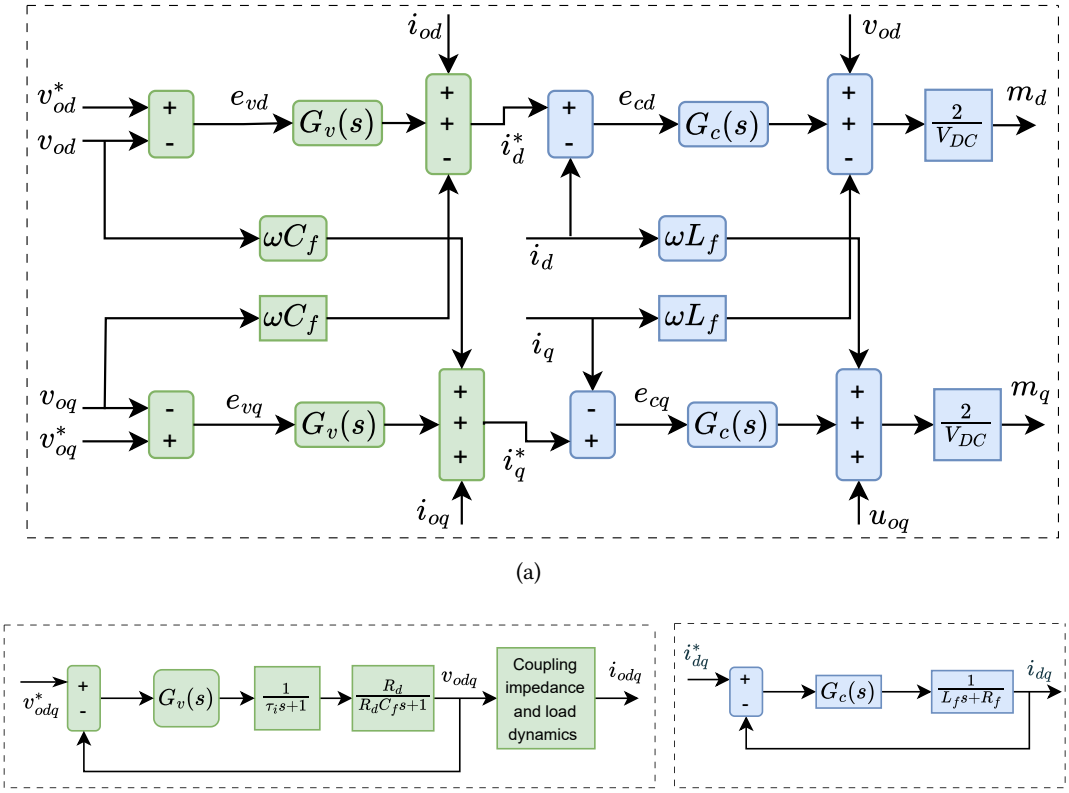

Fig. 4.7: (a) VSC voltage and current control loops. (b) Simplified VSC voltage and current control loops.

where $\tau_v = k_{pv}/k_{iv}$ is the voltage compensator time constant. In Eq. (4.26), if we design such that $\tau_i \ll \tau_v$ since the time response of the current control loop is faster than that of the voltage control loop, the term in the bracket

$$G(s) = K_{iv}\frac{\tau_v s + 1}{\tau_i s + 1}$$

has the maximum phase ϕ_m at ω_m with positive gain G_m. To ensure stability against variations in system parameters, it is essential to choose appropriate values for ϕ_m and G_m. When ϕ_m is large, the system responds sluggishly to disturbances but remains robust against changes in parameters. Smaller ϕ_m values result in faster responses, but may result in oscillations or instability. For satisfactory performance, ϕ_m should be between 30° and 75°, and the G_m should be greater than 6 dB [103], [106]. After selecting the proper value of ϕ_m, the voltage controller bandwidth $\omega_v = \frac{1}{\tau_v}$ is determined as:

$$\omega_v = \omega_i\left(\frac{1 - sin\phi_m}{1 + sin\phi_m}\right) \tag{4.27}$$

where $\omega_i = \frac{1}{\tau_i}$ is bandwidth of the closed-loop system of Eq. (4.19). Then, the frequency ω_m at which the maximum phase ϕ_m is achieved can be obtained as:

$$\left.\frac{d\angle G(j\omega)}{d\omega}\right|_{\omega=\omega_m} = 0$$

resulting to

$$\omega_m = \sqrt{\omega_i \omega_v} \tag{4.28}$$

If the gain crossover frequency ω_{gc} of Eq. (4.26) is chosen as ω_m, then ϕ_m becomes the phase margin. For this to hold, the PI gains k_{pv} and k_{iv}, must satisfy the condition $|l(j\omega_{gc})|$ = $|l(j\omega_m)|$ = 1, which yields to:

$$k_{iv} = \frac{1}{Rd}\left|\frac{1}{L(j\omega_m)}\right|; \qquad k_{pv} = \tau_v k_{iv} \tag{4.29}$$

where $L(s) = (\tau_v s+1)/(s(\tau_d s+1)(\tau_i s+1))$. The open-loop transfer function $l(s)$ described by Eq. (4.26) is a *type one system*. In such systems, the response of a feedback control system to a ramp input exhibits a steady-state error. Setting the integral gain k_{iv} to a sufficiently large value is crucial to keeping the steady-state response within an acceptable range. In this research, the optimal values of k_{iv} and k_{pv} are determined using computational optimization methods, and their upper bounds are defined as:

$$k_{iv}^{max} = \frac{1}{R_d}\left|\frac{1}{L(j\omega_m)}\right|; \qquad k_{pv}^{max} = \tau_v k_{iv}^{max} \tag{4.30}$$

4.4.3 LCL Filter Design Considerations

A well-designed LCL filter exhibits a minimum component size while meeting standards like IEEE-519 for sufficient harmonic attenuation [107]. To achieve this, understanding the relationship between filter parameters and various design requirements is crucial. By setting $L_T = L_f + L_c$, $\mu = L_c/L_f$ and $\lambda = \omega_{sw}/\omega_{res}$, Eq. (4.3) can be modified to:

$$L_T C_f = \frac{\lambda^2}{\omega_{sw}^2}\frac{(1+\mu)^2}{\mu} \tag{4.31}$$

where ω_{sw} is the switching frequency of the VSC in rad/s.

Eq. (4.31) can be expressed per unit to generalize the design for a wide range of power levels. By selecting the following base values: $P_b = P_n$, with P_n is the rated power of VSC, $V_b = V_{LL}$, with V_{LL} is the line to line output nominal voltage, $\omega_b = 2\pi f_0$, with f_0 is the nominal frequency in Hz, $Z_b = V_b^2/P_b$, $C_b = 1/(Z_b\omega_b)$ and $L_b = Z_b/\omega_b$, the per unit expression of

Eq. (4.31) can be derived as:

$$l_T c_f = \frac{\lambda^2}{\rho^2} \frac{(1+\mu)^2}{\mu} \tag{4.32}$$

where l_T is the per unit total inductance, $l_T = L_T/L_b$, c_f is the per unit capacitance, $c_f = C_f/C_b$, $\rho = \omega_{sw}/\omega_b$. Eq. (4.32) shows that the product of passive components l_T and c_f depends on the ratios λ and μ. In designing an LCL filter, the goal is to minimize component size while ensuring compliance with IEEE-519 harmonic limits [107] and reactive power compensation constraints [89], [90]. The ratio μ governs both the total inductance l_T and the filter's attenuation. The product $c_f l_T$ reaches its minimum when $\mu = 1$, found by setting the derivative of Eq. (4.32) with respect to μ to zero.

Rearranging Eq. (4.32), the ratio λ can be expressed as:

$$\lambda = \rho \frac{\sqrt{\mu}}{1+\mu} \sqrt{l_T c_f} \tag{4.33}$$

The maximum value of λ, corresponding to the minimum ω_{res}, is obtained by solving the equation $\frac{d\lambda}{d\mu} = 0$ as per Eq. (4.33). However, choosing an appropriate value for λ is essential to ensure that the resonance frequency falls within an acceptable range. In this research, the authors uniquely determine the suitable value of λ. From Eqs. (4.1) and (4.2), the ratio of the magnitude of the output current ripple Δi_o with converter-side current ripple Δi at the switching frequency is given as:

$$\frac{\Delta i_o(h_{sw})}{\Delta i(h_{sw})} = \frac{z_{LC}^2}{s^2 + z_{LC}^2} \tag{4.34}$$

where $z_{LC}^2 = \frac{1}{L_c C_f}$. The per-unit representation of Eq. (4.34) at switching frequency (i.e., $h_{s\omega} = j\omega_{sw}$) is given as:

$$\left| \frac{\Delta i_{opu}(h_{sw})}{\Delta i_{pu}(h_{sw})} \right| = \frac{1}{|1 - (1+\mu)\lambda^2|} = \sigma \tag{4.35}$$

Then rearranging Eq. (4.35), we have:

$$(1+\mu)\lambda^2 + \frac{1}{\sigma} - 1 = 0$$

which is a quadratic equation, and solving for λ will result in two values, where the negative value can be ignored as the magnitude is of interest. Hence, the positive value of λ as a

function of μ and attenuation factor σ is given as:

$$\lambda = \sqrt{\frac{1}{1+\mu}\left|1 - \frac{1}{\sigma}\right|} \tag{4.36}$$

The selection of λ based on Eq. (4.36) ensures that the output current i_o complies with the IEEE-519 standard [90], [107]. According to this standard, the magnitude of odd harmonic components in i_o (of order greater than or equal to 35) should not exceed 0.3% of the converter-rated output current I_o in RMS [108]. Meanwhile, the converter-side ripple current varies between 5% and 25% of I_o [109]–[111].

For a specific case where μ=1 and $\Delta i_{opu}(h_{sw})$ = 0.2%, the value of λ ranges from 3.0822 to 7.0356 as $\Delta i_{pu}(h_{sw})$ varies from 5% to 25%. It's important to note that choosing a small value for $\Delta i_{pu}(h_{sw})$ results in a higher requirement for converter side inductance L_f, while opting for a large value of $\Delta i_{pu}(h_{sw})$ may lead to a small L_f. As a common practice, $\Delta i_{pu}(h_{sw})$ is recommended to be set at 10% [109]–[112], which the authors have adopted in this work.

4.4.4 Total Inductance Design

The total inductance is selected such that the filter has the highest efficiency and complies with the IEEE-519 standard for harmonic limitation [107]. Based on Eqs. (4.1) and (4.3), we have:

$$\frac{i_o(s)}{v_t(s)} = \frac{1}{L_T s}\left(\frac{\omega_{res}^2}{s^2 + \omega_{res}^2}\right) \tag{4.37}$$

The ripple attenuation, passing from the converter side to the load side at the switching frequency can be determined as:

$$\left|\frac{\Delta i_o(h_{sw})}{\Delta v_t(h_{sw})}\right| = \frac{1}{L_T \omega_{sw}|1-\lambda^2|} \tag{4.38}$$

Per unit representation of Eq. (4.38) can be expressed as:

$$\left|\frac{\Delta i_{opu}(h_{sw})}{\Delta v_{tpu}(h_{sw})}\right| = \frac{1}{l_T \rho|1-\lambda^2|} \tag{4.39}$$

Eq. (4.39) is modified to determine the minimum per unit total inductance as expressed in:

$$l_{Tmin} = \frac{|\Delta v_{tpu}(h_{sw})|}{\rho|\Delta i_{opu}(h_{sw})||1-\lambda^2|} \tag{4.40}$$

Here, the voltage switching ripple component $\Delta v_{tpu}(h_{sw})$ at the converter terminal can be evaluated using methods outlined in references [90]–[93].

The choice of l_{Tmin} based on Eq. (4.40) is reasonable in terms of filter losses and size. However, it may not necessarily meet the harmonic attenuation criterion defined in the IEEE-519 standard [107]. Consequently, l_{Tmin} serves as a lower limit for optimizing the total inductance.

The maximum per unit total inductance (l_{Tmax}) in a filter connected to a VSC depends on the availability of the DC bus. Factors such as the AC voltage drop across the total inductance during inverter operation and anticipated switching losses influence this limit. Minimizing l_T helps reduce the DC bus requirement, as higher DC bus values lead to increased switching losses. Typically, l_{Tmax} is limited to 0.1 per unit [89], [90]. Hence, the range of l_T is given as:

$$l_{Tmin} \leq l_T \leq l_{Tmax} \tag{4.41}$$

As observed from the inequality in Eq. (4.41), multiple solutions fall within this range for the selected values of μ and λ. The proposed approach determines the optimal value of l_T within this range through computational optimization methods.

4.4.5 Filter Capacitor Design

A filter capacitor C_f is used to suppress switching frequency harmonics in the output voltage. It provides a low-impedance path for the switching current harmonics produced by the VSC, thereby isolating the load from their effects. The effective power delivered by the VSC in Fig. 4.2 is given by:

$$S = P - j(Q_{L_T} - Q_{C_f}) \tag{4.42}$$

When the capacitor C_f operates at the system's full voltage, the inductors L_f and L_c are effectively in series and assumed to carry full-rated currents. Consequently, Eq. (4.42) transforms into:

$$S \approx P - j(\omega_o L_T I_o^2 - \omega_o C_f V_o^2) \tag{4.43}$$

where I_o denotes the system's fundamental rated current. The per unit representation of Eq. (4.43) becomes:

$$s \approx p - j(l_T - c_f) \tag{4.44}$$

From Eq. (4.44), we deduce that the net per unit reactive power output is given by:

$$q \approx c_f - l_T \tag{4.45}$$

For a VSC transferring unity active power, that is $P = P_b$, the per unit real component is unity (p = 1), and Eq. (4.44) simplifies to:

$$s \approx 1 - j(l_T - c_f) \tag{4.46}$$

Consequently, the power factor (PF) of the VSC output is:

$$PF = \frac{1}{\sqrt{1 + q^2}} \tag{4.47}$$

Maintaining a near-unity PF is generally recommended in grid-connected systems [89], [90]. However, in islanded operation, VSCs must supply reactive power, which conflicts with strict unity PF requirements. The key challenge is to determine the minimum reactive power needed based on the nature of the connected load (inductive or capacitive).

As shown in Eqs. (4.46) and (4.47), reactive power increases the VSC's apparent power rating. To avoid this, a high operating PF is preferred. The minimum reactive power is constrained by the VSC's maximum allowable PF, expressed as:

$$q_{min} = \sqrt{\frac{1}{PF_{max}^2} - 1} \tag{4.48}$$

Accordingly, using Eqs. (4.45) and (4.48), the minimum per-unit filter capacitor value to limit reactive power is given as:

$$c_{fmin} = l_{Tmin} - q_{min} \tag{4.49}$$

The per-unit maximum capacitance, c_{fmax}, is selected to limit the reactive power drawn by the shunt branch, defined as a maximum $\kappa\%$ of the base capacitance C_b, i.e., $c_{fmax} = C_{fmax}/(\kappa C_b)$. The optimal value of c_f is searched within the range:

$$c_{fmin} \leq c_f \leq c_{fmax} \tag{4.50}$$

Since multiple c_f values satisfy Eq. (4.50), the proposed approach determines the optimal one through computational optimization to achieve the best system performance.

4.4.6 Damping Resistor Design

In power electronic systems, the LCL filter plays an important role in reducing unwanted harmonics. However, its performance depends on adequate damping. Insufficient damping can cause resonance, resulting in amplified ripple [89], [113]. To address this, a parallel passive damping method is used, where a resistor is placed in parallel with the filter capacitor

(see Section 4.2). This approach is favored for its simplicity, reliability, and minimal impact on the control structure. The key challenge is selecting an appropriate value for the damping resistor, R_d. The proposed method aims to suppress oscillations while maintaining system efficiency. Specifically, the damping resistor R_d should be selected such that it is larger than the impedance of the filter capacitor X_{C_f} at the fundamental frequency ω_0—that is, $X_{C_f}|_{\omega=\omega_0} < R_d$. To express this relationship, let α represent the ratio of the filter capacitor's impedance at the fundamental frequency to the damping resistor, defined as:

$$\alpha = \frac{X_{C_f}}{R_d}; \qquad X_{C_f} = \frac{1}{\omega_0 C_f}$$

the currents conducted by R_d at the fundamental frequency ω_0 is given as:

$$I_{R_d} = \frac{X_{C_f}}{X_{C_f} + R_d} I_{sh} = \frac{\alpha}{\alpha + 1} I_{sh} \tag{4.51}$$

where I_{sh} is current through shunt impedance at the fundamental frequency and α is between zero and one. Passive damping design ensures that damping losses do not exceed acceptable thresholds (not greater than 1% of the nominal power) to avoid efficiency reduction. The condition for damping efficiency is succinctly captured as $I_{sh} < 1\% I_o$, where I_o denotes the system's fundamental current [113]. This corresponds to:

$$I_{R_d} < \frac{\alpha}{\alpha + 1} 1\% I_o; \qquad P_d < \frac{\alpha}{\alpha + 1} 1\% P_n \tag{4.52}$$

where P_d is total damping loss and P_n is system nominal rated power. Then, the corresponding minimum damping resistor can be determined as:

$$R_{dmin} = \frac{\alpha + 1}{\alpha} \frac{V_o^2}{1\% P_n}\bigg|_{\alpha=1}; \qquad 0 < \alpha \leq 1 \tag{4.53}$$

As observed from Eqn. (4.51), when $\alpha = 0$, the system corresponds to an undamped case, representing the theoretical extreme where $R_d \to \infty$. This condition is not used for practical design but helps illustrate the upper extent of the damping resistor. One can select a practical $R_{d_{\max}}$ based on methods such as frequency-domain criteria, impedance-based analysis, or control-oriented constraints. Additionally, the damping factor ζ, when constrained within a practical range (e.g., $\zeta_{\min} = 0.1$ to $\zeta_{\max} = 0.7$), can be employed to define the permissible upper limit of R_d, helping designers avoid underdamped or overdamped behavior while limiting energy dissipation in the damping resistor. This method offers a systematic way to estimate $R_{d_{\max}}$, ensuring acceptable dynamic performance. Based on the selected method, an

admissible range for the damping resistor is defined as:

$$R_{d_{\min}} \leq R_d \leq R_{d_{\max}}$$

Within this interval, several values of R_d may satisfy the damping requirements. A computational optimization approach can be utilized to determine the most suitable value of R_d, ensuring an effective trade-off between damping performance and broader system-level objectives such as harmonic suppression and energy efficiency.

4.5 Computational Intelligence-Based Optimization Approach

4.5.1 Formulation of Objective Function

In the context of computational intelligence-based optimization, the formulation of a well-defined objective function is central to guiding the search process toward optimal system performance. The objective function is defined for parameter optimization based on the desired specifications and constraints. This function can be selected using specific points of the time response or the entire time response, often employing integral criteria as performance indices [114]. Common indices include the Integral of Squared Error (ISE), Integral of Absolute Error (IAE), Integral of Time multiplied by Squared Error (ITSE), and Integral of Time multiplied by Absolute Error (ITAE) [114], [115]. Among these indices, the ITAE-based objective function has been reported to significantly improve system performance compared to the others, as noted in [115]–[117].

Instead of conventional trial-and-error methods, this study employs an optimization approach to enhance the efficiency and performance of VSC systems by systematically tuning critical design parameters. Specifically, the following parameters are optimized: the filter's damping resistance R_d, converter-side inductance L_f, shunt capacitance C_f, and coupling inductance L_c, as well as the voltage and current controller gains $(K_{pv}, K_{iv}, K_{pc}, K_{ic})$.

To effectively guide the optimization process, this study adopts an objective (or fitness) function based on the ITAE, which is widely recognized for its ability to penalize sustained errors and improve system transient performance [114]–[117]. In addition to capturing the dynamic behavior through the tracking error, this formulation integrates a power quality component by incorporating the Total Harmonic Distortion (THD) of the output voltage. This dual-focus objective ensures that both dynamic response and harmonic performance are simultaneously considered.

Accordingly, the objective function $J(x)$ is expressed as:

$$J(x) = \int_{t=0}^{t_f} t|e(t)|\,dt + \int_{t=0}^{t_f} t \cdot \text{THD}_v(t)\,dt \tag{4.54}$$

where t_f denotes the total simulation time, $e(t)$ represents the instantaneous deviation between the reference and actual output signals, as obtained from Eqs. (4.17) and (4.25), and $\text{THD}_v(t)$ is the time-varying total harmonic distortion of the output voltage, evaluated via Fast Fourier Transform (FFT) analysis.

The THD of the voltage waveform is calculated as:

$$\text{THD}_v = \frac{\sqrt{\sum_{n=2}^{\infty} V_n^2}}{V_1} \times 100\% \tag{4.55}$$

where V_1 denotes the RMS value of the fundamental frequency component, and V_n is the RMS value of the n^{th} harmonic component.

This optimization task is framed as a constrained problem, where the goal is to minimize the objective function $J(x)$ subject to physical and design-based parameter limits. The general formulation is given as:

$$\begin{aligned} &\text{Minimize } J(x) \quad \text{subject to:} \\ &x_j^{\min} \leq x_j \leq x_j^{\max} \end{aligned}$$

where x_j denotes the j^{th} design variable, and $x_j^{\min}$, $x_j^{\max}$ represent its lower and upper bounds, respectively.

In the context of this study, the decision variables encompass both filter component values and controller gains. The optimization bounds are defined as follows:

$$\begin{aligned} k_{pc}^{\min} \leq k_{pc} \leq k_{pc}^{\max}; \qquad & k_{ic}^{\min} \leq k_{ic} \leq k_{ic}^{\max}; \\ k_{pv}^{\min} \leq k_{pv} \leq k_{pv}^{\max}; \qquad & k_{iv}^{\min} \leq k_{iv} \leq k_{iv}^{\max}; \\ L_f^{\min} \leq L_f \leq L_f^{\max}; \qquad & L_c^{\min} \leq L_c \leq L_c^{\max}; \\ C_f^{\min} \leq C_f \leq C_f^{\max}; \qquad & R_d^{\min} \leq R_d \leq R_d^{\max} \end{aligned}$$

These bounds are determined based on practical design guidelines, component limitations, and control performance requirements. Constraining the search space in this manner helps ensure feasible and implementable solutions while reducing computational complexity during the optimization process.

4.5.2 Metaheuristic Optimization Techniques

Computational intelligence techniques like GA and PSO are popular for overcoming traditional optimization limitations. Other metaheuristic approaches, such as Harris Hawks Optimization (HHO), Grey Wolf Optimization (GWO), Cuckoo Search (CS), Butterfly Optimization Algorithm (BOA), Grasshopper Optimization Algorithm (GOA), and Ant Colony Optimization (ACO), are also widely used for complex, nonlinear, and high-dimensional problems [118]. These nature-inspired algorithms are particularly useful in engineering applications where conventional techniques struggle with computational efficiency and adaptability [119].

Despite their advantages, each metaheuristic algorithm has inherent limitations affecting practical applicability. For example, HHO excels in exploration but has a slow convergence rate and can get trapped in local optima. This makes it less effective in dynamic optimization tasks [120], [121]. Similarly, BOA, while handling nonlinear problems well, is prone to instability and premature convergence, which can compromise long-term optimization stability [122], [123].

GOA is effective in avoiding local optima but requires careful parameter tuning to maintain consistent performance across different problem domains. This tuning process can be time-consuming and complex [124]. GWO, known for preventing early stagnation, gradually loses population diversity over time, increasing the likelihood of premature convergence and reducing its effectiveness in later iterations. [125], [126].

GA remains a popular choice for discrete optimization due to its robustness in combinatorial problems. However, its slow convergence and high computational costs, along with sensitivity to mutation and crossover parameters, often hinder its efficiency in continuous optimization tasks [127], [128]. ACO, effective for discrete search spaces, struggles with slower convergence in continuous problems due to its dependency on pheromone-based learning, which requires careful tuning to prevent stagnation [129], [130]. Likewise, CS can escape local optima through its random walk mechanism, but this characteristic also makes its convergence behavior unpredictable, leading to reduced stability in optimization performance [131].

While each of these algorithms offers strengths tailored to specific optimization scenarios, they also present inherent trade-offs between solution accuracy, convergence speed, and computational complexity. For microgrid control applications, where real-time responsiveness and adaptability are critical, an algorithm that provides robust performance with manageable computational demands is essential. PSO has gained attention for its relatively simple structure and ability to provide acceptable solutions within a reasonable time frame [132], [133]. Its population-based update mechanism, inspired by swarm intelligence, facilitates efficient search and adjustment in dynamic environments. Although PSO may exhibit limitations in

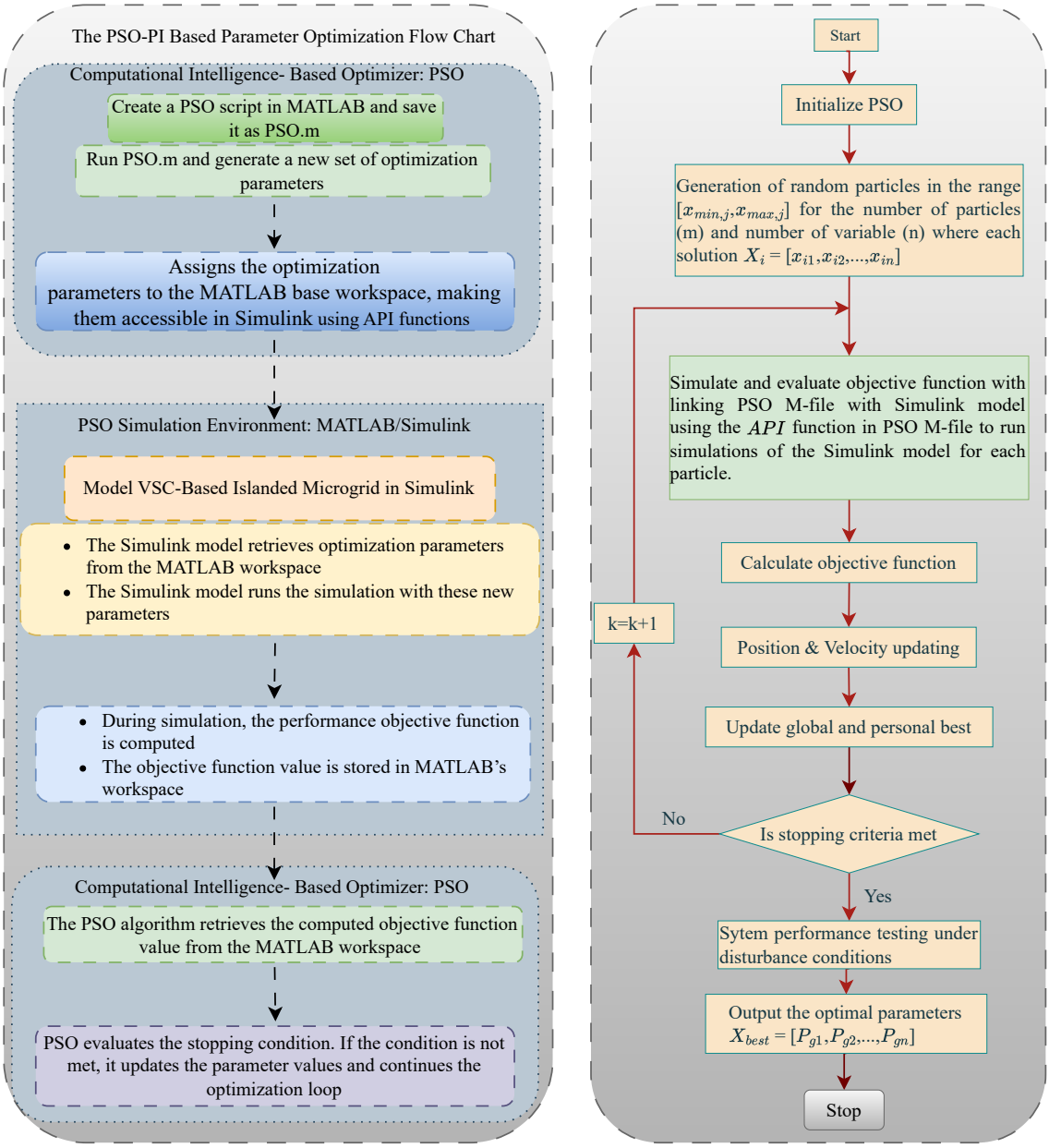

Fig. 4.8: Simulation-based online parameter optimization of an islanded VSC integrating PSO within a SIMULINK framework.

global exploration compared to more complex metaheuristics, its ease of implementation, low tuning effort, and satisfactory convergence behavior make it a practical choice for real-time optimization tasks such as control parameter tuning in islanded MGs [132], [134]. Accordingly, this study adopts PSO as a suitable candidate for the proposed simulation-based optimization framework.

PSO, a computational intelligence-based technique, is highly effective for solving large-scale

and nonlinear optimization problems [135], [136]. Fig. 4.8 illustrates the design flowchart for simulation-based online parameter optimization of an islanded VSC system, where PSO is integrated within a SIMULINK framework to iteratively refine control parameters. In this approach, the filter and controller parameters are directly defined within the SIMULINK model, allowing seamless interaction with the system's dynamic behavior. The objective function is embedded within the same model, serving as a performance metric to guide the optimization process. The PSO algorithm is implemented as a MATLAB script (M-file) and integrated with the SIMULINK model through MATLAB API functions. This setup enables continuous parameter adjustments and real-time optimization throughout the simulation.

In this framework, PSO employs a group of particles—each representing a candidate solution—that iteratively adjusts their positions using both personal and collective experience to converge toward an optimal solution [136]. Mathematically, each particle is described by its position and velocity vectors within the search space, defined as:

$$[X_i] = [x_{i1}, x_{i2}, ..., x_{ij}, ..., x_{in}] \tag{4.56}$$

where $i = 1, 2, ..., m$ are the number of particles and $j = 1, 2, ..., n$ are the dimensions of each particle. In an n-dimensional search space, the velocity vector $[V_i^k]$ and position vector $[X_i^k]$ of i^{th} particle at k^{th} iteration are represented by:

$$\begin{aligned} [V_i^k] &= [v_{i1}^k, v_{i2}^k, ..., v_{ij}^k, ..., v_{in}^k] \\ [X_i^k] &= [x_{i1}^k, x_{i2}^k, ..., x_{ij}^k, ..., x_{in}^k] \end{aligned} \tag{4.57}$$

Each particle is initialized with a random position within the search bounds $[x_{min,j}, x_{max,j}]$ and a velocity within $[v_{min,j}, v_{max,j}]$. It stores its personal best position $[P_{bi}^k]$ and accesses the global best position $[P_g^k]$ found by the swarm. The optimization proceeds iteratively, updating velocities and positions using the following recursive equations:

$$\begin{aligned} v_{ij}^{k+1} &= \chi . \left(v_{ij}^k + \varphi_1 r_1 (P_{b,ij}^k - x_{ij}^k) + \varphi_2 r_2 (P_{g,j}^k - x_{ij}^k) \right) \\ x_{ij}^{k+1} &= x_{ij}^k + v_{ij}^{k+1} \end{aligned} \tag{4.58}$$

where

$$\chi = \frac{2}{|2 - \varphi - \sqrt{\varphi^2 - 4\varphi}|}, \varphi_1 + \varphi_2 = \varphi > 4$$

with χ as the constriction factor, and φ_1 and φ_2 are acceleration constants.

4.6 Results and Discussion

The performance of two distinct approaches—a virtual complex impedance-based control method and a PSO-based simulation framework—was evaluated using MATLAB/Simulink simulations. The key system specifications and VSC parameters are listed in Table 4.1. Each method was tested under various disturbance scenarios to assess its effectiveness. In the simulated setup, multiple VSC operated in parallel, sharing a common load at the point of common coupling (PCC).

4.6.1 Evaluation of Virtual Complex Impedance-Based Control

This section investigates the performance of a cascaded virtual complex impedance-based control strategy designed to ensure proper active and reactive power sharing among parallel VSCs in an islanded microgrid. The control approach incorporates both virtual resistance and inductance, synthesized using an impedance angle of 65.5° to shape the output impedance of

Table 4.1: Table of Key System Specifications and VSC Parameters.

Parameters	Value	Parameters	Value
P_n	1.25 MW	f_{sw}	15 kHz
V_{DC}	800 V	ω_f	$0.1\omega_o$ rad/s
V_o	311 V	m_p	$2.5133\mathrm{e}^{-7}$ W/s
f_o	50 Hz	n_q	$1.2445\mathrm{e}^{-4}$ V/VAR
ω_o	$2\pi f_o$ rad/s	K_e	100

Table 4.2: VSC Parameters for Virtual Complex Impedance-Based Control.

Parameters	Value	Parameters	Value
L_f	15 μH	τ_i	$4.244\mathrm{e}^{-5}$ s
L_c	0.5 μH	τ_v	$3.800\mathrm{e}^{-4}$ s
C_f	1400 μF	ϕ_m	53°
R_f	1 mΩ	θ	65.5°
R_c	0.1 mΩ	k_{pc}	0.391
R_d	1 $k\Omega$	k_{ic}	$2.356\mathrm{e}^{3}$
L_v	0.5 μH	k_{pv}	10.802
R_v	0.5 mΩ	k_{iv}	$2.850\mathrm{e}^{4}$

each converter. The aim is to emulate a desirable droop response that facilitates decentralized power sharing without the need for communication.

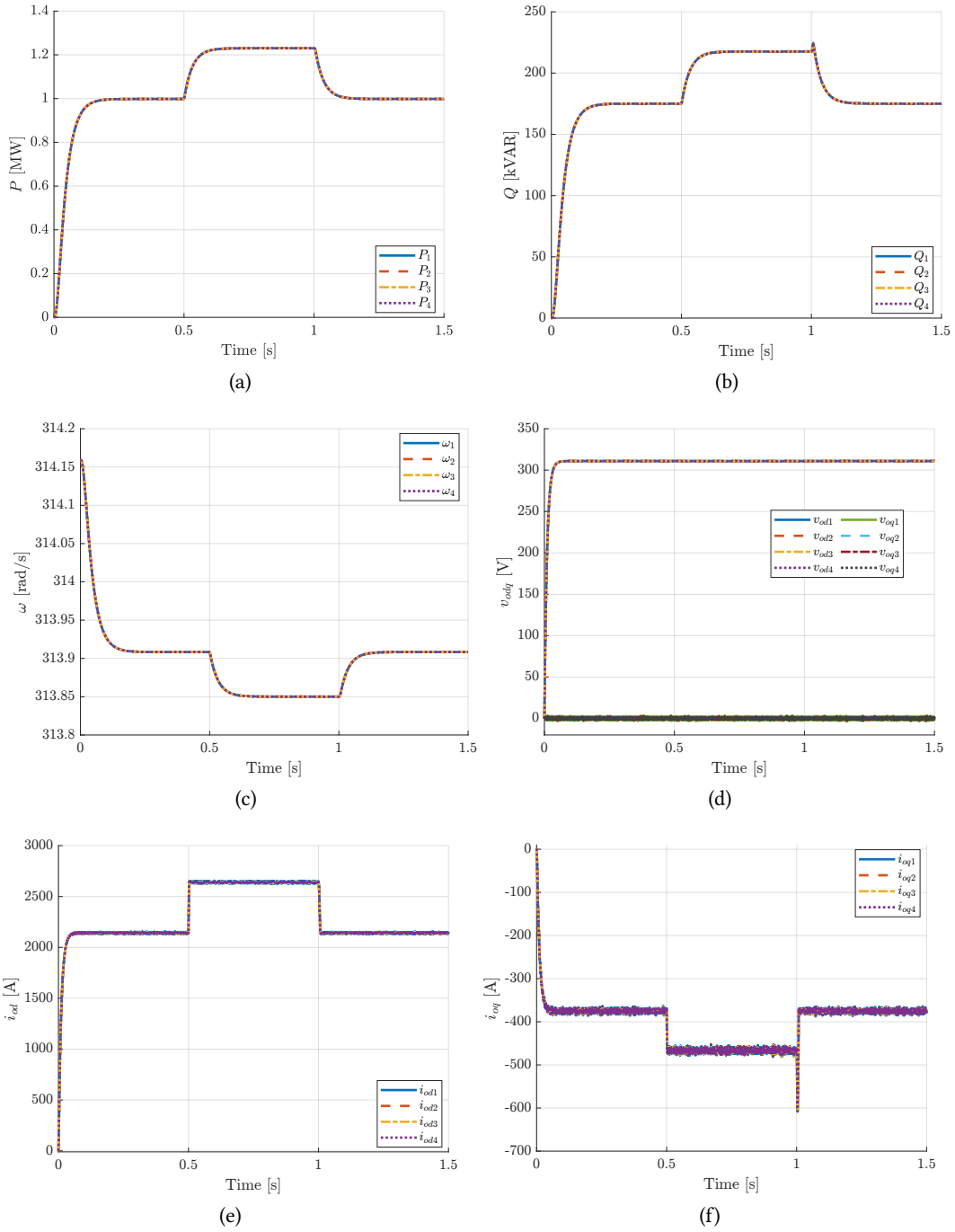

Fig. 4.9: Simulation results of the virtual impedance-based control strategy: (a) Real power sharing, (b) Reactive power sharing, (c) Frequency synchronization, (d) dq-axis voltage output, (e) d-axis current sharing, and (f) q-axis current sharing.

The effectiveness and flexibility of the control scheme are validated through simulations of four VSCs, each rated at 1.25 MVA, connected in parallel to a common bus via an LCL filter (see Fig. 4.15). The droop settings for all converters are listed in Table 4.1, where identical gains are assigned to each VSC to support proportional power sharing throughout the simulation. A static load of 4.07 MVA is applied across the microgrid throughout the simulation, with an additional switchable load of 1.02 MVA engaged at t = 0.5 s and disconnected at t = 1 s, simulating realistic load disturbances.

Simulation results (Fig.4.9) demonstrate that the proposed virtual complex impedance-based control strategy effectively enables all VSC units to proportionally adjust their outputs in response to load variations. During load disturbances, such as the connection and disconnection of switchable loads, the droop-controlled VSCs regulate their power outputs in accordance with the load changes, ensuring balanced sharing of both active and reactive power, as illustrated in Figs.4.9a and 4.9b. As a result, frequency synchronization and voltage regulation are maintained within acceptable limits, as shown in Figs.4.9c and 4.9d. Moreover, Figs.4.9e and 4.9f show that the d-axis current (i_{od}) and q-axis current (i_{oq}) are accurately shared among the VSC units under the proposed control approach. During load disturbances, both i_{od} and i_{oq} dynamically follow the load demand, contributing to the delivery of real and reactive power, respectively. The system exhibits well-damped transient responses, indicating the controller's ability to adapt to dynamic load changes without compromising stability. These results confirm the effectiveness of the proposed decentralized control strategy in managing load transitions and maintaining overall system performance without requiring centralized coordination.

While simulation results confirm that the controller maintains stability and effective load sharing under dynamic conditions, the virtual complex impedance method introduces notable structural trade-offs. Specifically, it adds an additional control loop atop the conventional voltage and current controllers, complicating coordination, increasing computational burden, and raising potential stability concerns under varying operating scenarios [137], [138]. Moreover, if the virtual impedance loop is not carefully integrated with the inner control layers, it may lead to inconsistent or conflicting control actions, ultimately diminishing system performance [137]. Under dynamic loading conditions, these coordination challenges can become more pronounced, posing risks to system stability [139]. An additional limitation arises from indirect performance degradation: although no physical impedance is introduced, the emulated behavior alters power flow and dynamic response, increasing control effort and potentially elevating switching losses or regulatory burden, thereby reducing overall efficiency [137]. Motivated by these limitations, this study presents a PSO-based simulation framework as an alternative strategy—focused on optimizing control parameters to improve performance while reducing design complexity in VSC-based islanded microgrids [94].

4.6.2 Evaluation of Computationally Guided PSO-Based Optimization Framework

The performance of the proposed optimization technique for VSC parameter tuning was evaluated using MATLAB/Simulink simulations on the test system depicted in Fig.4.2, while the simulation-based online parameter optimization of the islanded VSC—achieved by integrating PSO within the Simulink framework—is illustrated in the flow diagram of Fig.4.8. The key system specifications and VSC parameters are summarized in Tables 4.1 and 4.3. The proposed PSO-optimized approach—referred to as the PSO-PI method—was evaluated against a conventional method (CM) cited in prior studies [95], [104], [105], [112]. To further investigate its effectiveness in a more complex environment, the method was applied to a microgrid consisting of four VSCs connected in parallel to a common load at the PCC, as shown in Fig. 4.15.

4.6.3 Comparison of PSO-Optimized and Conventional Methods

The PSO algorithm is used to minimize an objective function, defined in Eq. (4.54), in order to identify the optimal LCL filter and controller parameters. The acceleration constants, φ_1 and φ_2, are set to 2.05, resulting in a combined parameter φ of 4.1 and a constriction coefficient χ of 0.7298, which regulates the particle velocity. Consequently, both the personal ($\chi\varphi_1$) and social ($\chi\varphi_2$) coefficients are 1.4962. Random variables r_1 and r_2, ranging between 0 and 1, are

Table 4.3: VSC Parameters for PSO-Optimized Approach.

Parameters	Value	Parameters	Value
$\Delta v_{tpu}(h_{sw})$	0.9091 pu	ϕ_m	68.5°
$\Delta i_{pu}(h_{sw})$	10%	PF_{max}	0.995
$\Delta i_{opu}(h_{sw})$	0.2%	q_{min}	0.0709 pu
R_f	0.1 $m\Omega$	τ_i	6.3662e^{-5} s
R_c	0.1 $m\Omega$	τ_v	1.7662e^{-3} s

Table 4.4: Selected boundaries of parameters to be optimized.

Parameters	Value	Parameters	Value
L_{Tmin}/L_{Tmax}	11.6410/36.9749 μH	$K_{pc}^{min}/K_{pc}^{max}$	0/0.2904
L_{fmin}/L_{fmax}	5.8205/18.4874 μH	$K_{ic}^{min}/K_{ic}^{max}$	0/157.0796
C_{fmin}/C_{fmax}	3709.3036/5423.8751 μF	$K_{pv}^{min}/K_{pv}^{max}$	0/11.1054
R_{dmin}/R_{dmax}	23.1040/1000 Ω	$K_{iv}^{min}/K_{iv}^{max}$	0/6287.8272

introduced to maintain population diversity and prevent premature convergence by adding stochasticity to the particle updates. Fig. 4.10a illustrates the convergence of the objective function over 50 iterations for a population size of 30. The optimized parameters obtained from this process are presented in Table 4.5.

For comparison, the VSC parameters obtained through the proposed PSO-optimized approach and the CM approach are presented in Table 4.6. The proposed method reduces the LCL filter's total inductance by 64.82% and capacitance by 16.67%, leading to a reduction in filter size. This results in lower losses and improved efficiency. While the CM method, as shown in Table 4.6, provides better attenuation of switching frequency components due to its higher inductance, the proposed method achieves THD level below 5%, meeting the IEEE-519 standard. This is achieved with a smaller total inductance and capacitance, resulting in a minimized filter size while maintaining harmonic attenuation within the recommended range.

Table 4.5: Results from Parameter Optimization Using the PSO-Based Approach.

Parameters	**Value**	**Parameters**	**Value**
L_f	11.9197 μH	K_{pc}	0.2573
L_c	11.9197 μH	K_{ic}	12.7777
C_f	4110.4066 μF	K_{pv}	6.1291
R_d	25.1425 Ω	K_{iv}	5205.4504

Table 4.6: Comparison of Filter and Controller Parameters for PSO-Optimized and CM Approaches.

Parameters	**CM-approach [95], [104], [105], [112]**	**PSO-PI-approach**
μ	0.0210	1
λ	7.7339	4.9497
ω_{res}	12186 rad/s	19040.9269 rad/s
L_T	67.7680 μH	23.8390 μH
C_f	4932.4879 μF	4110.4066 μF
K_{pc}	1.0426	0.2573
K_{ic}	1.5708	12.7777
K_{pv}	1.7607	6.1291
K_{iv}	996.8826	5205.4504
THD_V	2.06%	2.32%
THD_I	2.24%	2.44%
t_s	11.70 ms	4.47 ms
t_r	1.41 ms	0.52 ms
M_p	29%	14.1%

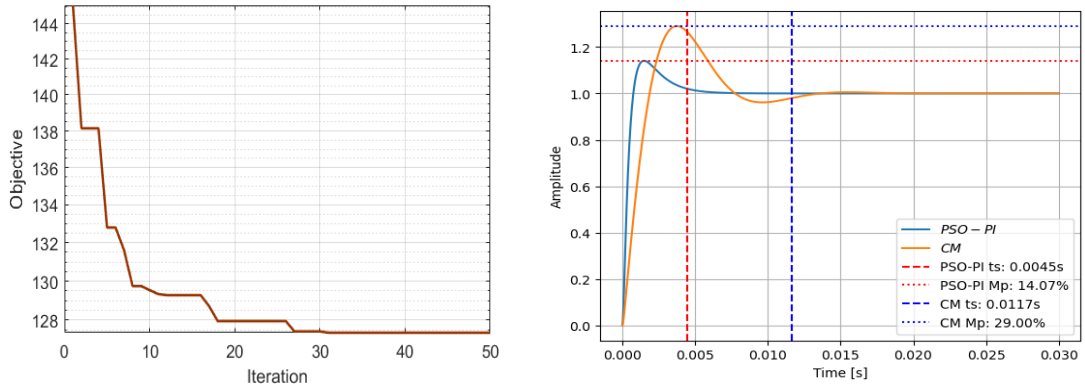

(a) (b)

Fig. 4.10: (a) Objective function convergence. (b) Transient and steady-state response of CM and PSO-PI methods.

The transient and steady-state responses of the closed-loop control system for the proposed PSO-optimized approach, as well as the CM approach, are shown in Fig. 4.10b. The PSO-optimized approach outperforms the CM in terms of rise time, settling time, and overshoot, achieving a rise time of 0.52 ms, a settling time of 4.47 ms, and a maximum overshoot of 14.1%. In contrast, the CM results in a larger LCL filter with a slower rise time of 1.41 ms, a longer settling time of 11.70 ms, and a maximum overshoot of 29%.

4.6.4 Testing and Evaluation of the PSO-Optimized Approach

The performance of the PSO-optimized control method was assessed by simulating various operational scenarios, including voltage reference variations, inductive and capacitive step load changes, and the integration of nonlinear loads. The study was further extended to configurations involving multiple VSC connected to a common load, as shown in Fig. 4.15.

VSC Response to Voltage Reference Variation

To evaluate the closed-loop system's ability to accurately follow a reference signal, a step change is introduced to the voltage amplitude command. The system initially operates with a reference voltage of $V_o = 311$ V, supplying an inductive load of $(1000 + j185)$kVA. At $t = 0.5$s, the reference voltage is reduced by 20%, and then restored to $V_o = 311$ V at $t = 1$ s. The system response to this perturbation is illustrated in Fig.4.11. As shown in Figs.4.11a and 4.11b, the output voltage v_{od} closely tracks the reference V_o, indicating effective voltage regulation. The q-axis voltage v_{oq} remains near zero, maintaining proper decoupling and supporting system stability.

Figs. 4.11c and 4.11d further show that the output currents i_{od} and i_{oq} accurately follow their respective references i^*_{od} and i^*_{oq}. By holding v_{oq} at zero and ensuring close current tracking,

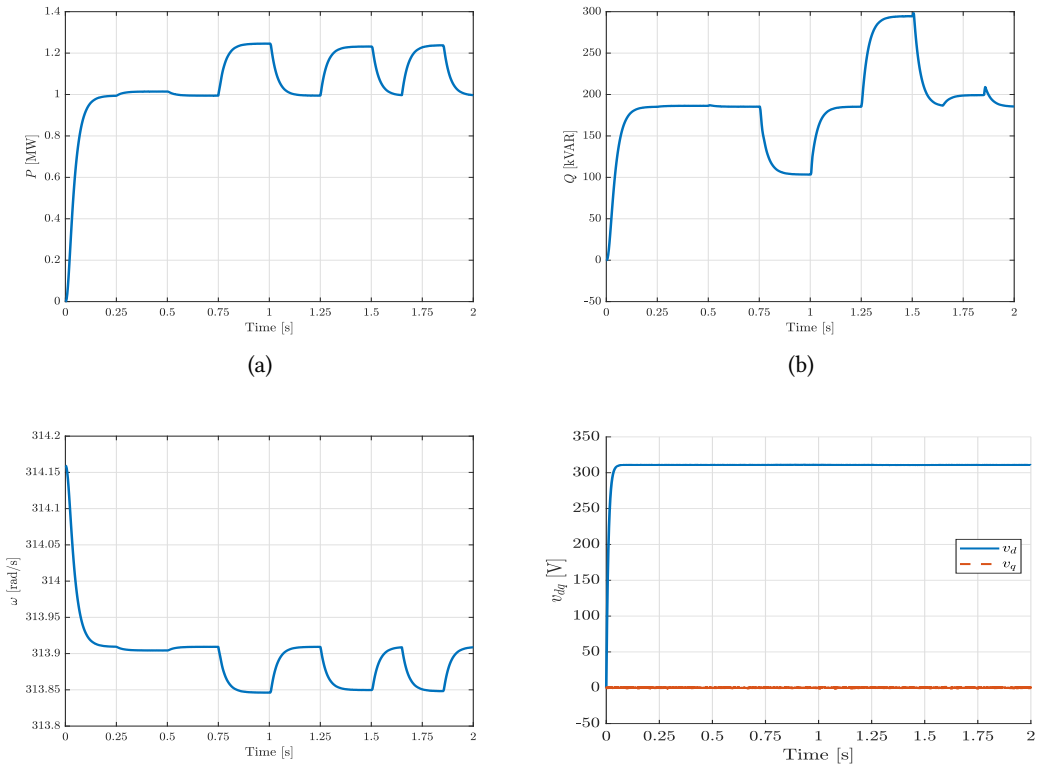

Fig. 4.11: Voltage and current responses to reference variation: (a) dq-axis voltage, (b) Per-phase voltage, (c) dq-axis current, (d) Per-phase current.

independent control of real and reactive power through i_{od} and i_{oq} is maintained. Overall, the system demonstrates robust performance and accurate dynamic tracking despite the applied voltage perturbation.

VSC Response to Inductive Load Disturbance

The performance of the proposed PSO-optimized approach was examined under an inductive load disturbance. Initially, the VSC operated at 380 V and 50 Hz, supplying an inductive load of $(1000 + j185)$kVA. At $t = 0.5$s, an additional inductive load of $(250 + j55)$kVA was suddenly connected, and disconnected at $t = 1$s. As shown in Fig. 4.12a, the output voltages v_{od} and v_{oq} closely follow their respective references throughout the disturbance, with no observable overshoot in either axis.

With the increased load, the VSC dynamically adjusted to maintain power balance, as reflected in the real and reactive power responses shown in Figs.4.12b and4.12c. Due to the inductive nature of the disturbance, the VSC compensated for the lagging power factor by supplying reactive power. Operating in island mode, the system experienced frequency variation caused

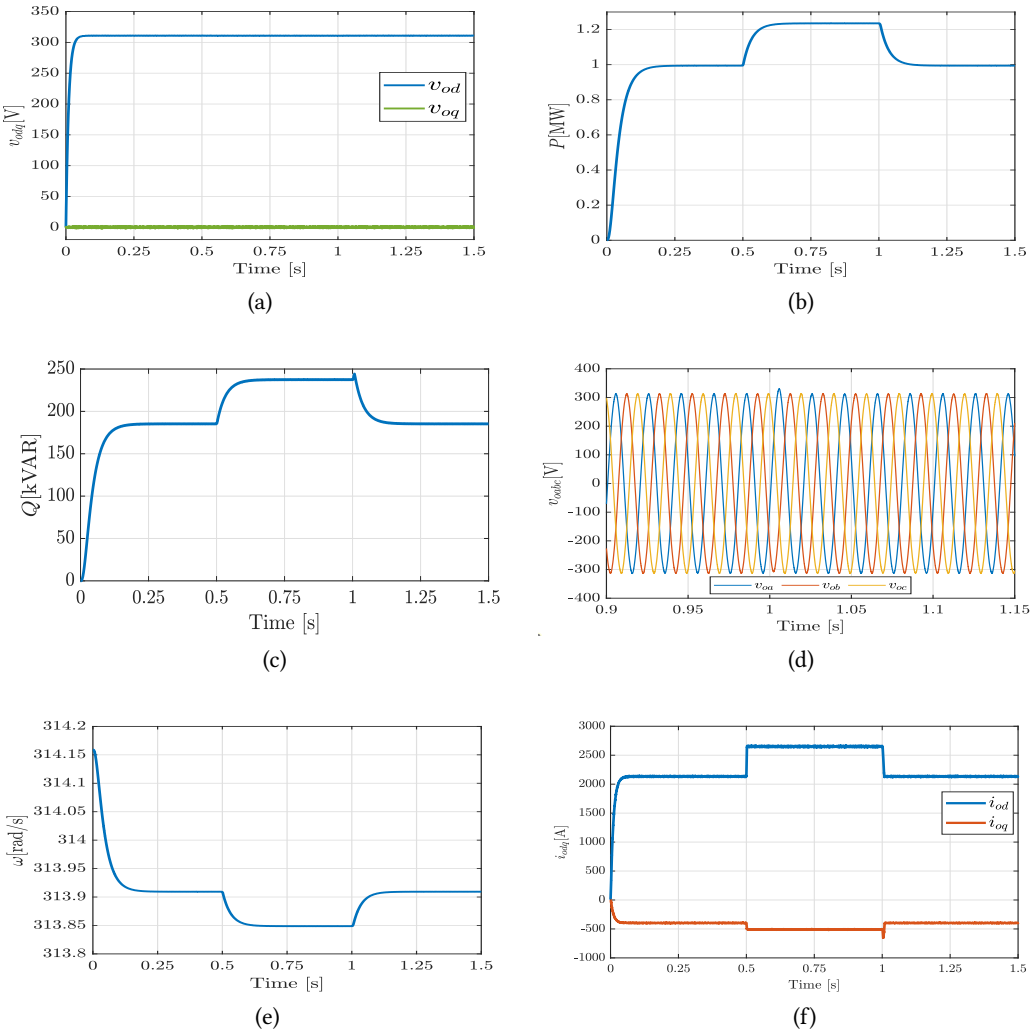

Fig. 4.12: VSC response to inductive load disturbance: (a) dq-axis voltage, (b) Real power, (c) Reactive power, (d) Per-phase voltage, (e) Frequency, (f) dq-axis current.

by power imbalance and droop control effects, but the deviation remained within acceptable bounds, as shown in Fig. 4.12e.

The current components i_{od} and i_{oq} adapted to the changing load without exhibiting transient overshoot, as depicted in Fig.4.12f. The negative values observed in i_{oq} reflect the adopted dq-reference convention, as explained in Eq.(4.6). Overall, the results confirm the system's ability to maintain stable operation under inductive load disturbances with well-regulated voltages and currents.

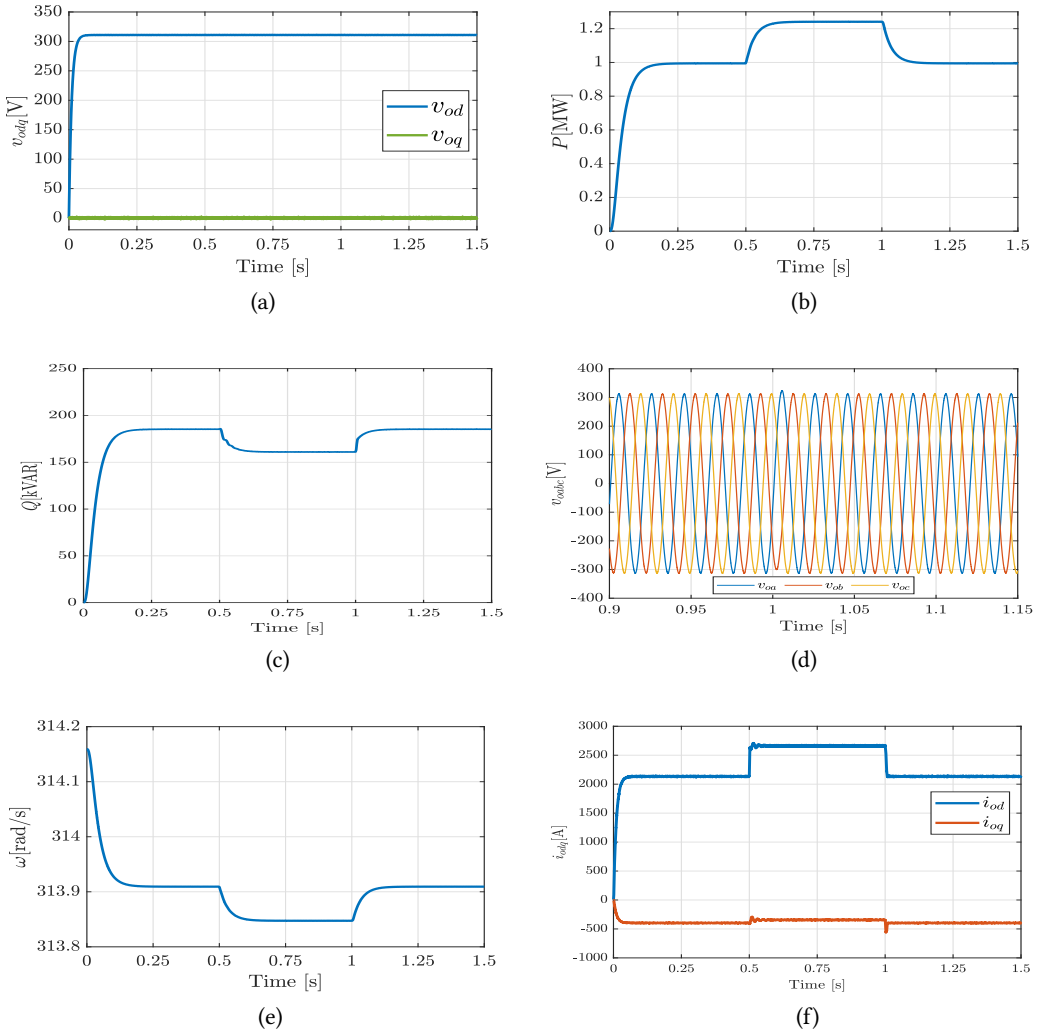

Fig. 4.13: VSC response to capacitive load disturbance: (a) dq-axis voltage, (b) Real power, (c) Reactive power, (d) Per-phase voltage, (e) Frequency, (f) dq-axis current.

VSC Response to Capacitive Load Disturbance

To further assess the system's performance with the optimized filter and controller parameters, a capacitive load disturbance was introduced, maintaining the same initial operating conditions as those used in the inductive load disturbance scenarios. At $t = 0.5$ s, a capacitive load of $(250 - j25)$kVA was abruptly connected and then disconnected at $t = 1$ s. As illustrated in Fig. 4.13a, the output voltages v_{od} and v_{oq} tracked their respective reference signals throughout the event, maintaining stable voltage regulation.

Following the load change, the VSC dynamically adjusted its operation to balance both real and reactive power, as shown in Figs. 4.13b and 4.13c. In response to the capacitive nature of the disturbance, the VSC absorbed reactive power to counteract the leading power factor.

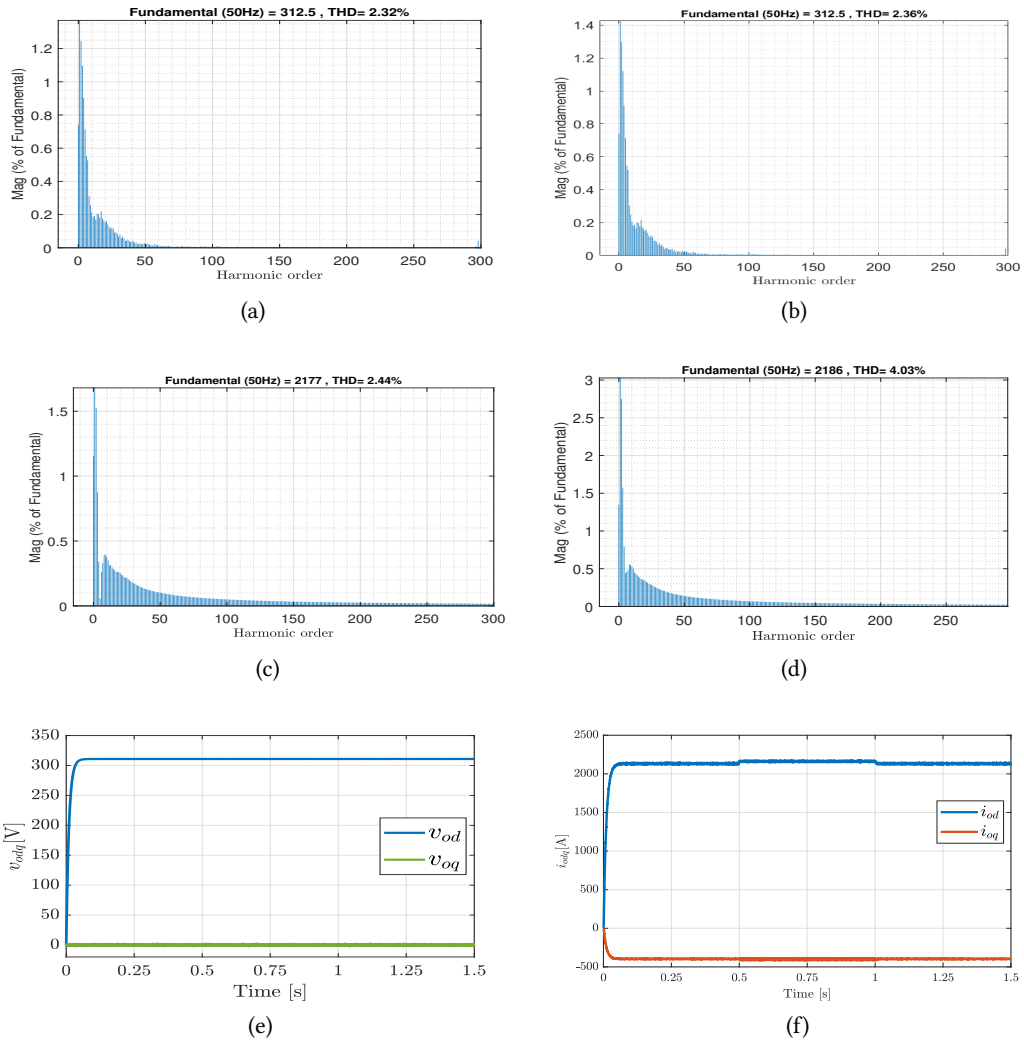

Fig. 4.14: VSC response to nonlinear load integration: (a) Voltage THD without nonlinear load, (b) Voltage THD with nonlinear load, (c) Current THD without nonlinear load, (d) Current THD with nonlinear load, (e) dq-axis voltage, (f) dq-axis current.

This contrasts with the inductive case, where the VSC supplied reactive power to address the lagging power factor. Thus, the system demonstrated its ability to provide reactive power support as needed—either absorbing or injecting—based on the load characteristics.

Operating in islanded mode, the system experienced some frequency variation due to instantaneous power imbalances and droop characteristics, but these deviations remained within acceptable limits, as indicated in Fig.4.13e. The current components i_{od} and i_{oq} responded smoothly to the changing load conditions without any overshoot, as shown in Fig.4.13f. These results highlight the controller's responsiveness and reliability under capacitive load disturbances.

VSC Response to Nonlinear Load Disturbance

In this test scenario, a VSC operating in islanded mode—under the same initial conditions as in the inductive and capacitive load disturbance scenarios—is subjected to a nonlinear load disturbance. At $t = 0.5$ s, a 10 kW nonlinear load, interfaced through a rectifier, is suddenly connected and then disconnected at $t = 1$ s. This test evaluates the system's performance under nonlinear loading conditions.

As shown in Figs.4.14a and4.14b, the THD of the output voltage increases from 2.32% to 3.36% due to the nonlinear load. Similarly, the output current THD rises from 2.44% to 4.03%, as illustrated in Figs.4.14c and 4.14d. Despite the increase, the harmonic distortion levels remain within acceptable limits. Moreover, the harmonic content of the dq-axis voltages and currents shows only minor variation before and after the disturbance, as seen in Figs.4.14e and4.14f. The results indicate that the proposed control scheme maintains satisfactory performance even under nonlinear load conditions.

Extension of the Proposed Approach to a Multi-VSC System

The proposed PSO-optimized approach was rigorously evaluated in a complex system featuring four 1.25 MVA VSCs connected in parallel in islanded mode, linked to a common AC bus at the PCC via an LCL filter, as depicted in Fig. 4.15. Initially, the system operates at 380 V (line-to-line) and 50 Hz, with a static inductive load of $(Z_{LC} = 4 + j0.74)$ MVA continuously applied at the PCC throughout the entire simulation period.

To ensure stable operation, the droop coefficients are precisely designed to maintain an allowable voltage drop ratio of 0.25% and an allowable frequency droop of 0.1%. The d-axis and q-axis voltage references, v_{od}^* and v_{oq}^*, are set to 311 V and 0 V, respectively, for all VSCs. This configuration ensures that the VSCs share both real and reactive power equally, maintaining system balance and stability. These design goals are uniformly applied across all VSCs to ensure that voltage and frequency remain within the required settings.

To assess the system's performance under dynamic load conditions, a step load change was introduced through a switchable load ($Z_{sw} = 1 + j0.22$) MVA, which was applied at t = 0.5 s and disconnected at t = 1.0 s. This test evaluates the effectiveness of the PSO-optimized controllers and their accuracy in power-sharing control. The results, illustrated in Fig. 4.16, demonstrate the controllers' capability to maintain system stability and performance under varying load conditions. As depicted in Fig. 4.16a, the d-axis and q-axis output voltage responses of all four VSCs accurately track their respective reference inputs despite load increments in both real and reactive powers. As shown in Figs. 4.16b and 4.16c, real and reactive power are faithfully shared in equal ratios among the VSC. This accurate power sharing is ensured for active and reactive powers, even under load disturbances. Each VSC adjusts its frequency to meet load

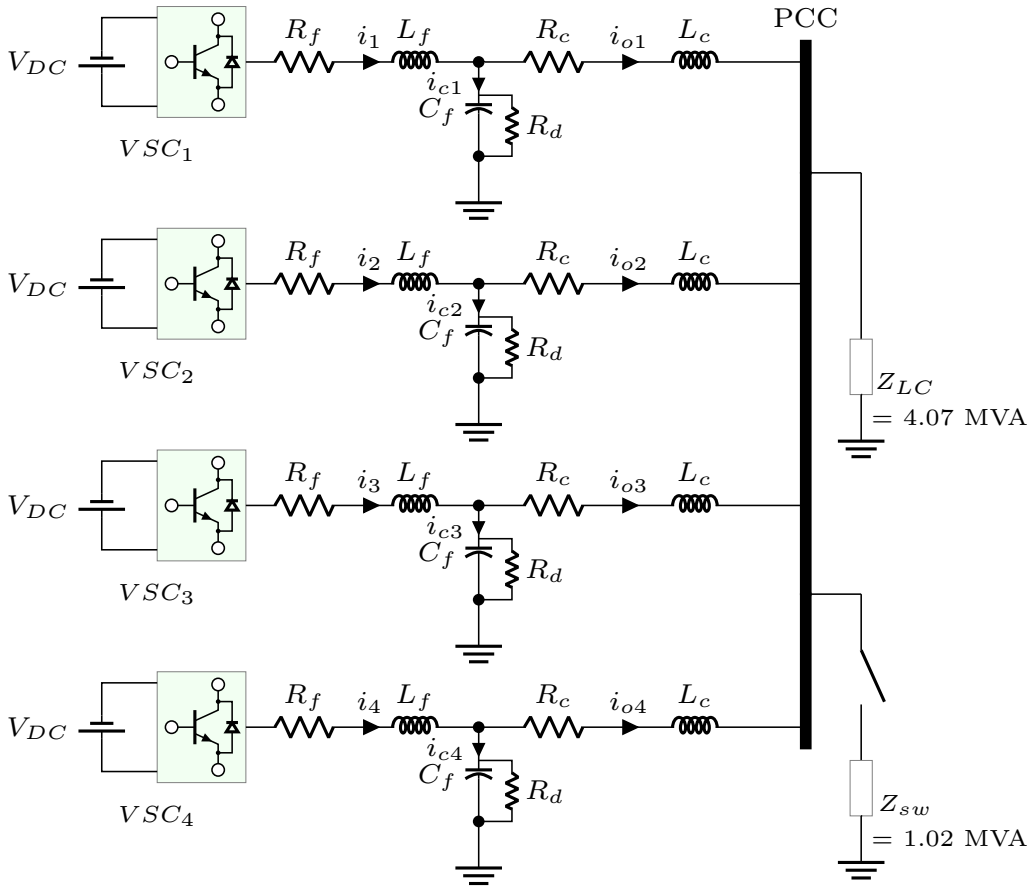

Fig. 4.15: Multi-VSC-based islanded microgrid case study.

demand as the load varies to keep synchronization among all VSCs.

After a brief transient interval, all VSC units operate at the same frequency, as illustrated in Fig. 4.16d. As depicted in Figs. 4.16e and 4.16f, the d-axis current i_{od} and q-axis current i_{oq} are accurately shared among VSC units based on the proposed control strategy. During the load disturbance interval, both the d-axis current i_{od} and q-axis current i_{oq} of each VSC follow the load to meet the required demand in real power and reactive power, respectively. Hence, the proposed design exhibits good performance and desirable responses for step load change scenarios when implemented in systems with multiple VSCs.

As shown in Fig. 4.15, all VSCs share a common load at the PCC. The control strategy described in this paper aims to maintain the voltage v_{od} across the filter capacitor C_f at a reference value V_o, which is essential for ensuring stable and efficient VSC operation. To achieve this, the load voltage at the PCC, v_{Ld}, must closely match v_{od}, which requires careful optimization of the coupling impedance.

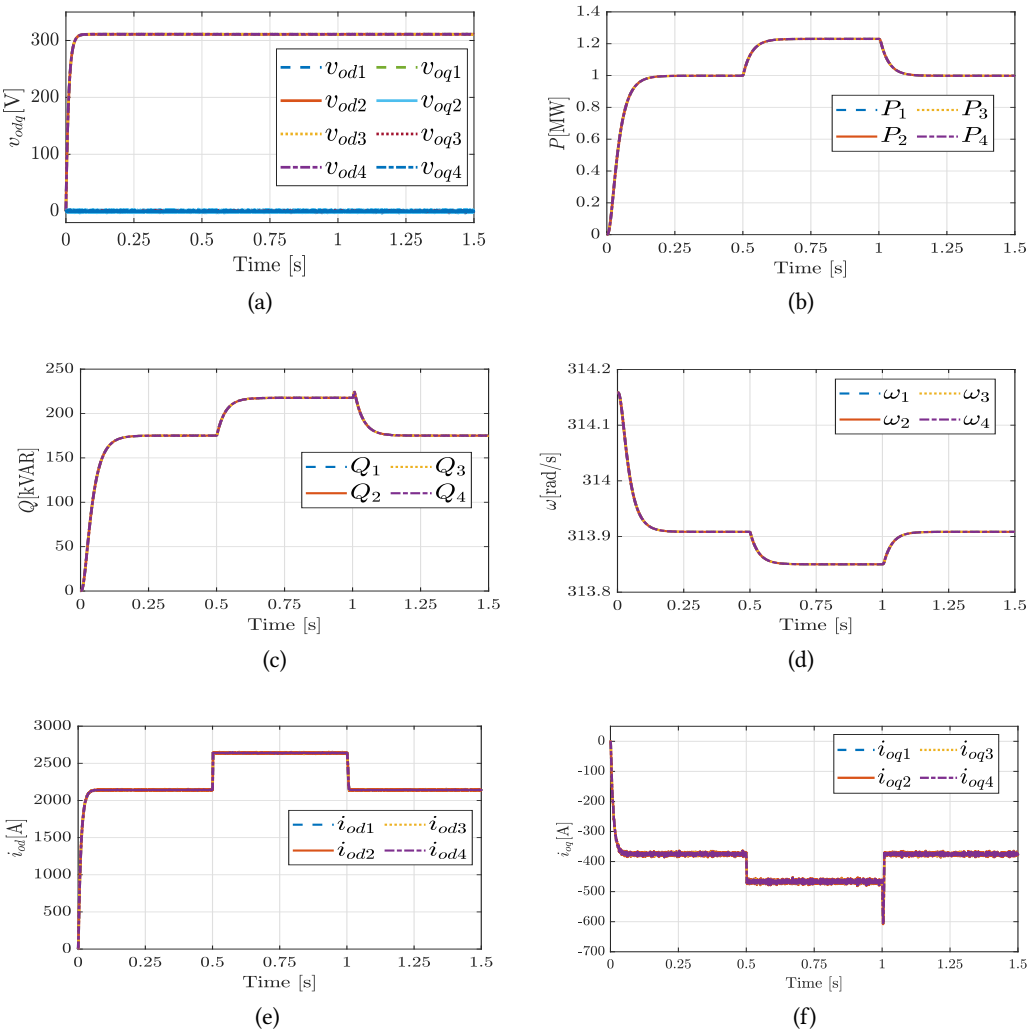

Fig. 4.16: Performance of parallel VSCs: (a) dq-axis voltage sharing, (b) Real power sharing, (c) Reactive power sharing, (d) Frequency synchronization, (e) d-axis current sharing, (f) q-axis current sharing.

The coupling impedance significantly influences both voltage regulation and power loss in the system. A high impedance can cause substantial voltage drops and reduce overall efficiency. On the other hand, minimizing impedance to reduce losses introduces a trade-off with power quality—specifically, THD. While lower inductance decreases losses, it also weakens harmonic attenuation, potentially leading to unacceptable THD levels in sensitive applications. Therefore, selecting an appropriate impedance value requires careful balancing between efficiency, voltage stability, and harmonic performance.

As illustrated in Fig. 4.17a, the voltage at the PCC closely tracks the input reference signal-311 V on the d-axis and zero on the q-axis. Fig.4.17b shows the total d-axis and q-axis output currents reflecting the imposed load dynamics, verifying that the current control loop responds

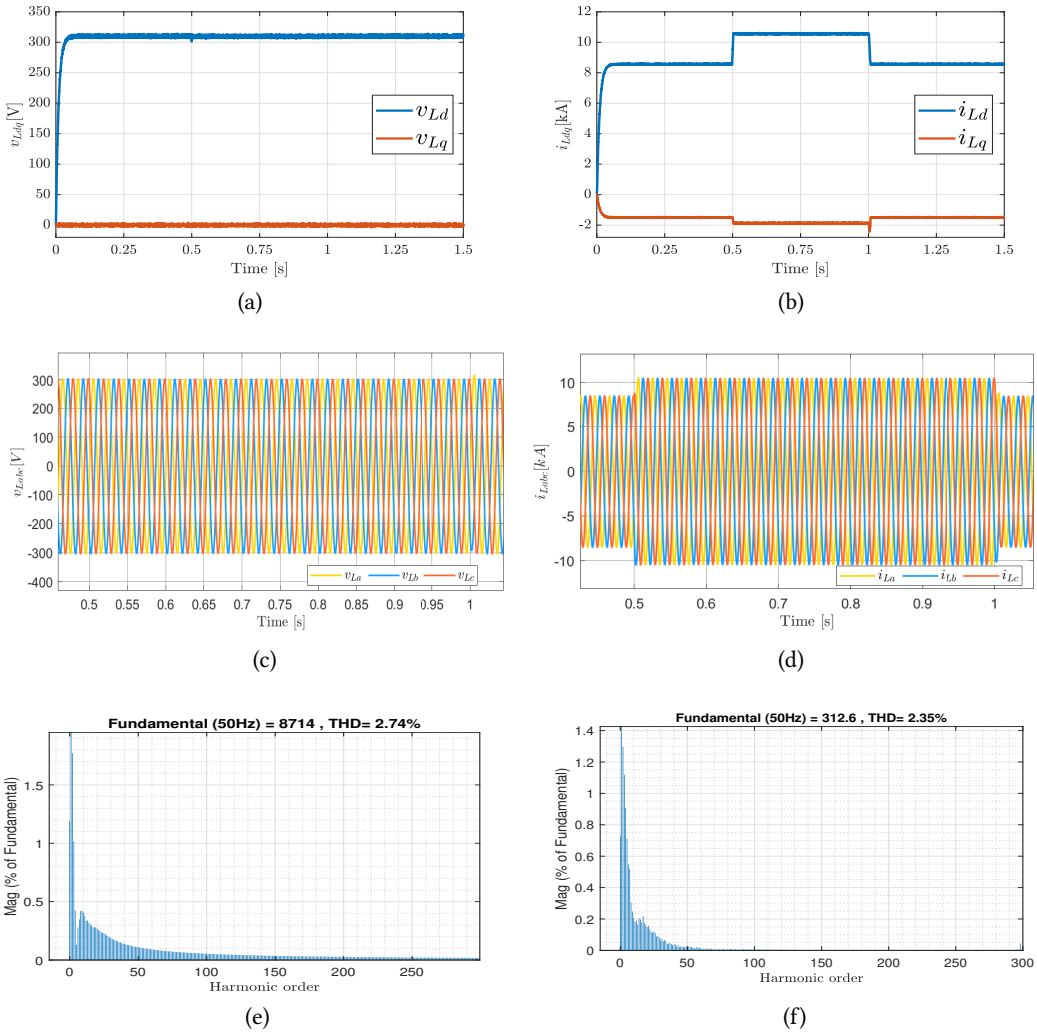

Fig. 4.17: System performance at PCC: (a) dq-axis voltage, (b) dq-axis load currents, (c) per-phase voltage, (d) per-phase load current, (e) load current THD, (f) PCC voltage THD.

consistently to system load disturbance. The per-phase sinusoidal AC representation of load voltage and current, shown in Figs. 4.17c and 4.17d, reveals that the harmonic content of the waveforms is minimal. As depicted in Figs. 4.17e and 4.17f,the THD of the output currents and voltages is 2.74% and 2.35%, respectively, which complies with the IEEE-519 standard. In summary, the PSO-optimized control strategy ensures that the three-phase output voltage at the PCC remains within the required statutory limits, demonstrating the robustness and validity of the proposed control technique.

Chapter 5

Neuroevolutionary Training of MLP Controllers for Voltage–Frequency Regulation in VSC-Based Islanded Microgrid

5.1 Introduction

The increasing integration of RES into power systems, alongside the growing demand for reliable, efficient, and resilient power delivery, has driven the development of islanded MGs capable of operating independently from the main grid [3], [4], [23]. Among these,VSC-based islanded MGs have garnered significant attention due to their flexibility in integrating diverse energy sources and maintaining voltage and frequency stability under varying operating conditions [87], [140]. However, controlling such MGs remains challenging, particularly in ensuring accurate voltage and frequency regulation amidst system disturbances, fluctuating load conditions, and the inherent variability of renewable generation [141], [142].

To address these control challenges, particularly in dynamic and uncertain environments, advanced AI techniques—especially machine learning (ML) and its subfield, deep learning (DL)—offer promising solutions. These AI-driven approaches enhance the reliability, efficiency, and adaptability of power systems by improving monitoring, forecasting, control, and decision-making processes [23], [143]. Among these, neural networks have shown particular promise for controller design in complex systems like islanded MGs, due to their ability to model nonlinear dynamics and adapt to changing operational conditions [144].

This study introduces a computationally guided framework for training Multilayer Perceptron

Controllers (MLPCs) specifically designed for voltage and frequency regulation in VSC-based islanded MGs. MLPs are well-suited for this task due to their capacity to model complex, nonlinear system dynamics. However, their performance is highly dependent on the appropriate tuning of both network parameters and architectural hyperparameters. Traditional training methods often face limitations such as slow convergence rates and poor generalization, particularly when navigating high-dimensional and nonconvex optimization landscapes.

To overcome these challenges, we propose the Adaptive Hybrid PSO-Embedded GA (AH-PEGA), an advanced optimization framework that embeds PSO within a GA structure. AH-PEGA incorporates dynamic adjustment of PSO coefficients, adaptive mutation and crossover mechanisms in the GA, localized refinement strategies, and population resizing with elitism to balance convergence speed and solution diversity. This framework enables the joint optimization of MLPC parameters and hyperparameters, and its effectiveness is validated through extensive simulations across a range of operating conditions.

5.2 Neuroevolutionary Optimization of MLP Controllers in VSC-Based Islanded Microgrids

The control framework adopted in this thesis builds upon the cascaded voltage and current control loops of a two-level VSC connected to a common AC bus through an LCL filter, as detailed in Chapter 4. The corresponding mathematical formulations and structural representations of the power, voltage, and current control loops—illustrated in Fig. 5.1—are thoroughly

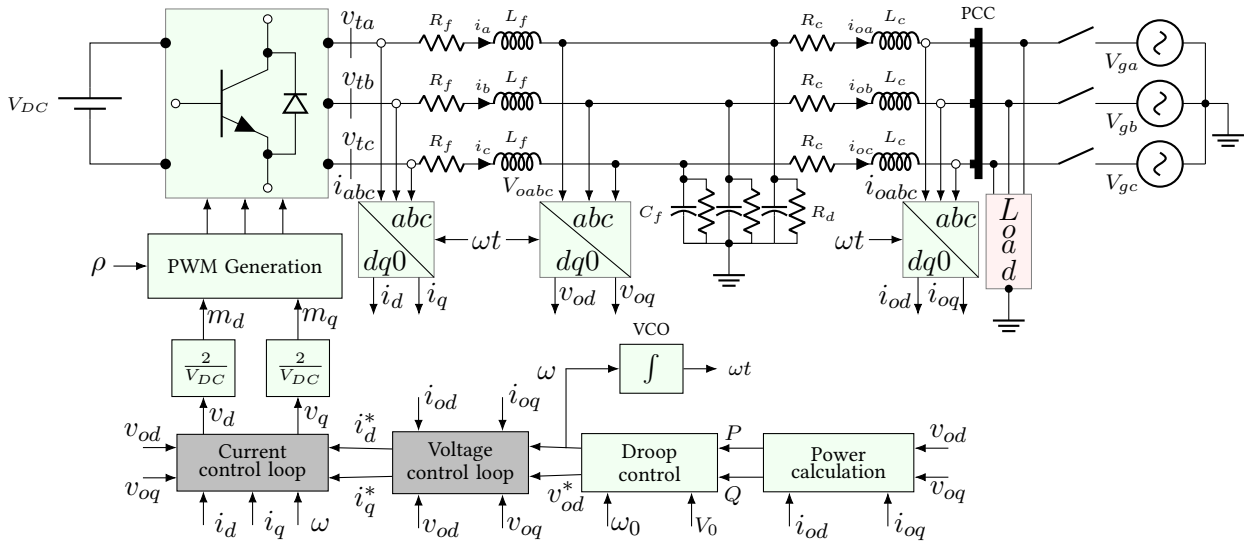

Figure 5.1: Schematic of VSC system with LCL filters and cascaded control loops.

addressed therein. Building on this foundation, the present section focuses on the neuroevolutionary design of MLPC optimized for voltage and frequency regulation using the proposed AHPEGA framework.

5.2.1 Mathematical Formulation of Feedforward MLP Neural Network

A feedforward MLP model processes input features through successive hidden layers to generate output predictions, following a structured learning flow [145]. To balance model complexity and computational efficiency, this study employs a neural network with three hidden layers—sufficient to capture complex nonlinear mappings while supporting effective generalization. In the context of training MLPCs for VSC-based islanded MG, the network is designed

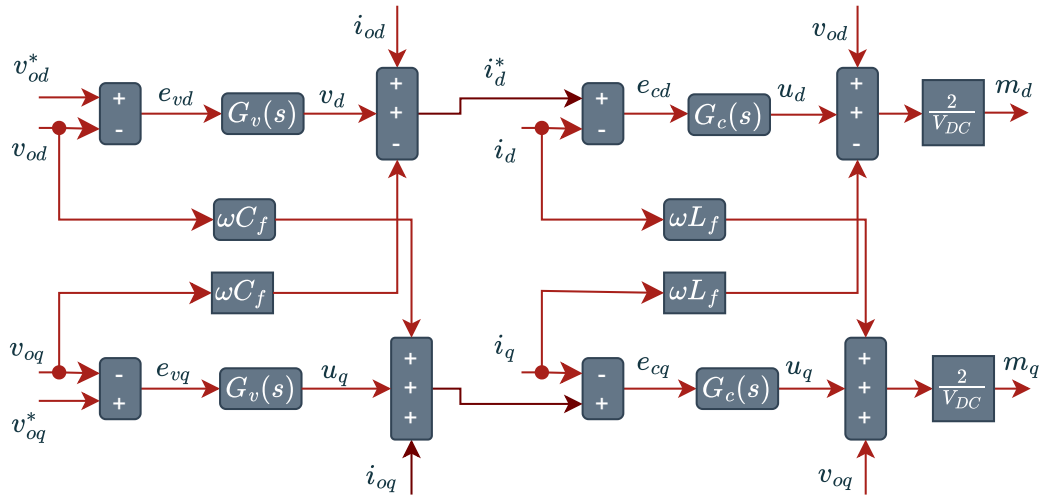

(a)

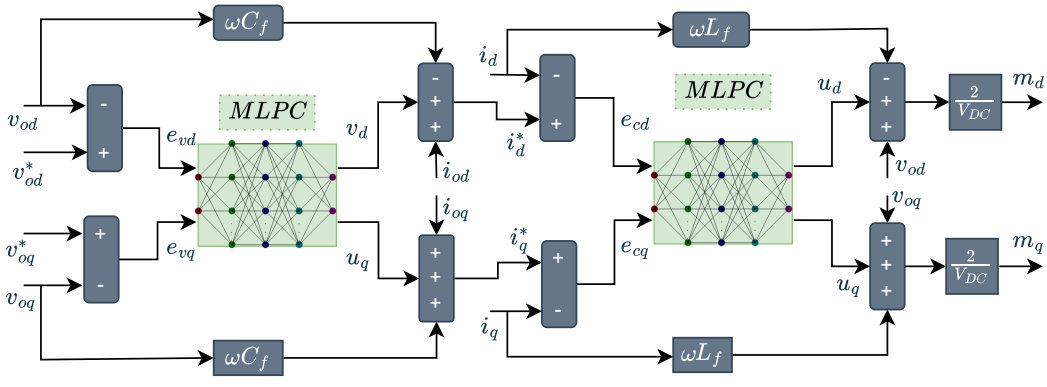

(b)

Fig. 5.2: (a) General structure of voltage and current control in VSC systems. (b) AHPEGA-optimized MLPC-based implementation of voltage and current control in VSC.

to map input-output relationships involving the dq-axis control variables.

Based on Eqns. (4.17) and (4.25) from Chapter 4, the corresponding input vector $\mathbf{e}$ is formulated as follows:

$$\mathbf{e} = \begin{bmatrix} e_d \\ e_q \end{bmatrix} \tag{5.1}$$

where e_d and e_q are the input features of dimension 2×1 for the d-axis and q-axis, respectively.

Assuming a maximum of p neurons per hidden layer, a suitable neuroevolutionary algorithm is employed to determine the optimal network structure, including the number of neurons and the associated weight and bias values. Based on the MLP structure illustrated in Fig. 5.3, the forward computations proceed layer by layer once the network architecture is defined. The weight matrix $\mathbf{W}^{(1)}$ and bias vector $\mathbf{b}^{(1)}$, connecting the input layer to the first hidden

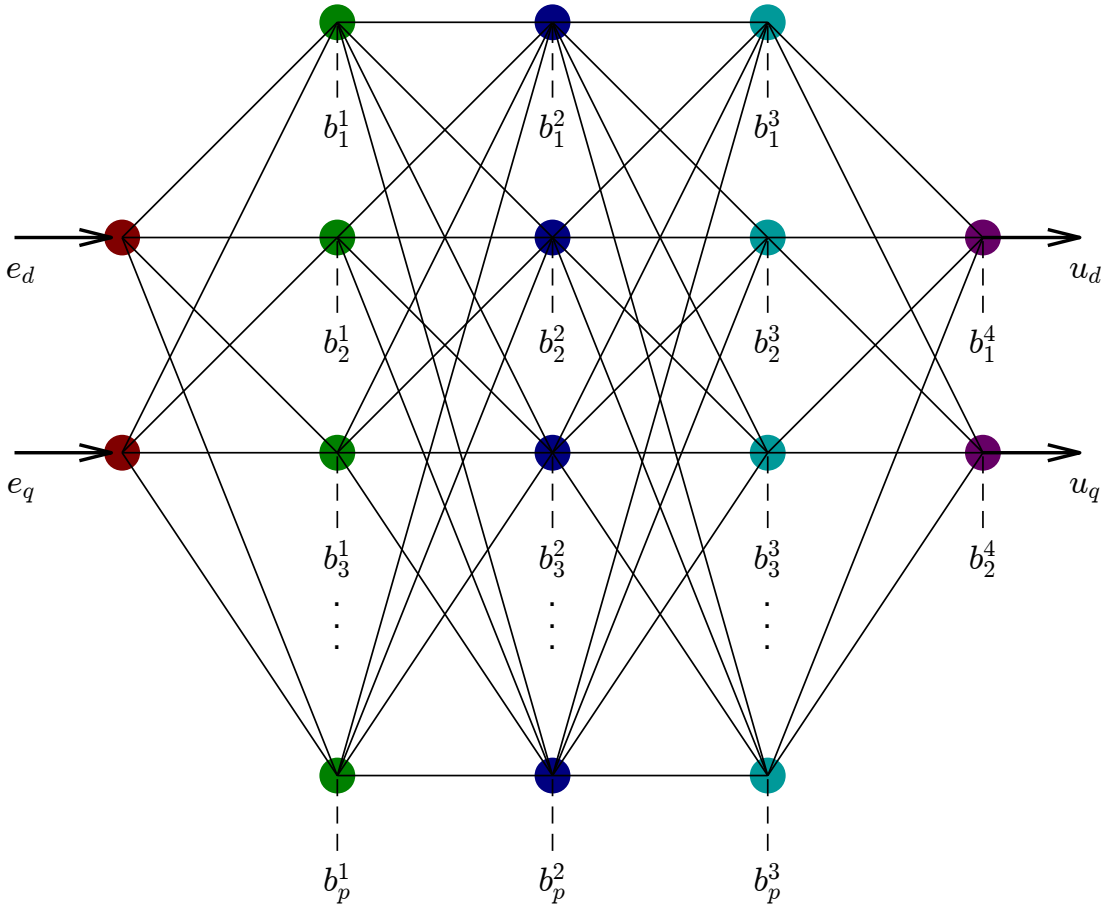

Fig. 5.3: Architecture of the feedforward MLP neural network employed for training MLPCs, showing the arrangement of input, hidden, and output layers.

layer (with up to p nodes), are defined as:

$$\mathbf{W}^{(1)} = \begin{bmatrix} W_{11}^{(1)} & W_{12}^{(1)} \\ W_{21}^{(1)} & W_{22}^{(1)} \\ \vdots & \vdots \\ W_{p1}^{(1)} & W_{p2}^{(1)} \end{bmatrix}; \quad \mathbf{b}^{(1)} = \begin{bmatrix} b_1^{(1)} \\ b_2^{(1)} \\ \vdots \\ b_p^{(1)} \end{bmatrix}$$

The output of the first hidden layer, $\mathbf{h}^{(1)}$, is computed as:

$$h_i^{(1)} = \sigma\left(\sum_{j=1}^{2} W_{ij}^{(1)} x_j + b_i^{(1)}\right) \quad \text{for} \quad i = 1, 2, \ldots, p; \quad \mathbf{h}^{(1)} = \begin{bmatrix} h_1^{(1)} \\ h_2^{(1)} \\ \vdots \\ h_p^{(1)} \end{bmatrix}$$

where $\sigma(\cdot)$ denotes the activation function applied at each node.

The second hidden layer receives $\mathbf{h}^{(1)}$ as input. Its weight matrix and bias vector are defined as:

$$\mathbf{W}^{(2)} = \begin{bmatrix} W_{11}^{(2)} & W_{12}^{(2)} & \cdots & W_{1p}^{(2)} \\ W_{21}^{(2)} & W_{22}^{(2)} & \cdots & W_{2p}^{(2)} \\ \vdots & \vdots & \ddots & \vdots \\ W_{p1}^{(2)} & W_{p2}^{(2)} & \cdots & W_{pp}^{(2)} \end{bmatrix}; \quad \mathbf{b}^{(2)} = \begin{bmatrix} b_1^{(2)} \\ b_2^{(2)} \\ \vdots \\ b_p^{(2)} \end{bmatrix}$$

The output of the second hidden layer is:

$$h_i^{(2)} = \sigma\left(\sum_{j=1}^{p} W_{ij}^{(2)} h_j^{(1)} + b_i^{(2)}\right) \quad \text{for} \quad i = 1, 2, \ldots, p; \quad \mathbf{h}^{(2)} = \begin{bmatrix} h_1^{(2)} \\ h_2^{(2)} \\ \vdots \\ h_p^{(2)} \end{bmatrix}$$

Similarly, the third hidden layer uses:

$$\mathbf{W}^{(3)} = \begin{bmatrix} W_{11}^{(3)} & W_{12}^{(3)} & \cdots & W_{1p}^{(3)} \\ W_{21}^{(3)} & W_{22}^{(3)} & \cdots & W_{2p}^{(3)} \\ \vdots & \vdots & \ddots & \vdots \\ W_{p1}^{(3)} & W_{p2}^{(3)} & \cdots & W_{pp}^{(3)} \end{bmatrix}; \quad \mathbf{b}^{(3)} = \begin{bmatrix} b_1^{(3)} \\ b_2^{(3)} \\ \vdots \\ b_p^{(3)} \end{bmatrix}$$

with corresponding output:

$$h_i^{(3)} = \sigma\left(\sum_{j=1}^{p} W_{ij}^{(3)} h_j^{(2)} + b_i^{(3)}\right) \quad \text{for} \quad i = 1, 2, \ldots, p; \quad \mathbf{h}^{(3)} = \begin{bmatrix} h_1^{(3)} \\ h_2^{(3)} \\ \vdots \\ h_p^{(3)} \end{bmatrix}$$

Finally, the output layer, which maps to the d-axis and q-axis outputs, uses:

$$\mathbf{W}^{(4)} = \begin{bmatrix} W_{11}^{(4)} & W_{12}^{(4)} & \cdots & W_{1p}^{(4)} \\ W_{21}^{(4)} & W_{22}^{(4)} & \cdots & W_{2p}^{(4)} \end{bmatrix}; \quad \mathbf{b}^{(4)} = \begin{bmatrix} b_1^{(4)} \\ b_2^{(4)} \end{bmatrix}$$

and the final output $\mathbf{u} = [u_d \; u_q]^T$ is computed as:

$$u_i = \sigma\left(\sum_{j=1}^{p} W_{ij}^{(4)} h_j^{(3)} + b_i^{(4)}\right) \quad \text{for} \quad i = 1, 2; \quad \mathbf{u} = \begin{bmatrix} u_d \\ u_q \end{bmatrix} \tag{5.2}$$

5.2.2 Data Processing

In this research, data is generated through simulation-based techniques using MATLAB/Simulink models of the MG, as shown in Fig. 5.1. The system operates under a cascaded control architecture employing conventional proportional-integral (PI) controllers. Input and output signals from these controllers are recorded at each time step across a range of operating conditions, ensuring that the neural network is trained on a diverse and representative dataset. Given the converter's high switching frequency of 15 kHz, the sampling rate is set to 750,000 data points per second throughout the data acquisition period. This results in a rich dataset of input-output pairs suitable for training the neural controller. Prior to training, the raw data is preprocessed to enhance compatibility with the neural network. Specifically, it is normalized to the range $[-1, 1]$, in accordance with the hyperbolic tangent activation function, defined as:

$$\tanh(z_i^{(l)}) = \frac{e^{z_i^{(l)}} - e^{-z_i^{(l)}}}{e^{z_i^{(l)}} + e^{-z_i^{(l)}}} \tag{5.3}$$

where

$$z_i^{(l)} = \sum_{j=1}^{p} W_{ij}^{(l)} h_j^{(l-1)} + b_i^{(l)}, \quad \text{for } i = 1, \ldots, p$$

The $tanh$ function maps inputs to $[-1, 1]$, making it well-suited for outputs centered around zero. Normalization is performed by first scaling the data to $[0, 1]$ and then shifting it to match

the target range as:

$$x = 2 \cdot \left(\frac{x - x_{\min}}{x_{\max} - x_{\min}} \right) - 1 \tag{5.4}$$

This process enhances learning efficiency by maintaining consistency across feature scales, leading to faster convergence of the neural network.

5.2.3 Loss Function and Constraints

The loss function $J(x)$ quantifies the error between the predicted output u_i and the actual target value $\hat{u}_i$. It is tailored to optimize MLPCs by minimizing the mean squared error (MSE) between estimated and actual outputs. The function is defined as:

$$J(x) = \frac{1}{N} \sum_{i=1}^{N} (u_i - \hat{u}_i)^2 \tag{5.5}$$

where u_i denotes the predicted output for the i^{th} sample, $\hat{u}_i$ is the corresponding ground truth value, and N is the total number of data samples.

The optimization process seeks to minimize $J(x)$ while adhering to structural constraints that ensure the neural network remains both feasible and computationally efficient. These constraints apply to the number of neurons in the hidden layers, synaptic weights, and biases, and are formulated as:

$$\text{Minimize } J(x) \text{ subject to: } n_{l,j} \leq n_j \leq n_{u,j}; \quad w_{l,j} \leq w_j \leq w_{u,j}; \quad b_{l,j} \leq b_j \leq b_{u,j}$$

where n_j is the number of neurons in the j^{th} hidden layer, bounded by $n_{l,j}$ and $n_{u,j}$; w_j is the synaptic weight, constrained between $w_{l,j}$ and $w_{u,j}$; and b_j is the bias term, limited within the range $b_{l,j}$ to $b_{u,j}$.

5.2.4 Performance Evaluation Indices

The performance of the AHPEGA-driven MLPCs is evaluated using standard regression metrics to ensure an accurate and reliable assessment of the model's predictive capability. Specifically, this study reports the Mean Squared Error (MSE), Root Mean Squared Error (RMSE), Normalized Mean Squared Error (NMSE), Mean Absolute Error (MAE), Coefficient of Determination (R^2), and Pearson Correlation Coefficient (R), as defined below.

$$\text{MSE} = \frac{1}{n} \sum_{i=1}^{n} (u_i - \hat{u}_i)^2; \quad \text{NMSE} = \frac{\frac{1}{n} \sum_{i=1}^{n} (u_i - \hat{u}_i)^2}{\frac{1}{n} \sum_{i=1}^{n} (\hat{u}_i - \bar{u})^2};$$

$$R^2 = 1 - \frac{\sum_{i=1}^{n}(u_i - \hat{u}_i)^2}{\sum_{i=1}^{n}(u_i - \bar{u})^2}; \quad R = \frac{\sum_{i=1}^{n}(u_i - \bar{u})(\hat{u}_i - \bar{\hat{u}})}{\sqrt{\sum_{i=1}^{n}(u_i - \bar{u})^2 \sum_{i=1}^{n}(\hat{u}_i - \bar{\hat{u}})^2}};$$

$$\text{RMSE} = \sqrt{\frac{1}{n}\sum_{i=1}^{n}(u_i - \hat{u}_i)^2}; \quad \text{MAE} = \frac{1}{n}\sum_{i=1}^{n}|u_i - \hat{u}_i|.$$

where u_i are the actual values (targets), $\hat{u}_i$ are the predicted values (predictions), $\bar{u}$ is the mean of the target values, and $\bar{\hat{u}}$ is the mean of the predicted values. Lower values for MSE, RMSE, NMSE, and MAE generally indicate a better-performing regression model. Values closer to 0 indicate a better fit, while higher values indicate a poorer fit. Specifically, for NMSE, values closer to 1 indicate a poor fit. R^2 tells you how well your model explains the variability in the data, while R tells you the strength and direction of the linear relationship between two variables. R^2 values range from 0 to 1, where $R^2 = 1$ means the model explains all the variability of the response data around its mean, and $R^2 = 0$ means the model explains none of the variability of the response data around its mean. For R, values closer to 1 or -1 indicate a stronger linear relationship, while values closer to 0 indicate a weaker linear relationship.

5.3 Neuroevolutionary Optimization of MLP Controllers Driven by AHPEGA

Following the acquisition of training data, the next step involves optimizing the MLPCs through a computationally guided algorithm. Conventional backpropagation (BP) techniques are hindered by slow convergence and vulnerability to local minima. While heuristic methods like PSO and GA provide certain advantages—PSO offers rapid convergence and GA excels in global search—they also exhibit limitations: PSO can stagnate prematurely, and GA often lacks fine-grained exploitation.

To overcome these drawbacks, this study proposes the Adaptive Hybrid PSO-Embedded GA (AHPEGA), a novel optimization framework that embeds PSO within a GA structure, as illustrated in Fig. 5.4. AHPEGA is designed to simultaneously optimize both the parameters (weights and biases) and hyperparameters (e.g., the number of hidden layer neurons) of MLPCs—an integrated approach not commonly addressed in prior studies.

By incorporating PSO and local search mechanisms within GA, AHPEGA capitalizes on the fast convergence behavior of PSO and the robust global search capability of GA. It introduces adaptivity through dynamic tuning of PSO's inertia weights and cognitive-social coefficients, effectively balancing exploration and exploitation over time.

To further enhance optimization robustness, mutation operators are embedded within PSO to

avoid local stagnation, while GA utilizes adaptive mutation and crossover strategies to preserve population diversity and drive convergence. One of the distinctive features of AHPEGA is its adaptive population resizing strategy, which departs from traditional fixed-population approaches and enables more efficient convergence through selective elitism.

5.3.1 Dynamic Population

A larger population enhances exploration but can slow convergence and increase the computational burden, whereas a smaller population accelerates convergence but may overlook superior solutions and risk premature convergence. To manage this trade-off, AHPEGA starts with a larger population to promote broad exploration of the solution space and gradually reduces it over successive iterations, allowing the algorithm to shift focus toward fine-tuning and exploitation. The algorithm dynamically adjusts the population size by sorting individuals based on cost, retaining top-performing candidates, and replacing the worst-performing ones, thereby preserving elite particles throughout the optimization process. Particles x_i are sorted in ascending order based on their cost values $J(x_i)$ as:

$$x_i = \{x_{(1)}, x_{(2)}, \ldots, x_{(P)}\}; \quad \text{where} \quad J(x_{(1)}) \leq J(x_{(2)}) \leq \ldots \leq J(x_{(P)})$$

Then the top n_e elite particles x_i^e are retained as:

$$x_i^e = \{x_{(1)}, x_{(2)}, \ldots, x_{(n_e)}\}$$

The particle array is adjusted to the current size P as given below:

$$P = \left\lceil (P_i - (P_i - P_f)\left(\frac{k+1}{T+1}\right)^{\alpha} \right\rceil \tag{5.6}$$

where $\lceil \cdot \rceil$ denotes the rounding function, P_i is the initial number of particles, P_f is the final number of particles, k is the current iteration, and T is the total number of iterations for the main loop.

The last n_e particles in the adjusted array are replaced with the elite particles as:

$$x_{(P-n_e+1)}, x_{(P-n_e+2)}, \ldots, x_{(P)} = x_{(1)}^e, x_{(2)}^e, \ldots, x_{(n_e)}^e$$

where $x_{(P-n_e+i)}$ denotes the $(P - n_e + i)^{th}$ particle in the adjusted array, and $x_{(i)}^e$ denotes the i^{th} elite particle.

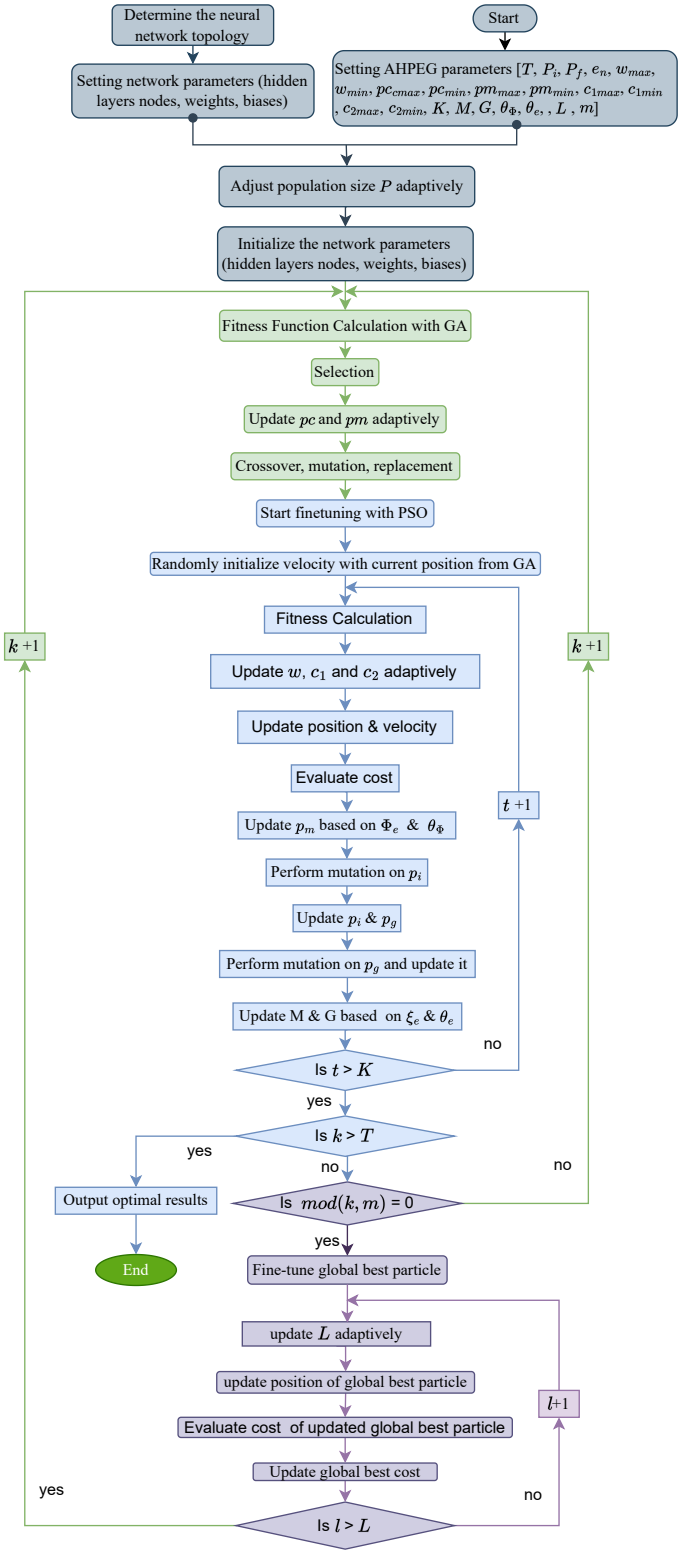

Fig. 5.4: Flowchart of the Adaptive Hybrid PSO-Embedded GA (AHPEGA) algorithm for training Multi-layer Perceptron Controllers (MLPCs).

5.3.2 GA Operators

Selection

Tournament selection is employed to choose individuals from the population for crossover and mutation. In this method, a subset of individuals is randomly selected from the population, and the best individual is chosen based on their fitness. The selected subset, referred to as the tournament group $\mathcal{T}$, is evaluated, and the individual with the highest fitness (or lowest cost) within this group is selected to participate in the next generation. Let $x_i = \{x_1, x_2, \ldots, x_P\}$ represent the population, where P is the population size, and $J(x_i)$ denotes the fitness of individual x_i. A subset of $\mathcal{T}$ individuals selected from the population x_i be denoted as:

$$\mathcal{T} = \{\pi_{i_1}, \pi_{i_2}, \ldots, \pi_{i_\mathcal{T}}\}$$

where π_{ij} is the j^{th} individual randomly selected from the population. Then, the fitness of each individual in the tournament group is evaluated as:

$$J(\pi_{ij}) \quad \text{for} \quad j = 1, 2, \ldots, \mathcal{T}.$$

The winner of the tournament is the individual with the best fitness, which can be expressed as:

$$x_\mathcal{T} = \arg\min_{x_{ij} \in \mathcal{T}} J(x_{ij}) \tag{5.7}$$

where $\arg\min$ returns the individual with the minimum (or best) fitness value in the tournament group $\mathcal{T}$. This process is repeated until P individuals have been selected for the next generation.

Dynamically Adjusted Crossover and Mutation

This study utilizes the Probabilistic Blend Crossover ($BLX - \alpha$), a real-valued crossover method, to produce offspring. Given two parent individuals $x_{p1,i}^{(k)}$ and $x_{p2,i}^{(k)}$, the offspring genes $x_{o1,i}^{(k)}$ and $x_{o2,i}^{(k)}$ are generated as follows:

$$\begin{cases} x_{o1,i}^{(k)} = L_i + r \cdot (U_i - L_i), & \text{if } r \leq p_c \\ x_{o2,i}^{(k)} = L_i + r \cdot (U_i - L_i), & \text{if } r \leq p_c \\ x_{o1,i}^{(k)} = x_{p1,i}^{(k)}, & \text{if } r > p_c \\ x_{o2,i}^{(k)} = x_{p2,i}^{(k)}, & \text{if } r > p_c \end{cases} \tag{5.8}$$

$$\forall k \in \{1, 2, \ldots, T\}, \quad \forall i \in \{1, 2, \ldots, P\}.$$

where L_i and U_i are defined as:

$$L_i = \min(x_{p1,i}^{(k)}, x_{p2,i}^{(k)}) - \alpha \cdot |x_{p1,i}^{(k)} - x_{p2,i}^{(k)}|, \quad U_i = \min(x_{p1,i}^{(k)}, x_{p2,i}^{(k)}) + \alpha \cdot |x_{p1,i}^{(k)} - x_{p2,i}^{(k)}|$$

where α can be selected between 0.1 and 0.5 and r is a random number between 0 and 1.

To help in exploring the search space more effectively and escape local optima, a mutation technique integrated with mutation rate p_m is used as given below:

$$x_{oi}^{(k)} = \begin{cases} x_{oi}^{(k)} + \Delta m_i^{(k)}, & \text{if } r \leq p_m \\ x_{oi}^{(k)}, & \text{otherwise} \end{cases} \tag{5.9}$$

$$\forall k \in \{1, 2, \ldots, T\}, \quad \forall i \in \{1, 2, \ldots, P\}.$$

where r is a random number and Δm represents the perturbation applied to the particle's position and defined as:

$$\Delta m_i = \beta(u_i^b - l_i^b)(2r - 1)$$

Here, β is a scaling factor that controls the magnitude of the perturbation, while u_i^b and l_i^b represent upper and lower bounds for the mutation, respectively. The perturbation is either added to or subtracted from the current value $x_i^{(k)}$, with the direction determined randomly.

The condition for adaptively adjusting p_c and p_m is given as:

$$\begin{cases} p_m = \min(p_{m_{\max}}, p_m + \Delta p_m), & \text{if } \sigma \leq \theta_\sigma \\ p_c = \min(p_{c_{\max}}, p_c + \Delta p_c), & \text{if } \sigma \leq \theta_\sigma \\ p_m = \max(p_{m_{\min}}, p_m - \Delta p_m), & \text{if } \sigma > \theta_\sigma \\ p_c = \max(p_{c_{\min}}, p_c - \Delta p_c), & \text{if } \sigma > \theta_\sigma \end{cases} \tag{5.10}$$

$$\forall k \in \{1, 2, \ldots, T\}, \quad \forall i \in \{1, 2, \ldots, P\}.$$

where

$$\Delta p_m = p_{m_{max}} - (p_{m_{max}} - p_{m_{min}}) \left(\frac{k+1}{T+1} \right)^\alpha; \quad \Delta p_c = p_{c_{max}} - (p_{c_{max}} - p_{c_{min}}) \left(\frac{k+1}{T+1} \right)^\alpha$$

$$\sigma = \sqrt{\frac{1}{P} \sum_{i=1}^{P} (C_i - \mu_C)^2}; \quad \theta_\sigma = 0.1 \frac{1}{P} \sum_{i=1}^{P} C_i$$

where C_i is the personal best cost at each iteration and μ_C is the mean of the costs.

Probabilistic Kill Tournament-Based Replacement Technique

The probabilistic kill tournament replacement technique is used to replace either the worst or second worst individual in a tournament group with a new offspring generated through crossover or mutation. Let $x_i = \{x_1, x_2, \ldots, x_P\}$ represent the population of size P, and let $\mathrm{J}(x_i)$ denote the cost (or fitness) of individual x_i. The tournament group $\mathcal{T}$ is selected from the population $\mathcal{P}$, and this subset is denoted as follows:

$$\mathcal{T} = \{\pi_{i_1}, \pi_{i_2}, \ldots, \pi_{i_\mathcal{T}}\}, \quad \text{such that} \quad \pi_i \in \{1, 2, \ldots, P\}.$$

where π_{ij} represents the j-th individual randomly selected from the population. Then the tournament individuals are sorted in ascending order as:

$$\mathrm{J}(x_{\pi_1}) \leq \mathrm{J}(x_{\pi_2}) \leq \cdots \leq \mathrm{J}(x_{\pi_\mathcal{T}}).$$

The worst individual in the tournament is replaced based on the probability p_r as:

$$\begin{aligned} &\text{if } r \leq p_r: \quad x_{\pi_T} \leftarrow x_{\text{oi}}, \quad \mathrm{J}(x_{\pi_T}) \leftarrow \mathrm{J}(x_{\text{oi}}) \\ &\text{if } r > p_r: \quad x_{\pi_{T-1}} \leftarrow x_{\text{oi}}, \quad \mathrm{J}(x_{\pi_{T-1}}) \leftarrow \mathrm{J}(x_{\text{oi}}) \end{aligned} \tag{5.11}$$

5.3.3 PSO Operators

In PSO, the optimization process is guided by a set of operators that govern how the particles in the swarm interact with one another and update their velocities and positions [135]. After the particles are initialized, the iterative optimization process begins, where the following recursive equations update the velocities of all the particles:

$$v_{ij}^{(k+1)} = \omega^{(k)} v_{ij}^{(k)} + c_1^{(k)} r_1 (p_{ij}^{(k)} - x_{ij}^{(k)}) + c_2^{(k)} r_2 (g_j^{(k)} - x_{ij}^{(k)}) \tag{5.12}$$

where k is the current iteration, and r_1 and r_2 are random numbers between 0 and 1. Based on the updated velocities, each particle changes its position as follows:

$$x_{ij}^{(k+1)} = x_{ij}^{(k)} + v_{ij}^{(k+1)} \tag{5.13}$$

Inertia Weight and Acceleration Coefficients

Among various techniques, one commonly adopted strategy is to employ a time-varying inertia weight that decreases throughout the optimization process. This helps balance the trade-off between global exploration and local exploitation. A large initial inertia weight encourages broad search space exploration, while a gradually reduced weight promotes fine-tuning

around promising regions. In Eq. (5.14), the inertia weight $\omega^{(k)}$ decreases non-linearly according to a predefined schedule, enabling smooth adjustment across iterations:

$$\omega^{(k)} = \omega_{\max} - (\omega_{\max} - \omega_{\min}) \left(\frac{k+1}{T+1} \right)^{\alpha} \tag{5.14}$$

where $\omega_{\max}$ and $\omega_{\min}$ are the maximum and minimum inertia weights, k is the current iteration, T is the total number of iterations, and α controls the non-linearity of the decay, typically selected in the range [0.5, 2]. Fig. 5.5 illustrates the behavior of $\omega^{(k)}$ for $\alpha = 0.5$. This method enables a more controlled and gradual shift from exploration to exploitation, which is crucial for avoiding premature convergence and ensuring solution quality.

In eq. 5.15, the cognitive and social learning factors, c_1 and c_2, determine the extent to which a particle is influenced by its own experience (cognitive) and the experience of the swarm (social). As illustrated in Fig. 5.5, this study adopts a strategy where higher values of c_1 and lower values of c_2 are used during the early iterations to encourage independent exploration. Conversely, lower values of c_1 and higher values of c_2 are employed in later iterations to

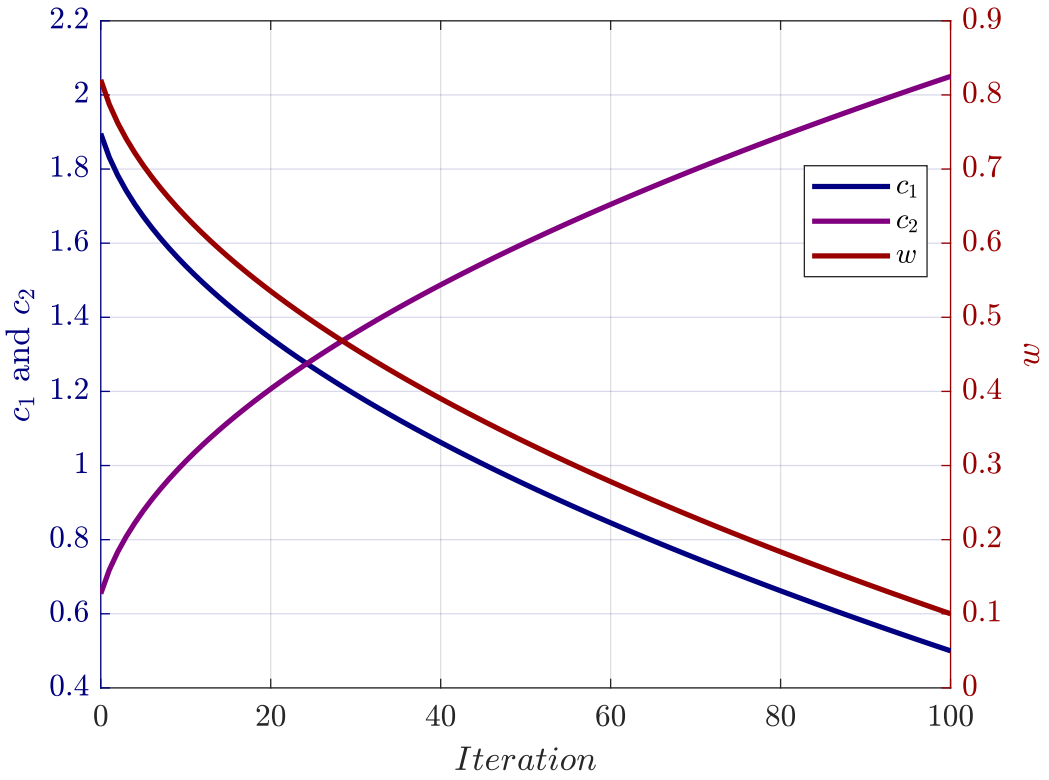

Fig. 5.5: Variation of dynamic inertia weight (right) and acceleration coefficients (left) in the PSO algorithm.

promote convergence through social learning. Mathematically, it is given as:

$$c_1^{(k)} = c_{1max} - (c_{1max} - c_{1min})\left(\frac{k+1}{T+1}\right)^{\alpha}$$
$$c_2^{(k)} = c_{2min} + (c_{2max} - c_{2min})\left(\frac{k+1}{T+1}\right)^{\alpha} \tag{5.15}$$

Mutation Strategies for Personal and Global Best

A mutation is applied to both the personal best of each particle and the global best position during optimization, aiming to prevent stagnation in local optima, preserve diversity, and accuracy. The value of the mutation probability p_m can be adjusted as:

$$p_m = \begin{cases} \min(p_m^{max}, 1.1 \times p_m), & \text{if } \Phi \geq \theta_\Phi \\ \max(p_m^{min}, 0.9 \times p_m), & \text{if } \Phi < \theta_\Phi \end{cases}$$

where θ_Φ is diversity threshold and Φ is the diversity of particles and, defined as:

$$\Phi = \frac{1}{P}\sum_{i=1}^{P}\sqrt{\sum_{j=1}^{m}(x_{ij} - \bar{x}_j)^2}; \qquad \bar{x} = \frac{1}{P}\sum_{i=1}^{N} x_i$$

In proposed AHPEGA, the mutation on the best particle $p_i^{(t)}$ is given as:

$$p_{mi}^{(t)} = \begin{cases} p_i^{(t)} + \Delta m_i^{(t)}, & \text{if } r \leq p_m \\ p_i^{(t)}, & \text{otherwise} \end{cases} \quad \begin{array}{l} \forall k \in \{1, 2, \ldots, T\}, \\ \forall t \in \{1, 2, \ldots, K\}, \\ \forall i \in \{1, 2, \ldots, P\}, \\ \forall j \in \{1, 2, \ldots, M\} \end{array} \tag{5.16}$$

where r is a random number and Δm represents the perturbation applied to the particle's position, K is the maximum iteration for the PSO loop, M is the maximum iteration for mutation on the best particle.

After applying mutation to the personal best, the updated personal best $p_i^{(t)}$ is given by:

$$p_{mi}^{(t)} = \begin{cases} p_{mi}^{(t)}, & \text{if } J(x_{mi}^{(t)}) \leq J(p_i^{(t)}) \\ p_i^{(t)}, & \text{otherwise} \end{cases}; \quad g_m^{(t)} = \begin{cases} p_{mi}^{(t)} & \text{if } J(p_{mi}^{(t)}) \leq J(g^{(t)}) \\ g^{(t)} & \text{otherwise} \end{cases} \tag{5.17}$$

Since the global best particle $g^{(t)}$ guides the swarm, introducing small perturbations through mutation enables PSO to explore promising new regions of the search space rather than solely

refining a potentially suboptimal solution. Hence, in AHPEGA, mutation on the global best particle $g^{(t)}$ is performed as:

$$g_m^{(t)} = \begin{cases} g^{(t)} + \Delta m^{(t)} & \text{if } r \leq p_m \\ g^{(t)} & \text{otherwise} \end{cases} \quad \begin{array}{l} \forall k \in \{1, 2, \ldots, T\}, \\ \forall t \in \{1, 2, \ldots, K\}, \\ \forall j \in \{1, 2, \ldots, G\} \end{array} \tag{5.18}$$

where G is the maximum iteration of mutation on the global best particle.

After performing mutation, global best particle $g^{(t)}$ is updated as:

$$g_m^{(t)} = \begin{cases} g_m^{(t)} & \text{if } J(g_m^{(t)}) \leq J(g^{(t)}) \\ g^{(t)} & \text{otherwise} \end{cases} \tag{5.19}$$

The perturbation Δx_i is defined as:

$$\Delta m_i = \beta(u_i^b - l_i^b)(2r - 1)$$

In AHPEGA, the iteration for mutation on best particles and global particle is adjusted adaptively based on the performance of particles. In case the global best cost reaches the stagnation threshold, the mutation iterations for each particle and global best particle are adjusted as:

$$\begin{cases} \text{if } \xi_e \quad \geq \quad \theta_e \text{ then} \\ \beta = \beta \times 1.1, \quad M = M + 1, \quad G = G + 1, \quad \xi = 0 \end{cases} \tag{5.20}$$

where ξ_e is the stagnation counter for the embedded PSO loop and θ_e is the stagnation threshold.

5.3.4 Fine-tuning Global Best Adaptively

In hybrid approaches such as AHPEGA, fine-tuning the global best particle allows the algorithm to efficiently exploit high-quality solutions while simultaneously exploring new regions through mutation. This dual mechanism helps maintain a dynamic balance between exploration and exploitation.

Within this framework, the number of local search iterations adapts over time and is computed as:

$$L = L_i + (L_f - L_i) \left(\frac{k+1}{T+1} \right)^{\alpha} \tag{5.21}$$

Table 5.1: Parameters of Adaptive Hybrid PSO-Embedded GA (AHPEGA)

Parameters of Neural Network	
Architecture	Multi-layer perceptron FNN
Number of layers	3
n_u	20
n_l	2
$\sigma(.)$	Tanh
$J(x)$	MSE
$b_u, \quad b_l$	1, -1
Parameters of PSO	
$v_{max}, \quad v_{min}$	$0.2(x_{max} - x_{min}), \quad -v_{max}$
$c_{1max}, \quad c_{1min}$	2.05, 0.5
$c_{2max}, \quad c_{2min}$	2.05, 0.5
$\omega_{max}, \quad \omega_{min}$	0.9, 0.1
$K, \quad M, \quad G$	5, 3, 5
Parameters of GA	
$pc_{max}, \quad pc_{min}$	0.6, 0.9
$pm_{max}, \quad pm_{min}$	0.01, 0.1
$\alpha, \quad \beta, \quad \mathcal{T}$	0.1, 0.1, 3
Population	
$P_i, \quad P_f$	100, 10
n_e	5
T	100
Local Search Parameters	
$L_i, \quad L_f$	5, 15
$m_{max}, \quad m_{min}$	20, 5

where L_i and L_f are initial and final iterations.

To further enhance adaptability, the number of local search steps m is dynamically adjusted based on the stagnation counter ξ_g and a predefined threshold θ_g, following this rule:

$$m = \begin{cases} \max(m_{min},\, m-1) & \text{if } \xi_g \geq \theta_g, \\ \min(m_{max},\, m+1) & \text{otherwise.} \end{cases}$$

Every m iterations (i.e., when $\mod(k, m) = 0$), the global best particle $g^{(k)}$ is perturbed by an increment $\Delta g^{(k)}$ to form a candidate solution as:

$$g_f^{(k)} = \begin{cases} g^{(k)} + \Delta g^{(k)}, & \text{if} \quad \mod(k, m) = 0, \\ g^{(k)}, & \text{otherwise.} \end{cases}$$

The candidate $g_f^{(k)}$ is accepted as the new global best if it yields a lower fitness value, that is:

$$g_f^{(k+1)} = \begin{cases} g_f^{(k)} & \text{if } J(g_f^{(k)}) \leq J(g^{(k)}), \\ g^{(k)} & \text{otherwise.} \end{cases} \tag{5.22}$$

This adaptive fine-tuning strategy strengthens the optimization process by dynamically modifying the local search frequency and updating the global best, thereby improving the algorithm's responsiveness to stagnation and enhancing convergence efficiency.

5.4 Results and Discussions

This section presents the performance evaluation of the proposed AHPEGA for optimizing MLPCs in VSC-based islanded MG. The simulation studies were conducted using MATLAB/Simulink 2024a, with all core algorithms implemented in MATLAB script files (.m).

The initial evaluation was performed on the test system depicted in Fig. 5.1. To further validate the scalability and robustness of the MLPC strategy, it was also applied to a more complex microgrid configuration comprising four VSCs connected in parallel to a common load at the PCC, as shown in Fig. 5.11. Detailed system specifications and controller parameters are outlined in Chapter 4, Section 4.6. To ensure a rigorous assessment, each control approach was tested under a variety of disturbance scenarios.comprehensively assess its performance.

5.4.1 Performance Evaluation of AHPEGA in Optimizing MLPCs

To thoroughly assess the effectiveness of AHPEGA in optimizing MLPCs, we conducted a series of controlled simulation experiments. The performance of AHPEGA was compared against several well-established algorithms, including GA [146], PSO [94], SGA [147], GA-PSO [148], GA/PSO [149], and PGPHEA [150], all under single-objective optimization conditions.

Due to the stochastic nature of metaheuristic algorithms, each was executed 20 times per optimization scenario to enhance statistical robustness. A maximum of 100 iterations per run was imposed to ensure comparability across all methods. To rigorously evaluate the performance of the proposed AHPEGA algorithm against benchmark approaches, a series of statistical analyses was conducted using the MSE objective function values from the 20 independent runs for both current and voltage controllers. The evaluation includes descriptive statistics (Table 5.2), paired t-tests (Table 5.3), and effect size calculations using Cohen's d (Table 5.4).

The descriptive statistics in Table 5.2 indicate that AHPEGA consistently yields the lowest mean MSE among all compared algorithms. For the current controller, it achieves a mean MSE of 0.000642 with a standard deviation of 0.000134 and a narrow 95% confidence interval (CI) of [0.000579, 0.000705], reflecting both high accuracy and stable performance across runs.

In contrast, other methods such as GA, PSO, and GA-PSO exhibit higher mean errors and greater variability. A similar trend is observed for the voltage controller, where AHPEGA

Table 5.2: Descriptive statistics of MSE values for each algorithm over 20 independent runs.

Current Controller			
Algorithm	**Mean**	**Std Dev**	**95% CI**
AHPEGA	0.000642	0.000134	[0.000579, 0.000705]
GA	0.006457	0.000972	[0.006002, 0.006912]
PSO	0.002800	0.000443	[0.002593, 0.003008]
SGA	0.000788	0.000170	[0.000708, 0.000868]
GA-PSO	0.003009	0.000620	[0.002719, 0.003299]
GA/PSO	0.001546	0.000282	[0.001414, 0.001678]
PGPHEA	0.000797	0.000135	[0.000734, 0.000860]
Voltage Controller			
AHPEGA	0.015506	0.000700	[0.015100, 0.015912]
GA	0.020500	0.001800	[0.019700, 0.021300]
PSO	0.019100	0.001500	[0.018400, 0.019800]
SGA	0.017800	0.001300	[0.017200, 0.018400]
GA-PSO	0.018900	0.001600	[0.018100, 0.019600]
GA/PSO	0.018800	0.001500	[0.018100, 0.019400]
PGPHEA	0.017400	0.001100	[0.016900, 0.017900]

Table 5.3: Paired t-test Results Comparing AHPEGA with Other Algorithms.

Current Controller			
Comparison	**p-value**	**Comparison**	**p-value**
AHPEGA vs GA	$< 10^{-6}$	AHPEGA vs PSO	$< 10^{-6}$
AHPEGA vs SGA	0.004661	AHPEGA vs GA-PSO	$< 10^{-6}$
AHPEGA vs GA/PSO	$< 10^{-6}$	AHPEGA vs PGPHEA	0.004115
Voltage Controller			
AHPEGA vs GA	0.0000	AHPEGA vs PSO	0.0000
AHPEGA vs SGA	0.0008	AHPEGA vs GA-PSO	0.0000
AHPEGA vs GA/PSO	0.0000	AHPEGA vs PGPHEA	0.0022

Table 5.4: Effect Size Estimates (Cohen's d) for Pairwise Comparisons Between AHPEGA and Competing Algorithms.

Current Controller		
Comparison	**Cohen's d**	**Interpretation**
AHPEGA vs GA	8.385	Huge effect size
AHPEGA vs PSO	6.591	Huge effect size
AHPEGA vs SGA	0.952	Large effect size
AHPEGA vs GA-PSO	5.281	Huge effect size
AHPEGA vs GA/PSO	4.101	Huge effect size
AHPEGA vs PGPHEA	1.154	Large effect size
Voltage Controller		
GA vs AHPEGA	3.079	Huge effect size
PSO vs AHPEGA	2.227	Huge effect size
SGA vs AHPEGA	1.349	Large effect size
GA-PSO vs AHPEGA	1.999	Huge effect size
GA/PSO vs AHPEGA	2.077	Huge effect size
PGPHEA vs AHPEGA	1.103	Large effect size

again records the lowest mean MSE of 0.015506 and the smallest standard deviation (0.000700), underscoring its consistent and superior control capability.

To statistically validate the performance advantage of AHPEGA observed in the descriptive statistics, paired t-tests were conducted, as presented in Table 5.3. The resulting p-values for all comparisons between AHPEGA and the benchmark algorithms are below 0.01, with many reaching values smaller than 10^{-6}. These low p-values strongly indicate that the differences in mean MSE are not attributable to random fluctuations. Even for algorithms such as SGA and PGPHEA, which demonstrate comparatively closer performance to AHPEGA, the statistical tests confirm that the observed improvements remain significant.

To assess the practical relevance of the observed performance differences, effect sizes were calculated using Cohen's d, as reported in Table 5.4. While Cohen's conventional thresholds—small (0.2), medium (0.5), and large (0.8) [151]—are widely used, Sawilowsky's extended classification [152] offers finer granularity more suitable for computational studies. This extended scale includes very small (0.01), small (0.20), medium (0.50), large (0.80), very large

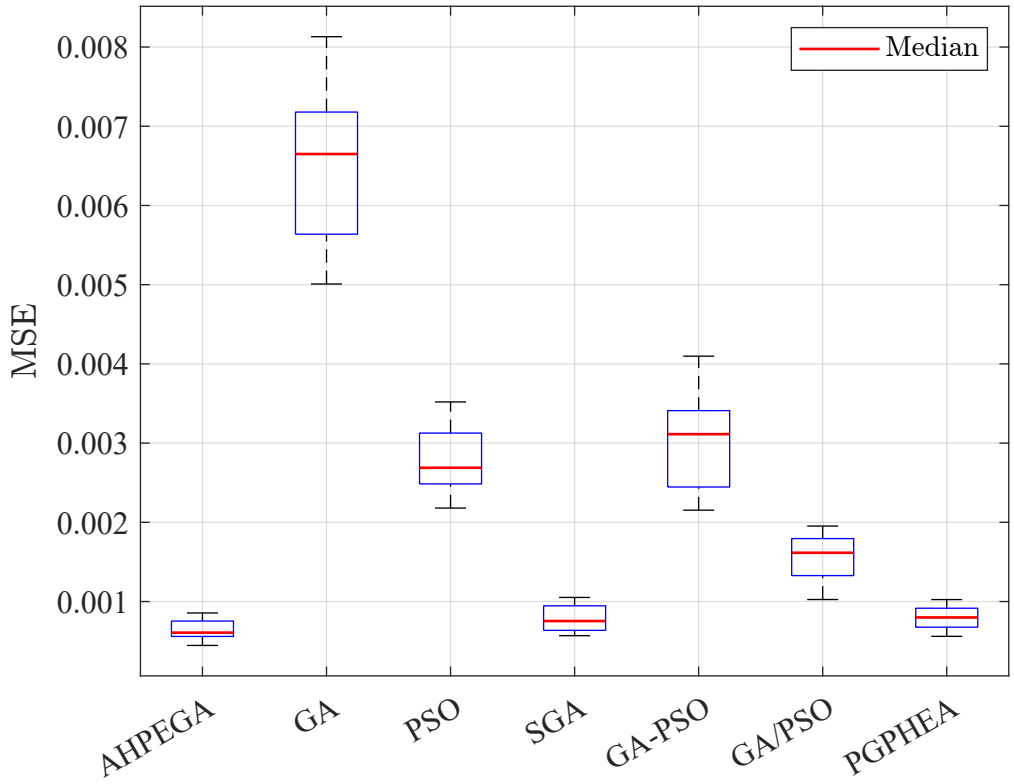

Fig. 5.6: Box plot of MSE values across 20 runs per algorithm, showing the optimization performance for the current controller.

(1.20), and huge (2.00) effect sizes, and has been increasingly adopted in the evolutionary computation literature [153]–[156] to capture the substantial variations often observed in stochastic algorithm performance.

Following this refined framework, the results demonstrate that AHPEGA consistently achieves effect sizes in the large to huge range across both controllers. For the current controller, Cohen's d values range from 0.952 to 8.385 when compared with other algorithms, underscoring the strong practical advantage of AHPEGA. In the voltage controller case, all effect sizes exceed 1.0, with several surpassing 2.0 and even 3.0, further confirming that the improvements delivered by AHPEGA are not only statistically significant but also of substantial practical significance.

Figs. 5.6 and 5.7 present box plots illustrating the distribution of MSE values over 20 independent runs for each algorithm, corresponding to the current and voltage controller optimization tasks, respectively. These visual summaries provide insights into the consistency, variability, and robustness of each algorithm's performance.

For the current controller (Fig. 5.6), AHPEGA achieves the best performance, characterized by the lowest median MSE and a compact box plot—indicating minimal variability and high

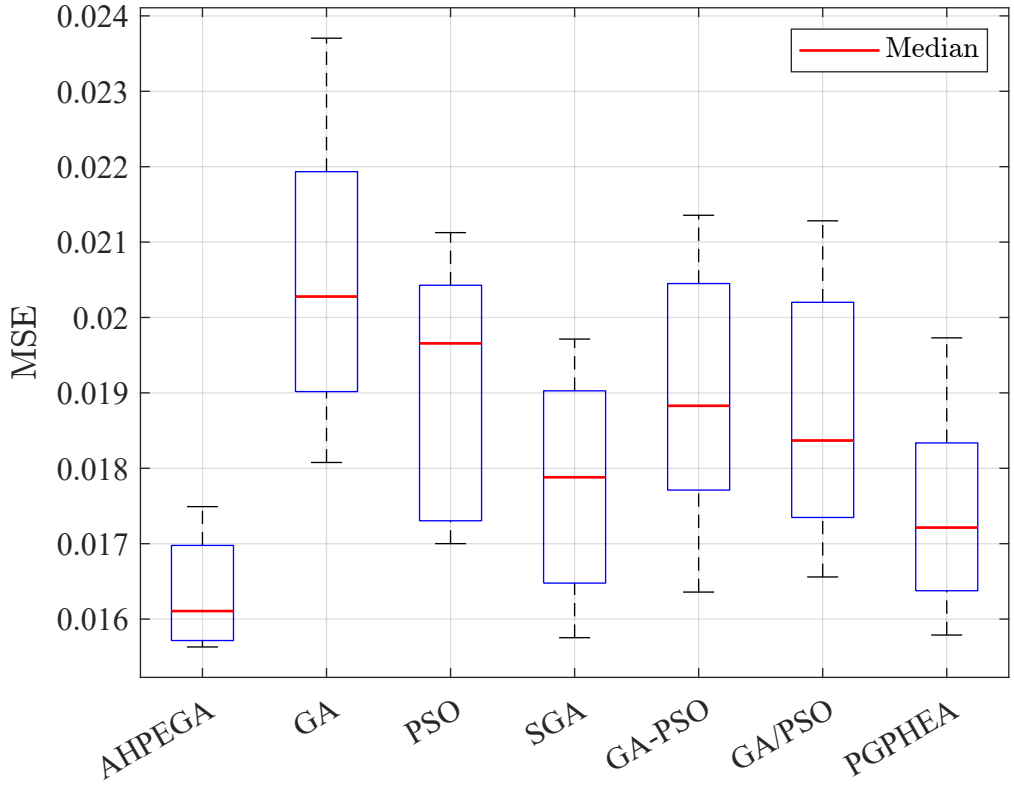

Figure 5.7: Box plot of MSE values across 20 runs per algorithm, showing the optimization performance for the voltage controller.

consistency across runs. In contrast, GA shows the highest median MSE, along with a wide interquartile range and long whiskers, reflecting significant variability. PSO and GA-PSO present higher median MSEs and broader spreads than AHPEGA, suggesting less stable optimization behavior. GA/PSO also underperforms, with elevated central values and dispersed outcomes. While SGA and PGPHEA achieve relatively lower medians compared to most algorithms, they still fall short of AHPEGA's, and their distributions remain wider, indicating greater variability.

A similar pattern emerges in the voltage controller case (Fig. 5.7). Although variability is slightly higher across all methods, AHPEGA again achieves the lowest median MSE and the most compact distribution—indicating consistently robust performance. GA continues to exhibit the poorest results, with the highest median and broadest spread. PSO and GA-PSO present higher medians and broad distributions, indicating inconsistent outcomes. GA/PSO demonstrates intermediate performance but remains clearly less effective than AHPEGA. SGA and PGPHEA show improved reliability compared to most alternatives, but AHPEGA maintains clear superiority in both median performance and distribution tightness.

Table 5.6 presents the optimal performance metrics obtained by each of the seven algorithms

over 20 independent runs, each conducted for 100 iterations. For each algorithm, the best-performing run—defined as the one yielding the lowest objective function value (MSE)—was selected to represent its peak capability. This approach highlights the maximum potential of each method under ideal conditions and complements the broader statistical analysis by focusing on best-case performance. The evaluation includes a comprehensive set of metrics—MSE, RMSE, NMSE, MAE, R^2, R, and convergence speed—providing an in-depth view of both the accuracy and efficiency of each algorithm in optimizing MLPCs for current and voltage controller design.

As shown in Table 5.5, the optimized neural network structures for each algorithm are presented, focusing on the number of neurons in each hidden layer for both the current and voltage controllers. Although all algorithms explore the same range of neurons (from 2 to 20), their optimal configurations differ, highlighting variations in their optimization capabilities. The results in Table 5.6 further demonstrate that AHPEGA consistently outperforms the other algorithms, achieving the lowest error metrics and the highest fit indices for both the current and voltage controllers.

For the current controller, AHPEGA significantly outperforms the other algorithms. It achieves the lowest MSE (0.000438), NMSE (0.004305), RMSE (0.020933), and MAE (0.012371), along with the highest R^2 (0.995695) and Pearson correlation coefficient R (0.998054). These results demonstrate that AHPEGA provides a notably superior fit, accurately capturing the underlying dynamics of the current controller compared to GA, PSO, SGA, GA-PSO, GA/PSO,

Table 5.5: Optimization results for the number of neurons in hidden layers.

Current Controller					
Algorithm	$\mathbf{n}_{min}$	$\mathbf{n}_{max}$	$\mathbf{H}_{L1}$	$\mathbf{H}_{L2}$	$\mathbf{H}_{L3}$
GA	2	20	11	8	5
PSO	2	20	13	12	8
SGA	2	20	8	11	14
GA-PSO	2	20	11	5	12
GA/PSO	2	20	16	10	8
PGPHEA	2	20	11	9	12
AHPEGA	2	20	6	8	11
Voltage Controller					
GA	2	20	7	14	12
PSO	2	20	14	5	13
SGA	2	20	16	9	8
GA-PSO	2	20	16	5	7
GA/PSO	2	20	8	6	6
PGPHEA	2	20	11	9	7
AHPEGA	2	20	17	9	8

Table 5.6: Performance metrics of various evolutionary algorithms for optimizing MLPCs.

Current Controller						
Algorithm	**MSE**	**NMSE**	**RMSE**	**MAE**	**R^2**	**R**
GA	0.004639	0.039107	0.068107	0.049025	0.960893	0.980265
PSO	0.001827	0.015406	0.042748	0.029855	0.984594	0.992908
SGA	0.000539	0.004543	0.023214	0.014689	0.995457	0.997726
GA-PSO	0.002063	0.017390	0.045417	0.033013	0.982610	0.991381
GA/PSO	0.001016	0.008564	0.031871	0.022198	0.991436	0.995733
PGPHEA	0.000527	0.004446	0.022965	0.013657	0.995554	0.997795
AHPEGA	0.000438	0.004305	0.020933	0.012371	0.995695	0.998054
Voltage Controller						
GA	0.018075	0.130635	0.134443	0.094272	0.869365	0.933099
PSO	0.016787	0.121326	0.129565	0.093012	0.878674	0.938254
SGA	0.015583	0.112621	0.124830	0.085794	0.887379	0.942008
GA-PSO	0.016241	0.117381	0.127441	0.088779	0.882619	0.939497
GA/PSO	0.016449	0.118884	0.128254	0.088740	0.881116	0.939051
PGPHEA	0.015774	0.114003	0.125594	0.086543	0.885997	0.941276
AHPEGA	0.015506	0.113929	0.124523	0.086053	0.887750	0.942206

and PGPHEA.

Among the evaluated algorithms, AHPEGA consistently achieves the best performance across all key metrics, demonstrating its effectiveness in optimizing the current controller. PGPHEA and SGA yield competitive results but still fall short of AHPEGA. PSO and GA-PSO exhibit moderate performance with noticeably higher error metrics, while GA records the highest error values, indicating its limited suitability for this optimization task.

When evaluating the voltage controller, all methods exhibit higher error metrics compared to the current controller. However, AHPEGA still delivers the best performance, recording the lowest error values: MSE (0.015506), NMSE (0.113929), RMSE (0.124523), and MAE (0.086053), along with the highest R^2 (0.887750) and Pearson correlation coefficient R (0.942206). These results suggest that, despite the more challenging nature of voltage regulation, AHPEGA consistently improves prediction accuracy and strengthens the linear relationship between predicted and actual outputs.

Across the comparative analysis, AHPEGA achieves the most favorable performance in voltage controller optimization, with the lowest error metrics across all scenarios. SGA and PGPHEA follow closely, demonstrating comparable results that validate their effectiveness, though they do not consistently match the precision of AHPEGA. PSO and GA-PSO exhibit moderate performance, with noticeably higher error values, while GA records the highest error metrics, indicating limited suitability for this task.

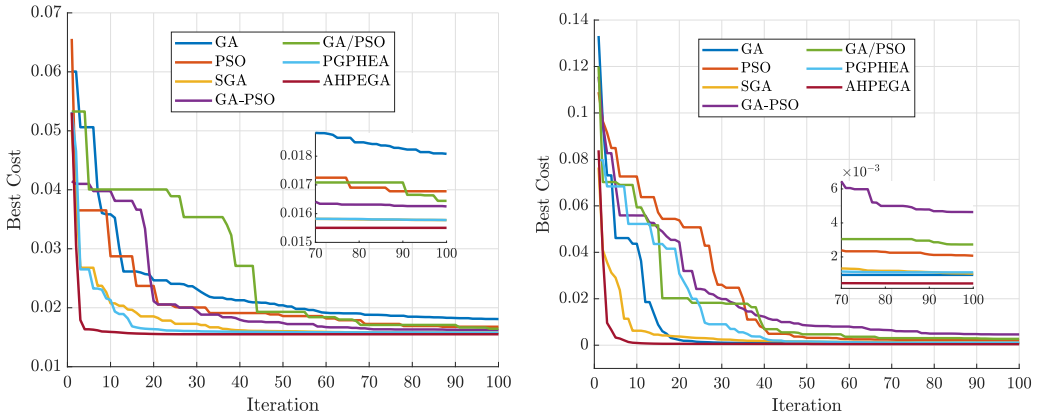

Fig. 5.8: Convergence characteristics of evolutionary algorithms for training MLPCs: (a) Voltage control convergence for MLPC. (b) Current control convergence for MLPC.

The performance of AHPEGA is evident not only in the numerical metrics but also in its convergence behavior, which is a crucial aspect of optimization algorithms. Fig. 5.8 presents a comparative analysis of the cost convergence behavior of AHPEGA alongside other algorithms, illustrating the error convergence during iterative training on the dataset.

AHPEGA's convergence curve indicates a faster progression toward the optimal solution compared to the other algorithms. The cost function converges quickly in AHPEGA, reaching the optimal solution within a few iterations, in contrast to the slower convergence of the competing algorithms. One of the key advantages of AHPEGA, as seen in the convergence curve, is its absence of sticking behavior. Unlike some algorithms that may become trapped in local minima, AHPEGA consistently progresses toward the global optimum without significant oscillations or plateaus. This stability ensures that the solutions provided are not only optimal but also reliable and repeatable. The ability to effectively explore and exploit the search space minimizes the time required to find the best solution, making AHPEGA particularly advantageous for real-world applications where computational speed is critical. The combination of rapid convergence, stability, and superior performance metrics strongly supports the adoption of AHPEGA in optimization tasks. Its consistent performance superiority across multiple metrics, coupled with its robust convergence behavior, demonstrates its effectiveness. These attributes make AHPEGA a compelling choice for both researchers and practitioners in need of reliable and efficient optimization solutions.

5.4.2 Performance Evaluation of the AHPEGA-Driven MLPCs in VSC-Based Islanded MG

Evaluation on a VSC-Based Islanded MG

To ensure the robustness of the MLPCs under extreme operating conditions, training data were collected through simulations involving severe load disturbances in the VSC system, as illustrated in Fig. 5.9. Initially, the system operates with an inductive load of (1000 + j185) kVA. To create highly dynamic conditions, several abrupt load variations are introduced: an inductive load of (250 + j100) kVA is connected at $t = 0.25$ s and disconnected at $t = 0.75$ s; subsequently, a capacitive load of (250 - j100) kVA is applied from $t = 0.75$ s to $t = 1.0$ s; and finally, a nonlinear load of 20 kW is imposed between $t = 0.75$ s and $t = 1.25$ s. These disturbances ensure that the training dataset captures a wide range of transient behaviors, enabling the neural network-based MLPCs to effectively learn and generalize the system's complex dynamics.

Following training, the model is subjected to the same sequence of violent load variations to evaluate its generalization capability under identical conditions. The comparative analysis of key performance parameters—including real and reactive power, system frequency, and

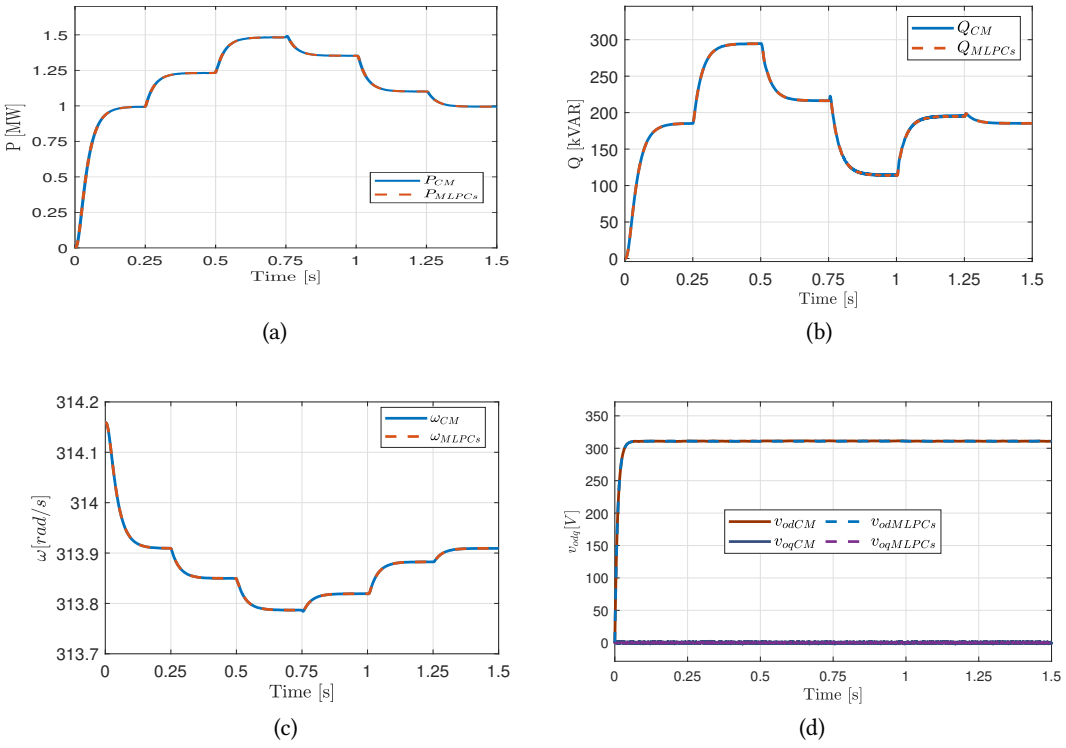

Fig. 5.9: Load variation scenarios under the conventional model and the AHPEGA-driven MLPC model: (a) Real power. (b) Reactive power. (c) Frequency. (d) dq-axis voltage.

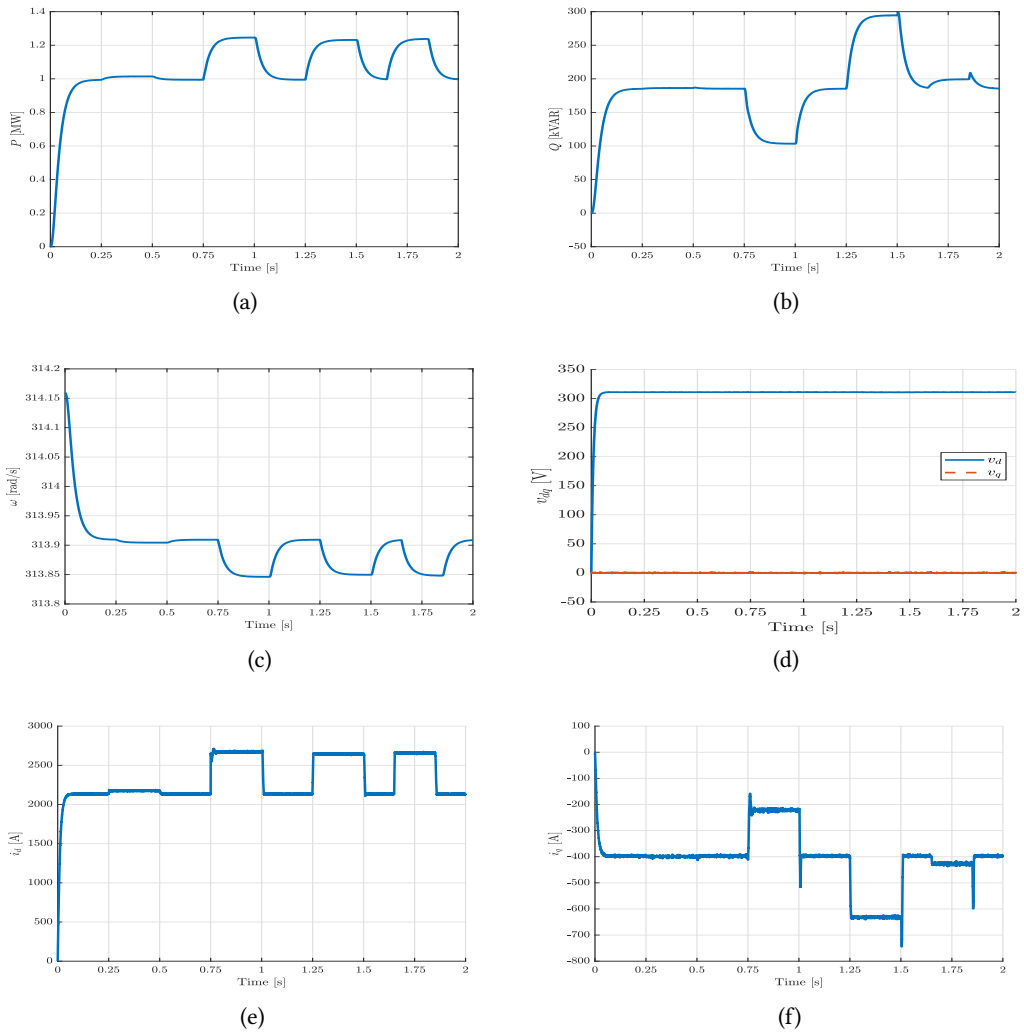

Fig. 5.10: VSC output under severe load variation scenarios with the AHPEGA-driven MLPC model: (a) Real power. (b) Reactive power. (c) VSC frequency. (d) dq-axis voltage. (e) d-axis current. (f) q-axis current.

voltage, as illustrated in Figs. 5.9a – 5.9d—demonstrates that MLPCs driven by AHPEGA precisely replicate the expected response of conventional method-based controllers (CMs). The striking alignment between the trained model's response and the system's actual behavior under disturbances validates the exceptional training quality of AHPEGA, affirming its ability to handle rapid load fluctuations with remarkable precision.

To further assess the robustness of AHPEGA-driven MLPCs beyond the original training data horizon, the simulation duration is extended to 2 s (previously 1.5 s), incorporating a new sequence of violent load variations. Specifically, a nonlinear load of 20 kW is connected at $t = 0.25$ s and disconnected at $t = 0.5$ s, followed by a capacitive load of (250 - j100) kVA, which is connected and disconnected at $t = 0.75$ s and $t = 1.0$ s, respectively. Subsequently,

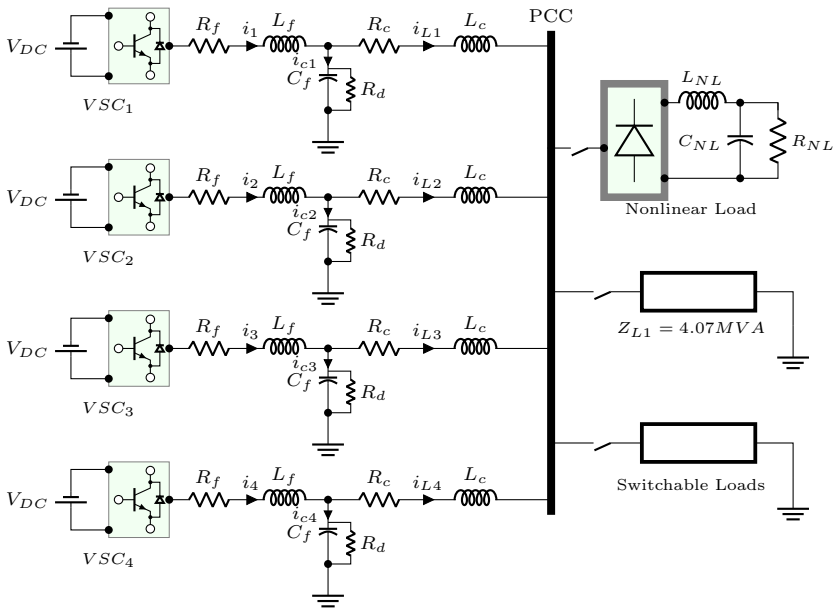

Fig. 5.11: Schematic of a multi-VSC based islanded AC MG with different loads connected at the PCC, used for the case study.

an inductive load of (250 + j100) kVA is introduced at $t = 1.25$ s and removed at $t = 1.5$ s. Finally, a resistive load of 250 kW is connected at $t = 1.65$ s and disconnected at $t = 1.85$ s, as illustrated in Fig. 5.10.

By subjecting the system to these dynamic load variations at different time intervals, the impact of rapid disturbances on MG performance is systematically assessed. The system response, including real and reactive power, voltage and frequency profiles, and d-axis and q-axis currents, is depicted in Figs. 5.10a – 5.10f. The results highlight the capability of the proposed intelligent control approach in stabilizing the MG's voltage and frequency under highly dynamic operating conditions, further demonstrating the effectiveness of AHPEGA-driven MLPCs in maintaining system stability.

Evaluation on a Multi-VSC Islanded MG

To assess the scalability and robustness of the AHPEGA-optimized MLPCs, further simulation experiments were carried out on a more realistic MG configuration, as depicted in Fig. 5.11. The setup consisted of four VSCs, each connected to a common AC bus via LCL filters and equipped with an individually trained MLPC. In this multi-VSC islanded MG, decentralized coordination is essential for accurate power-sharing and reliable operation. A droop control scheme was employed to coordinate the converters, with droop coefficients selected to yield a 0.25% voltage drop and a 0.1% frequency droop, enabling precise distribution of both active and reactive power among the units.

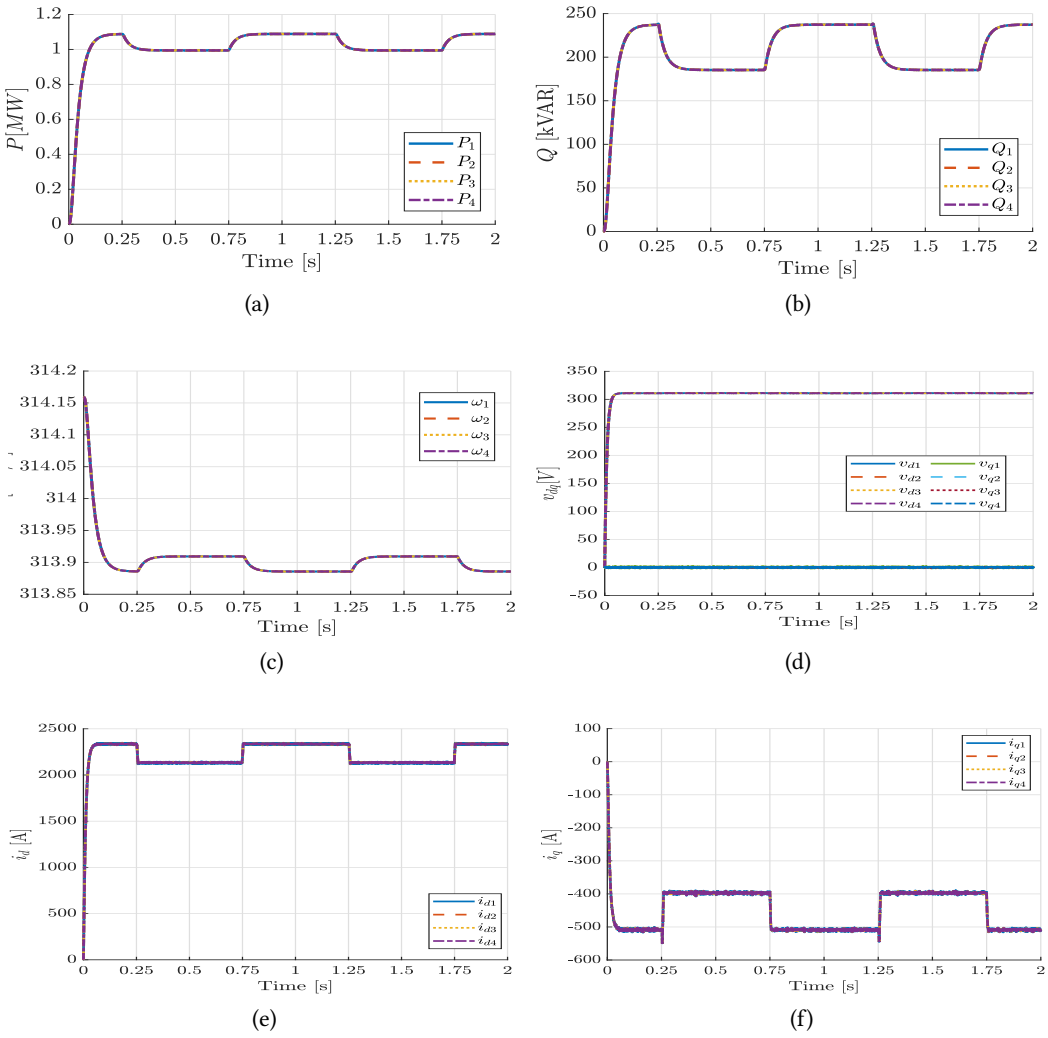

Fig. 5.12: Multi-VSC output under severe load variation scenarios with the AHPEGA-driven MLPC model: (a) Real power sharing. (b) Reactive power sharing. (c) VSC frequency synchronization. (d) dq-axis voltage sharing. (e) d-axis current sharing. (f) q-axis current sharing.

To rigorously evaluate the performance of the proposed AHPEGA-optimized MLPCs, a detailed simulation study was conducted under various load disturbance scenarios. The load profile consisted of a constant inductive base load of (4 + j0.74) MVA, a switchable inductive load of (1 + j0.1) MVA, and a nonlinear load of 20 kW. To evaluate dynamic performance and disturbance rejection, abrupt load transitions were introduced at specific intervals: the switchable loads were disconnected and reconnected at $t = 0.25$ s, $t = 0.75$ s, $t = 1.25$ s, and $t = 1.75$ s, respectively. This sequence imposed rapid changes in both active and reactive power demands, simulating real-world microgrid operating conditions.

As depicted in Fig. 5.12, the AHPEGA-driven MLPCs respond effectively to these disturbances,

maintaining stable voltage and frequency regulation across all VSC units. The controllers exhibit strong generalization capabilities, sustaining performance well beyond the conditions seen during training. Accurate power-sharing is consistently achieved, with both real and reactive power outputs from the VSCs closely aligned to their droop-based references. Following each transient, system frequency quickly re-synchronizes, and voltage magnitudes remain well within acceptable operating margins throughout the simulation, as shown in Figs. 5.10a–5.10d. Additionally, the d-axis and q-axis current components (i_d and i_q) are distributed proportionally among the VSC units in accordance with their droop settings (Figs. 5.10e, 5.10f), demonstrating the precision and coordination of the proposed control scheme.

The simulation results validate the effectiveness of AHPEGA-optimized MLPCs in managing the complex dynamics of VSC-based islanded MG. Under equal power-sharing droop control, the proposed controllers consistently maintain system stability, achieve accurate power-sharing, and deliver fast, coordinated responses—even in the presence of abrupt and severe load disturbances. These capabilities are demonstrated across multiple VSC units operating in parallel, confirming the robustness and adaptability of the control strategy under dynamic and nonlinear conditions. Notably, the AHPEGA-driven MLPCs match or exceed the performance of conventional methods while offering enhanced flexibility and scalability, making them highly suitable for real-world deployment in modern microgrid architectures. The results underscore the potential of AHPEGA as a reliable and intelligent optimization framework for training high-performance, data-driven controllers in distributed energy systems.

Chapter 6

Conclusion and Future Work

6.1 Conclusions

This thesis presents a comprehensive investigation into the optimization of operations and control strategies for DER-integrated MG, with particular emphasis on hydrogen integration, advanced control mechanisms for VSC-based islanded MG, and computationally guided optimization techniques. The study is structured around three interrelated research themes, each contributing original insights toward enhancing the efficiency, resilience, and sustainability of MG systems.

The first research focus addressed the design and optimization of MG architectures that integrate diverse DERs while ensuring long-term energy balance and cost minimization. A key innovation involved the incorporation of hydrogen-based storage and sector coupling mechanisms to bolster system flexibility, sustainability, and resilience. System-level analyses demonstrated that integrating hydrogen technologies—PEMFCs and electrolyzers—can significantly reduce carbon emissions, curtailment of renewable energy, and reliance on fossil fuels, while improving reliability during grid outages. Notably, hybrid hydrogen-battery configurations enhanced operational efficiency and extended battery lifetime by better managing state-of-charge conditions. In addition, the dual utilization of renewable-based hydrogen for both electricity generation and FCEVs enabled cross-sectoral decarbonization and introduced new revenue opportunities, reinforcing the environmental and economic value of sector coupling. These outcomes position hydrogen-integrated MGs as scalable solutions for advancing sustainable, low-carbon energy systems.

The second strand of research developed advanced control and optimization techniques for VSC-based islanded MGs. A virtual complex impedance-based control strategy was introduced to improve active and reactive power sharing accuracy, while maintaining voltage and

frequency stability under dynamic operating conditions. By shaping the converters' output impedance, the approach enhanced coordination with LCL filters and the broader electrical network. While simulation results confirmed its effectiveness in achieving stable and accurate load sharing, the strategy introduced notable structural trade-offs. The addition of an extra control loop atop conventional voltage and current controllers increased coordination complexity and computational burden, raising potential stability concerns under varying operating scenarios. If not carefully integrated with the inner control loops, the virtual impedance mechanism could lead to conflicting control actions and indirect efficiency losses—such as elevated control effort, increased switching losses, and altered dynamic responses.

To overcome these limitations, a complementary simulation-based optimization framework was proposed. This framework utilized PSO to jointly tune controller gains and LCL filter parameters, targeting improved transient performance, reduced design complexity, and greater overall efficiency. Integrated within the MATLAB/Simulink environment, the approach yielded significant enhancements—such as reduced overshoot, faster settling times, and smaller filter sizes. These findings underscore the interdependence between controller design and filter tuning, validating the use of computationally guided strategies for achieving robust and efficient in islanded MGs.

The third and final research direction focused on enhancing voltage and frequency regulation in VSC-based islanded microgrids by developing intelligent control techniques grounded in neuroevolutionary learning. To this end, a hybrid neuroevolutionary algorithm—AHPEGA—was introduced to train MLP-based controllers capable of adapting to diverse operating conditions. By integrating the global search capability of GA with the fine-tuning efficiency of PSO, while incorporating adaptive mechanisms including nonlinear inertia weighting, mutation-driven search enhancement, and dynamic population resizing. This comprehensive strategy enabled simultaneous optimization of neural network weights, biases, and hyperparameters, yielding robust generalization and fast convergence. Validated through extensive simulation, AHPEGA consistently outperformed conventional methods across key control performance metrics, establishing its potential as a high-performance, adaptable solution for intelligent control in renewable-integrated islanded MGs.

In summary, the contributions across these three research domains establish a coherent progression from system-level planning and decarbonization to device-level control innovation and intelligent optimization. The results highlight hydrogen's pivotal role in sustainable energy systems, the importance of harmonized controller and filter design in power electronic converters, and the transformative potential of neuroevolutionary methods for resilient MG control. Collectively, this work advances the frontier of distributed energy systems and lays a strong foundation for the development and deployment of intelligent, low-carbon microgrids.

6.2 Future Work

Building upon the findings of this thesis, several promising avenues for future research are identified, which can further enhance the development, operation, and intelligence of distributed energy resources integrated microgrids:

Multi-Objective and Multi-Layer Optimization Frameworks: This thesis employed single-objective optimization strategies within defined simulation environments. A natural extension is to explore multi-objective, multi-layer optimization frameworks that can simultaneously consider trade-offs between cost, emissions, reliability, and power quality. Future studies may also integrate demand-side management, market dynamics, and regulatory constraints to make such frameworks more practical and comprehensive.

Dynamic Sector Coupling with Hydrogen Infrastructure Expansion: While this work demonstrated the potential of hydrogen integration in stationary power and mobility applications, future investigations could focus on the dynamic coupling of hydrogen systems across multiple sectors. This includes modeling the coordinated operation of hydrogen production, storage, and consumption under variable renewable inputs and sectoral demands. Further exploration of hydrogen infrastructure deployment—such as the placement and operation of refueling stations in industrial parks and transport corridors—could support wider adoption.

Experimental Validation and Hardware-in-the-Loop (HIL) Implementation: All control strategies and optimization techniques proposed in this study were validated through simulation. Future work should target real-time validation using HIL platforms and experimental testbeds. This would help identify practical implementation issues such as hardware nonlinearities, communication delays, and sensor inaccuracies that are not captured in simulation environments.

Hybrid Learning-Based Controllers with Online Adaptation: Although the AHPEGA-trained controllers demonstrated strong offline performance, they do not adapt in real time. Future research may explore hybrid learning-based controllers that incorporate online or semi-online adaptation using reinforcement learning, transfer learning, or continual learning to maintain optimal performance under evolving operating conditions.

Cybersecurity and Interoperability in Intelligent Microgrids: As microgrids become more intelligent and communication-driven, addressing cybersecurity risks and ensuring interoperability among heterogeneous components will be increasingly important. Future work could focus on developing secure communication protocols, resilient control architectures, and fault-tolerant mechanisms for cyber-physical coordination.

Integration of Electric Vehicles (EVs) and Vehicle-to-Grid (V2G) Services: Complementing the hydrogen mobility framework, the coordinated integration of EVs and V2G services offers a promising avenue for further enhancing microgrid flexibility. Future studies may explore how mobile storage units can contribute to grid support functions such as peak shaving, frequency regulation, and emergency backup during outages.

References

[1] IEA, *Net zero by 2050: A roadmap for the global energy sector*, IEA, Paris. Licence: CC BY 4.0, https://www.iea.org/reports/net-zero-by-2050, 2021.

[2] Council of the European Union, *Fit for 55: Turning climate goals into law*, Council of the European Union, Brussels, https://www.consilium.europa.eu/en/policies/fit-for-55/, 2025.

[3] Y. B. Beyene, G. B. Worku, and L. B. Tjernberg, "On the design and optimization of distributed energy resources for sustainable grid-integrated microgrid in ethiopia," *International Journal of Hydrogen Energy*, 2023, https://10.1016/j.ijhydene.2023.04.192.

[4] Y. Bekele, G. Biru, and L. B. Tjernberg, "Sustainable off-grid systems with integration of renewable generation and hydrogen-fuel cell," in *2022 IEEE PES Innovative Smart Grid Technologies Conference Europe (ISGT-Europe)*, https://10.1109/ISGT-Europe54678.2022.9960622, 2022, pp. 1–5.

[5] J. J. Moreno Escobar, O. Morales Matamoros, R. Tejeida Padilla, I. Lina Reyes, and H. Quintana Espinosa, "A comprehensive review on smart grids: Challenges and opportunities," *Sensors*, vol. 21, no. 21, 2021, ISSN: 1424-8220. DOI: 10.3390/s21216978.

[6] N. Shaukat, M. R. Islam, M. M. Rahman, *et al.*, "Decentralized, democratized, and decarbonized future electric power distribution grids: A survey on the paradigm shift from the conventional power system to micro grid structures," *IEEE Access*, vol. 11, pp. 60 957–60 987, 2023. DOI: 10.1109/ACCESS.2023.3284031.

[7] S. Dorji, A. A. Stonier, G. Peter, R. Kuppusamy, and Y. Teekaraman, "An extensive critique on smart grid technologies: Recent advancements, key challenges, and future directions," *Technologies*, vol. 11, no. 3, 2023, ISSN: 2227-7080. DOI: 10.3390/technologies11030081. [Online]. Available: https://www.mdpi.com/2227-7080/11/3/81.

[8] S. Giannelos, S. Borozan, I. Konstantelos, and G. Strbac, "Option value, investment costs and deployment levels of smart grid technologies," *Sustainable Energy Research*, vol. 11, no. 1, p. 47, 2024. DOI: https://doi.org/10.1186/s40807-024-00143-x.

[9] Z. Jing, Q. Wang, Z. Chen, T. Cao, and K. Zhang, "Optimization of energy acquisition system in smart grid based on artificial intelligence and digital twin technology," *Energy Informatics*, vol. 7, no. 1, p. 121, 2024. DOI: https://doi.org/10.1186/s42162-024-00425-0.

[10] A. Hirsch, Y. Parag, and J. M. Guerrero, "Microgrids: A review of technologies, key drivers, and outstanding issues," *Renewable and Sustainable Energy Reviews*, vol. 90, pp. 402–411, 2018. DOI: 10.1016/j.rser.2018.03.040.

[11] K. Twaisan and N. Barışçı, "Integrated distributed energy resources (der) and microgrids: Modeling and optimization of ders," *Electronics*, vol. 11, no. 18, p. 2816, 2022. DOI: 10.3390/electronics11182816.

[12] S. Punitha, N. P. Subramaniam, and P. A. D. V. Raj, "A comprehensive review of microgrid challenges in architectures, mitigation approaches, and future directions," *Journal of Electrical Systems and Information Technology*, vol. 11, p. 60, 2024. [Online]. Available: https://jesit.springeropen.com/articles/10.1186/s43067-024-00188-4.

[13] S. A. M. Mousa, A. Ali, K. Mahmoud, and E. E. M. Mohamed, "Optimal operation of energy hub-based microgrids with intermittent ress and multi-type energy storage systems," *Iranian Journal of Science and Technology, Transactions of Electrical Engineering*, 2025. DOI: 10.1007/s40998-024-00779-x.

[14] P. Pachanapan, "Dynamic modelling and simulation of power electronic converter in digsilent simulation language (dsl): Islanding operation of microgrid system with multi-energy sources," in *Modelling and Simulation of Power Electronic Converter Dominated Power Systems in PowerFactory*, Springer, 2020, pp. 45–67. DOI: 10.1007/978-3-030-54124-83.

[15] E. Hernández-Mayoral, M. Madrigal-Martínez, J. D. Mina-Antonio, *et al.*, "A comprehensive review on power-quality issues, optimization techniques, and control strategies of microgrid based on renewable energy sources," *Sustainability*, vol. 15, p. 9847, 2023. [Online]. Available: https://doi.org/10.3390/su15129847.

[16] V. R. Chowdhury and A. Benato, "Microgrid and smart grid: Latest advances and prospect," *Applied Sciences*, vol. 15, p. 187, 2025. [Online]. Available: https://www.mdpi.com/journal/applsci/specialissues/W5UR40K589.

[17] N. Hatziargyriou, *Microgrids: architectures and control*. John Wiley & Sons, 2014.

[18] H. Farhangi and G. Joós, *Microgrid planning and design: a concise guide*. John Wiley & Sons, 2019.

[19] M. Roslan, M. Hannan, P. Ker, K. Muttaqi, and T. Mahlia, "Optimization algorithms for energy storage integrated microgrid performance enhancement," *Journal of Energy Storage*, vol. 43, p. 103 182, 2021, ISSN: 2352-152X. DOI: https://doi.org/10.1016/j.est.2021.103182.

[20] G. S. Thirunavukkarasu, M. Seyedmahmoudian, E. Jamei, B. Horan, S. Mekhilef, and A. Stojcevski, "Role of optimization techniques in microgrid energy management systems—a review," *Energy Strategy Reviews*, vol. 43, p. 100 899, 2022, ISSN: 2211-467X. DOI: https://doi.org/10.1016/j.esr.2022.100899.

[21] M. H. Moradi, M. Eskandari, and S. Mahdi Hosseinian, "Operational strategy optimization in an optimal sized smart microgrid," *IEEE Transactions on Smart Grid*, vol. 6, no. 3, pp. 1087–1095, 2015. DOI: 10.1109/TSG.2014.2349795.

[22] C. Gamarra and J. M. Guerrero, "Computational optimization techniques applied to microgrids planning: A review," *Renewable and Sustainable Energy Reviews*, vol. 48, pp. 413–424, 2015, ISSN: 1364-0321. DOI: https://doi.org/10.1016/j.rser.2015.04.025.

[23] M. M. Alam, M. Hossain, M. A. Habib, M. Arafat, and M. Hannan, "Artificial intelligence integrated grid systems: Technologies, potential frameworks, challenges, and research directions," *Renewable and Sustainable Energy Reviews*, vol. 211, p. 115 251, 2025, https://doi.org/10.1016/j.rser.2024.115251, ISSN: 1364-0321.

[24] A. M. Adeyinka, O. C. Esan, A. O. Ijaola, and P. K. Farayibi, "Advancements in hybrid energy storage systems for enhancing renewable energy-to-grid integration," *Sustainable Energy Research*, vol. 11, p. 26, 2024. [Online]. Available: https://sustainenergyres.springeropen.com/articles/10.1186/s40807-024-00120-4.

[25] R. Kumar, D. Lee, Ü. Ağbulut, *et al.*, "Different energy storage techniques: Recent advancements, applications, limitations, and efficient utilization of sustainable energy," *Journal of Thermal Analysis and Calorimetry*, vol. 149, pp. 1895–1933, 2024. [Online]. Available: https://link.springer.com/article/10.1007/s10973-023-12831-9.

[26] N. Goel and N. K. Yadav, "Sustainable microgrid operations: Multi-objective hybrid optimization for combined economic emission dispatch," *Electrical Engineering*, pp. 1–14, 2025. DOI: https://doi.org/10.1007/s00202-024-02912-9.

[27] H. Shuai, X. Ai, J. Fang, W. Yao, and J. Wen, "Double deep q-learning based real-time optimization strategy for microgrids," *arXiv preprint arXiv:2107.12545*, 2021. DOI: https://doi.org/10.48550/arXiv.2107.12545.

[28] X. Ge and J. Khazaei, "Physics-informed convolutional neural network for microgrid economic dispatch," *arXiv preprint arXiv:2404.18362*, 2024. DOI: https://doi.org/10.48550/arXiv.2404.18362.

[29] K. Twaisan and N. Barışçı, "Integrated distributed energy resources (der) and microgrids: Modeling and optimization of ders," *Electronics*, vol. 11, no. 18, 2022, ISSN: 2079-9292. DOI: 10.3390/electronics11182816.

[30] M. Bilal, P. N. Bokoro, and G. Sharma, "Hybrid optimization for sustainable design and sizing of standalone microgrids integrating renewable energy, diesel generators, and battery storage with environmental considerations," *Results in Engineering*, vol. 25, p. 103 764, 2025, ISSN: 2590-1230. DOI: https://doi.org/10.1016/j.rineng.2024.103764.

[31] T. T. Ağır, Z. Aydoğmuş, and B. Alataş, "Multi-objective optimization of microgrids based on recent metaheuristic methods," *Tehnički vjesnik*, vol. 28, no. 6, pp. 1839–1848, 2021. DOI: 10.17559/TV-20200112201457.

[32] M. A. Hossain, M. J. Hossain, and J. Lu, "Survey of optimization techniques for microgrids using high penetration renewable energy," *Energies*, vol. 17, no. 15, p. 3657, 2023. DOI: https://doi.org/10.3390/en17153657.

[33] S. Ishaq, I. Khan, S. Rahman, T. Hussain, A. Iqbal, and R. M. Elavarasan, "A review on recent developments in control and optimization of micro grids," *Energy Reports*, vol. 8, pp. 4085–4103, 2022, ISSN: 2352-4847. DOI: https://doi.org/10.1016/j.egyr.2022.01.080.

[34] P. A. Cárdenas, M. Martínez, M. G. Molina, and P. E. Mercado, "Development of control techniques for ac microgrids: A critical assessment," *Sustainability*, vol. 15, no. 21, 2023, ISSN: 2071-1050. DOI: 10.3390/su152115195.

[35] Y. Sabri, N. El Kamoun, and F. Lakrami, "A survey: Centralized, decentralized, and distributed control scheme in smart grid systems," in *2019 7th Mediterranean Congress of Telecommunications (CMT)*, 2019, pp. 1–11. DOI: 10.1109/CMT.2019.8931370.

[36] S. Sen and V. Kumar, "Microgrid control: A comprehensive survey," *Annual Reviews in Control*, vol. 45, pp. 118–151, 2018, ISSN: 1367-5788. DOI: https://doi.org/10.1016/j.arcontrol.2018.04.012.

[37] F. Nawaz, E. Pashajavid, Y. Fan, and M. Batool, "A comprehensive review of the state-of-the-art of secondary control strategies for microgrids," *IEEE Access*, vol. 11, pp. 102 444–102 459, 2023. DOI: 10.1109/ACCESS.2023.3316016.

[38] K. Zuo and L. Wu, "A review of decentralized and distributed control approaches for islanded microgrids: Novel designs, current trends, and emerging challenges," *The Electricity Journal*, vol. 35, no. 5, p. 107 138, 2022, Behind the meter strategies for enhancing the electricity grid resilience, reliability, economics, sustainability, and security, ISSN: 1040-6190. DOI: https://doi.org/10.1016/j.tej.2022.107138.

[39] L. B. Tjernberg and H. Shafique, "The flexible grid infrastructure enabling power grid evolution and decarbonization," in *Handbook on Climate Change and Technology*, https://doi.org/10.4337/9781800882119.00030, Edward Elgar Publishing, 2023, pp. 274–290.

[40] I. R. E. Agency, "Sector coupling in facilitating integration of variable renewable energy in cities," IRENA, 2021, Supported by SECTOR COUPLING IN FACILITATING INTEGRATION OF VARIABLE RENEWABLE ENERGY IN CITIES. [Online]. Available: https://www.irena.org/publications/2021/Oct/Sector-Coupling-in-Cities.

[41] T. Elmfeldt, Y. Arafat, L. B. Tjernberg, A. Lugnet, and G. Nyström, "Sector-coupling green hydrogen to electrify steel production – a case study at ovako hofors," in *2024 18th International Conference on Probabilistic Methods Applied to Power Systems (PMAPS)*, 2024, pp. 1–6. DOI: 10.1109/PMAPS61648.2024.10667107.

[42] F. Superchi, A. Mati, C. Carcasci, and A. Bianchini, "Techno-economic analysis of wind-powered green hydrogen production to facilitate the decarbonization of hard-to-abate sectors: A case study on steelmaking," *Applied Energy*, vol. 342, p. 121 198, 2023, ISSN: 0306-2619. DOI: https://doi.org/10.1016/j.apenergy.2023.121198.

[43] G. Bekele and B. Palm, "Feasibility study for a standalone solar–wind-based hybrid energy system for application in ethiopia," *Applied Energy*, vol. 87, no. 2, pp. 487–495, 2010, http://doi.org/10.1016/j.apenergy.2009.06.006, ISSN: 0306-2619.

[44] EEU. (2021), [Online]. Available: http://www.ethiopianelectricutility.gov.et/ (visited on 09/30/2021).

[45] M. S. Islam, "A techno-economic feasibility analysis of hybrid renewable energy supply options for a grid-connected large office building in southeastern part of france," *Sustainable Cities and Society*, vol. 38, pp. 492–508, 2018, http://doi.org/10.1016/j.scs.2018.01.022, ISSN: 2210-6707.

[46] N. Mukisa, R. Zamora, and T. T. Lie, "Feasibility assessment of grid-tied rooftop solar photovoltaic systems for industrial sector application in uganda," *Sustainable Energy Technologies and Assessments*, vol. 32, pp. 83–91, 2019, http://doi.org/10.1016/j.seta.2019.02.001, ISSN: 2213-1388.

[47] T. M. Azerefegn, R. Bhandari, and A. V. Ramayya, "Techno-economic analysis of grid-integrated pv/wind systems for electricity reliability enhancement in ethiopian industrial park," *Sustainable Cities and Society*, vol. 53, p. 101 915, 2020, https://doi.org/10.1016/j.scs.2019.101915, ISSN: 2210-6707.

[48] G. Bekele and B. Palm, "Wind energy potential assessment at four typical locations in ethiopia," *Applied Energy*, vol. 86, no. 3, pp. 388–396, 2009, http://doi.org/10.1016/j.apenergy.2008.05.012, ISSN: 0306-2619.

[49] M. Gökçek and C. Kale, "Optimal design of a hydrogen refuelling station (hrfs) powered by hybrid power system," *Energy Conversion and Management*, vol. 161, pp. 215–224, 2018, https://doi.org/10.1016/j.enconman.2018.02.007.

[50] M. Reuß, T. Grube, M. Robinius, and D. Stolten, "A hydrogen supply chain with spatial resolution: Comparative analysis of infrastructure technologies in germany," *Applied Energy*, vol. 247, pp. 438–453, 2019, https://doi.org/10.1016/j.apenergy.2019.04.064.

[51] M. R. Akhtari and M. Baneshi, "Techno-economic assessment and optimization of a hybrid renewable co-supply of electricity, heat and hydrogen system to enhance performance by recovering excess electricity for a large energy consumer," *Energy Conversion and Management*, vol. 188, pp. 131–141, 2019, https://doi.org/10.1016/j.enconman.2019.03.067.

[52] P. Alikhani, A. Mrad, H. Louie, and L. B. Tjernberg, "On the reliability and life cycle cost analyses of small-scale standalone solar systems in rural areas," in *2021 IEEE Power & Energy Society Innovative Smart Grid Technologies Conference (ISGT)*, http://doi.org/10.1109/ISGT49243.2021.9372190, 2021, pp. 1–5.

[53] J. A. Duffie, W. A. Beckman, and N. Blair, "Available solar radiation," in *Solar Engineering of Thermal Processes, Photovoltaics and Wind*. John Wiley & Sons, Ltd, 2020, ch. 2, pp. 45–140, https://doi.org/10.1002/9781119540328.ch2, ISBN: 9781119540328.

[54] N. R. E. Laboratory. (2022), [Online]. Available: https://www.homerenergy.com/products/pro/docs/3.14/index.html (visited on 09/30/2022).

[55] D. N. Luta and A. K. Raji, "Decision-making between a grid extension and a rural renewable off-grid system with hydrogen generation," *International journal of hydrogen Energy*, vol. 43, no. 20, pp. 9535–9548, 2018, https://doi.org/10.1016/j.ijhydene.2018.04.032.

[56] T. Lambert, P. Gilman, and P. Lilienthal, "Micropower system modeling with homer," *Integration of alternative sources of energy*, vol. 1, no. 1, pp. 379–385, 2006, https://doi.org/10.1002/0471755621.ch15.

[57] D. N. Luta and A. K. Raji, "Optimal sizing of hybrid fuel cell-supercapacitor storage system for off-grid renewable applications," *Energy*, vol. 166, pp. 530–540, 2019, https://doi.org/10.1016/j.energy.2018.10.070.

[58] T. Ayodele, T. Mosetlhe, A. Yusuff, and M. Ntombela, "Optimal design of wind-powered hydrogen refuelling station for some selected cities of south africa," *International Journal of Hydrogen Energy*, vol. 46, no. 49, pp. 24 919–24 930, 2021, https://doi.org/10.1016/j.ijhydene.2021.05.059.

[59] S. H. Siyal, D. Mentis, and M. Howells, "Economic analysis of standalone wind-powered hydrogen refueling stations for road transport at selected sites in sweden," *International Journal of Hydrogen Energy*, vol. 40, no. 32, pp. 9855–9865, 2015, https://doi.org/10.1016/j.ijhydene.2015.05.021.

[60] O. Guerra, M. K. Patel, and P. Mancarella, "Techno-economic and business case assessment of multi-energy microgrids with electrolysers," *Applied Energy*, vol. 240, pp. 258–272, 2019. DOI: 10.1016/j.apenergy.2019.01.135.

[61] D. Krishnamurthy, W. Cole, and J. Cochran, "Optimal operation of electrolyzers in hydrogen-based microgrids," *Renewable Energy*, vol. 168, pp. 707–720, 2021. DOI: 10.1016/j.renene.2020.12.132.

[62] P. Luis, "Water electrolysis for hydrogen production: Current status and future trends," *Chemical Engineering Journal*, vol. 369, pp. 115–132, 2019. DOI: 10.1016/j.cej.2019.03.080.

[63] M. Schalenbach, G. Tjarks, M. Carmo, W. Lueke, and D. Stolten, "Hydrogen diffusion through polymer electrolyte membranes: Measurement and modeling," *Journal of Power Sources*, vol. 352, pp. 57–66, 2016. DOI: 10.1016/j.jpowsour.2016.03.097.

[64] M. David, S. Hossain, and P. Klein, "Hydrogen as an energy storage solution for renewable energy integration: A review," *International Journal of Hydrogen Energy*, vol. 46, no. 5, pp. 3016–3034, 2021. DOI: 10.1016/j.ijhydene.2020.10.256.

[65] K. Zeng and D. Zhang, "Recent progress in alkaline water electrolysis for hydrogen production and applications," *Progress in Energy and Combustion Science*, vol. 36, no. 3, pp. 307–326, 2010. DOI: 10.1016/j.pecs.2009.11.002.

[66] M. Ni, M. K. Leung, D. Y. Leung, and K. Sumathy, "A review and recent developments in photocatalytic water-splitting using tio2 for hydrogen production," *Renewable and Sustainable Energy Reviews*, vol. 17, pp. 537–549, 2018. DOI: 10.1016/j.rser.2011.06.029.

[67] A. Vezzini, *Hydrogen and Fuel Cells: A Comprehensive Guide*. Springer, 2020. DOI: 10.1007/978-3-030-37673-8.

[68] M. Ozturk, L. Yuksek, and U. Alkan, "The role of hydrogen energy in decarbonization: A comprehensive review," *Energy Reports*, vol. 8, pp. 1534–1556, 2022. DOI: 10.1016/j.egyr.2022.10.031.

[69] D. S. Koussa and M. Koussa, "A feasibility and cost benefit prospection of grid connected hybrid power system (wind–photovoltaic)–case study: An algerian coastal site," *Renewable and Sustainable Energy Reviews*, vol. 50, pp. 628–642, 2015, https://doi.org/10.1016/j.rser.2015.04.189.

[70] H. Shafique, D.-E. Archer, R. Eriksson, and L. B. Tjernberg, "Real-time operation model for energy management system of battery energy storage system - case study: The school of sinntorp," in *2022 17th International Conference on Probabilistic Methods Applied to Power Systems (PMAPS)*, 2022, pp. 1–6. DOI: 10.1109/PMAPS53380.2022.9810577.

[71] T. Adefarati and G. Obikoya, "Techno-economic evaluation of a grid-connected microgrid system," *International Journal of Green Energy*, vol. 16, no. 15, pp. 1497–1517, 2019, https://doi.org/10.1080/15435075.2019.1671421.

[72] H. Shafique, L. B. Tjernberg, D.-E. Archer, and S. Wingstedt, "Energy management system (ems) of battery energy storage system (bess) – providing ancillary services," in *2021 IEEE Madrid PowerTech*, 2021, pp. 1–6. DOI: 10.1109/PowerTech46648.2021.9494781.

[73] C. D. Barley and C. B. Winn, "Optimal dispatch strategy in remote hybrid power systems," *Solar Energy*, vol. 58, no. 4-6, pp. 165–179, 1996, https://doi.org/10.1016/S0038-092X(96)00087-4.

[74] A. H. Fathima and K. Palanisamy, "Optimization in microgrids with hybrid energy systems–a review," *Renewable and Sustainable Energy Reviews*, vol. 45, pp. 431–446, 2015, https://doi.org/10.1016/j.rser.2015.01.059.

[75] Y. Kalinci, A. Hepbasli, and I. Dincer, "Techno-economic analysis of a stand-alone hybrid renewable energy system with hydrogen production and storage options," *International Journal of Hydrogen Energy*, vol. 40, no. 24, pp. 7652–7664, 2015, https://doi.org/10.1016/j.ijhydene.2014.10.147.

[76] M. Agredano-Torres, M. Zhang, L. Söder, and Q. Xu, "Decentralized dynamic power sharing control for frequency regulation using hybrid hydrogen electrolyzer systems," *IEEE Transactions on Sustainable Energy*, vol. 15, no. 3, pp. 1847–1858, 2024. DOI: 10.1109/TSTE.2024.3381491.

[77] R. Cozzolino and G. Bella, "A review of electrolyzer-based systems providing grid ancillary services: Current status, market, challenges and future directions," *Frontiers in energy research*, vol. 12, p. 1 358 333, 2024, https://doi.org/10.3389/fenrg.2024.1358333.

[78] S. H. Siyal, D. Mentis, U. Mörtberg, S. R. Samo, and M. Howells, "A preliminary assessment of wind generated hydrogen production potential to reduce the gasoline fuel used in road transport sector of sweden," *International Journal of Hydrogen Energy*, vol. 40, no. 20, pp. 6501–6511, 2015, https://doi.org/10.1016/j.ijhydene.2015.03.108, ISSN: 0360-3199.

[79] SunEarthTools.com. (), [Online]. Available: https://www.sunearthtools.com/tools/CO2-emissions-calculator.php (visited on 04/09/2023).

[80] M. Mohr and F. Fuchs, "Comparison of three phase current source inverters and voltage source inverters linked with dc to dc boost converters for fuel cell generation systems," in *2005 European Conference on Power Electronics and Applications*, 2005, 10 pp.–P.10. DOI: 10.1109/EPE.2005.219458.

[81] ENTSO-E, *Voltage source converters (vsc)*, Accessed: 2025-04-05, 2024. [Online]. Available: https://www.entsoe.eu/technopedia/techsheets/voltage-source-converters-vsc/.

[82] S. A. Azmi, K. H. Ahmed, S. J. Finney, and B. W. Williams, "Comparative analysis between voltage and current source inverters in grid-connected application," in *IET Conference on Renewable Power Generation (RPG 2011)*, 2011, pp. 1–6. DOI: 10.1049/cp.2011.0138.

[83] B. M. Weedy, B. J. Cory, N. Jenkins, J. B. Ekanayake, and G. Strbac, *Electric power systems*. John Wiley & Sons, 2012.

[84] J. M. Guerrero, J. C. Vasquez, J. Matas, L. G. De Vicuña, and M. Castilla, "Hierarchical control of droop-controlled ac and dc microgrids—a general approach toward standardization," *IEEE Transactions on industrial electronics*, vol. 58, no. 1, pp. 158–172, 2010. DOI: 10.1109/TIE.2010.2066534.

[85] M. Rasheduzzaman, J. A. Mueller, and J. W. Kimball, "An accurate small-signal model of inverter-dominated islanded microgrids using dq reference frame," *IEEE Journal of Emerging and Selected Topics in Power Electronics*, vol. 2, no. 4, pp. 1070–1080, 2014, https://10.1109/JESTPE.2014.2338131.

[86] Z. Liu, J. Liu, and Y. Zhao, "A unified control strategy for three-phase inverter in distributed generation," *IEEE Transactions on power electronics*, vol. 29, no. 3, pp. 1176–1191, 2013. DOI: 10.1109/TPEL.2013.2262078.

[87] Y. B. Beyene, G. B. Worku, and L. B. Tjernberg, "On virtual complex impedance droop control of vsc-based islanded microgrids," in *2023 IEEE PES Innovative Smart Grid Technologies Europe (ISGT EUROPE)*, https://10.1109/ISGTEUROPE56780.2023.10408653, 2023, pp. 1–5.

[88] W. Yao, M. Chen, J. Matas, J. M. Guerrero, and Z.-M. Qian, "Design and analysis of the droop control method for parallel inverters considering the impact of the complex impedance on the power sharing," *IEEE Transactions on Industrial Electronics*, vol. 58, no. 2, pp. 576–588, 2010. DOI: 10.1109/TIE.2010.2046001.

[89] R. Peña-Alzola, M. Liserre, F. Blaabjerg, M. Ordonez, and Y. Yang, "Lcl-filter design for robust active damping in grid-connected converters," *IEEE Transactions on Industrial Informatics*, vol. 10, no. 4, pp. 2192–2203, 2014, https://10.1109/TII.2014.2361604.

[90] S. Jayalath and M. Hanif, "An lcl-filter design with optimum total inductance and capacitance," *IEEE Transactions on Power Electronics*, vol. 33, no. 8, pp. 6687–6698, 2018, https://10.1109/TPEL.2017.2754100.

[91] Q. Liu, L. Peng, Y. Kang, S. Tang, D. Wu, and Y. Qi, "A novel design and optimization method of an LCL filter for a shunt active power filter," *IEEE Transactions on Industrial*

Electronics, vol. 61, no. 8, pp. 4000–4010, 2014, https://10.1109/TIE.2013.2282592.

[92] P. Channegowda and V. John, "Filter optimization for grid interactive voltage source inverters," *IEEE Transactions on Industrial Electronics*, vol. 57, no. 12, pp. 4106–4114, 2010, https://10.1109/TIE.2010.2042421.

[93] K. Jalili and S. Bernet, "Design of LCL filters of active-front-end two-level voltage-source converters," *IEEE Transactions on Industrial Electronics*, vol. 56, no. 5, pp. 1674–1689, 2009, https://10.1109/TIE.2008.2011251.

[94] Y. B. Beyene, G. B. Worku, and L. B. Tjernberg, "Enhancing voltage and frequency control in islanded vsc-based microgrids: A pso-driven multilayer perceptron approach," in *2024 IEEE PES Innovative Smart Grid Technologies Europe (ISGT EUROPE)*, https://10.1109/ISGTEUROPE62998.2024.10863686, 2024, pp. 1–5.

[95] D. Pullaguram, S. Mishra, N. Senroy, and M. Mukherjee, "Design and tuning of robust fractional order controller for autonomous microgrid vsc system," *IEEE Transactions on Industry Applications*, vol. 54, no. 1, pp. 91–101, 2017. DOI: 10.1109/TIA.2017.2758755.

[96] N. Pogaku, M. Prodanovic, and T. C. Green, "Modeling, analysis and testing of autonomous operation of an inverter-based microgrid," *IEEE Transactions on Power Electronics*, vol. 22, no. 2, pp. 613–625, 2007, https://10.1109/TPEL.2006.890003.

[97] M. Liserre, F. Blaabjerg, and S. Hansen, "Design and control of an lcl-filter-based three-phase active rectifier," *IEEE Transactions on Industry Applications*, vol. 41, no. 5, pp. 1281–1291, 2005, https://10.1109/TIA.2005.853373.

[98] R. N. Beres, X. Wang, M. Liserre, F. Blaabjerg, and C. L. Bak, "A review of passive power filters for three-phase grid-connected voltage-source converters," *IEEE Journal of Emerging and Selected Topics in Power Electronics*, vol. 4, no. 1, pp. 54–69, 2016, https://10.1109/JESTPE.2015.2507203.

[99] S. K. Sahoo, A. K. Sinha, and N. Kishore, "Control techniques in ac, dc, and hybrid ac–dc microgrid: A review," *IEEE Journal of Emerging and Selected Topics in Power Electronics*, vol. 6, no. 2, pp. 738–759, 2017. DOI: 10.1109/JESTPE.2017.2786588.

[100] Q.-C. Zhong, "Robust droop controller for accurate proportional load sharing among inverters operated in parallel," *IEEE Transactions on Industrial Electronics*, vol. 60, no. 4, pp. 1281–1290, 2013, https://10.1109/TIE.2011.2146221.

[101] Q.-C. Zhong and Y. Zeng, "Universal droop control of inverters with different types of output impedance," *IEEE Access*, vol. 4, pp. 702–712, 2016, https://10.1109/ACCESS.2016.2526616.

[102] A. C. Z. de Souza and M. Castilla, *Microgrids design and implementation*. Springer, 2019.

[103] A. Yazdani and R. Iravani, *Voltage-sourced converters in power systems: modeling, control, and applications*. John Wiley & Sons, 2010.

[104] A. Yazdani, "Control of an islanded distributed energy resource unit with load compensating feed-forward," in *2008 IEEE Power and Energy Society General Meeting - Conversion and Delivery of Electrical Energy in the 21st Century*, https://10.1109/PES.2008.4595978, 2008, pp. 1–7.

[105] Y. Li and L. Fan, "Stability analysis of two parallel converters with voltage–current droop control," *IEEE Transactions on Power Delivery*, vol. 32, no. 6, pp. 2389–2397, 2017, https://10.1109/TPWRD.2017.2656062.

[106] K. Ogata and Y. Yang, *Modern control engineering*. Prentice hall India, 2002, vol. 5.

[107] IEEE, "Ieee recommended practice and requirements for harmonic control in electric power systems," *IEEE Std 519-2014 (Revision of IEEE Std 519-1992)*, pp. 1–29, 2014, https://10.1109/IEEESTD.2014.6826459.

[108] T.-F. Wu, M. Misra, L.-C. Lin, and C.-W. Hsu, "An improved resonant frequency based systematic lcl filter design method for grid-connected inverter," *IEEE Transactions on Industrial Electronics*, vol. 64, no. 8, pp. 6412–6421, 2017, https://10.1109/TIE.2017.2682004.

[109] A. A. Rockhill, M. Liserre, R. Teodorescu, and P. Rodriguez, "Grid-filter design for a multimegawatt medium-voltage voltage-source inverter," *IEEE Transactions on Industrial Electronics*, vol. 58, no. 4, pp. 1205–1217, 2011, https://10.1109/TIE.2010.2087293.

[110] Y. Jiao and F. C. Lee, "Lcl filter design and inductor current ripple analysis for a three-level npc grid interface converter," *IEEE Transactions on Power Electronics*, vol. 30, no. 9, pp. 4659–4668, 2015, https://10.1109/TPEL.2014.2361907.

[111] P. Naresh, C. Anirudh, and V. Seshadri Sravan Kumar, "Comparison of passive damping based lcl filter design methods for grid-connected voltage source converters," in *2020 International Conference on Power, Instrumentation, Control and Computing (PICC)*, https://10.1109/PICC51425.2020.9362488, 2020, pp. 1–6.

[112] A. Reznik, M. G. Simões, A. Al-Durra, and S. M. Muyeen, "LCL filter design and performance analysis for grid-interconnected systems," *IEEE Transactions on Industry Applications*, vol. 50, no. 2, pp. 1225–1232, 2014, https://10.1109/TIA.2013.2274612.

[113] R. Peña-Alzola, M. Liserre, F. Blaabjerg, R. Sebastián, J. Dannehl, and F. W. Fuchs, "Analysis of the passive damping losses in lcl-filter-based grid converters," *IEEE Transactions on Power Electronics*, vol. 28, no. 6, pp. 2642–2646, 2013, https://10.1109/TPEL.2012.2222931.

[114] D. Guha, P. K. Roy, and S. Banerjee, "Load frequency control of interconnected power system using grey wolf optimization," *Swarm and Evolutionary computation*, vol. 27, pp. 97–115, 2016, https://10.1016/j.swevo.2015.10.004.

[115] R. K. Sahu, S. Panda, and S. Padhan, "A hybrid firefly algorithm and pattern search technique for automatic generation control of multi area power systems," *International Journal of Electrical Power and Energy Systems*, vol. 64, pp. 9–23, 2015, https://10.1016/j.ijepes.2014.07.013, ISSN: 0142-0615.

[116] S. Kanwal, M. Q. Rauf, B. Khan, and G. Mokryani, "Artificial neural network assisted robust droop control of autonomous microgrid," *IET Renewable Power Generation*, vol. 18, no. 7, pp. 1346–1369, 2024, https://doi.org/10.1049/rpg2.12739.

[117] R. K. Sahu, S. Panda, and G. Chandra Sekhar, "A novel hybrid pso-ps optimized fuzzy pi controller for agc in multi area interconnected power systems," *International Journal of Electrical Power and Energy Systems*, vol. 64, pp. 880–893, 2015, https://10.1016/j.ijepes.2014.08.021, ISSN: 0142-0615.

[118] M. O. Okwu and L. K. Tartibu, *Metaheuristic optimization: Nature-inspired algorithms swarm and computational intelligence, theory and applications*. Springer Nature, 2020, vol. 927.

[119] S. Selvarajan, "A comprehensive study on modern optimization techniques for engineering applications," *Artificial Intelligence Review*, vol. 57, no. 8, p. 194, 2024, https://doi.org/10.1007/s10462-024-10829-9.

[120] D. T. Akl, M. M. Saafan, A. Y. Haikal, and E. M. El-Gendy, "Ihho: An improved harris hawks optimization algorithm for solving engineering problems," *Neural Computing and Applications*, vol. 36, no. 20, pp. 12 185–12 298, 2024, https://doi.org/10.1007/s00521-024-09603-3.

[121] M. Shehab, I. Mashal, Z. Momani, *et al.*, "Harris hawks optimization algorithm: Variants and applications," *Archives of Computational Methods in Engineering*, vol. 29, no. 7, pp. 5579–5603, 2022, https://doi.org/10.1007/s11831-022-09780-1.

[122] A. S. Assiri, "On the performance improvement of butterfly optimization approaches for global optimization and feature selection," *Plos one*, vol. 16, no. 1, e0242612, 2021, https://doi.org/10.1371/journal.pone.0242612.

[123] S. N. Makhadmeh, M. A. Al-Betar, A. K. Abasi, *et al.*, "Recent advances in butterfly optimization algorithm, its versions and applications," *Archives of Computational Methods in Engineering*, vol. 30, no. 2, pp. 1399–1420, 2023, https://doi.org/10.1007/s11831-022-09843-3.

[124] S. Bouguezzi, *Grasshopper optimization algorithm*, Accessed: 2025-03-18, 2024. [Online]. Available: https://www.baeldung.com/cs/grasshopper-optimization-algorithm.

[125] E. Zvornicanin, *Grey wolf optimization algorithm*, Accessed: 2025-03-18, 2022. [Online]. Available: https://www.baeldung.com/cs/grey-wolf-optimization.

[126] B. Bhatt, H. Sharma, K. Arora, G. P. Joshi, and B. Shrestha, "Levy flight-based improved grey wolf optimization: A solution for various engineering problems," *Mathematics*, vol. 11, no. 7, 2023, ISSN: 2227-7390. DOI: 10.3390/math11071745.

[127] Y. Liu, A. As' arry, M. K. Hassan, A. A. Hairuddin, and H. Mohamad, "Review of the grey wolf optimization algorithm: Variants and applications," *Neural Computing and Applications*, vol. 36, no. 6, pp. 2713–2735, 2024, https://doi.org/10.1007/s00521-023-09202-8.

[128] S. Katoch, S. S. Chauhan, and V. Kumar, "A review on genetic algorithm: Past, present, and future," *Multimedia tools and applications*, vol. 80, pp. 8091–8126, 2021, https://doi.org/10.1007/s11042-020-10139-6.

[129] C. Blum, "Ant colony optimization: Introduction and recent trends," *Physics of Life Reviews*, vol. 2, no. 4, pp. 353–373, 2005, https://doi.org/10.1016/j.plrev.2005.10.001, ISSN: 1571-0645.

[130] C. Blum, "Ant colony optimization: A bibliometric review," *Physics of Life Reviews*, vol. 51, pp. 87–95, 2024, https://doi.org/10.1016/j.plrev.2024.09.014, ISSN: 1571-0645.

[131] X.-S. Yang and S. Deb, "Cuckoo search: Recent advances and applications," *Neural Computing and applications*, vol. 24, pp. 169–174, 2014, https://doi.org/10.1007/s00521-013-1367-1.

[132] G. Papazoglou and P. Biskas, "Review and comparison of genetic algorithm and particle swarm optimization in the optimal power flow problem," *Energies*, vol. 16, no. 3, 2023, ISSN: 1996-1073. DOI: 10.3390/en16031152.

[133] H. Kraiem, F. Aymen, L. Yahya, A. Triviño, M. Alharthi, and S. S. M. Ghoneim, "A comparison between particle swarm and grey wolf optimization algorithms for improving the battery autonomy in a photovoltaic system," *Applied Sciences*, vol. 11, no. 16, 2021, ISSN: 2076-3417. DOI: 10.3390/app11167732.

[134] RoX818, *Particle swarm optimization vs. genetic algorithm*, Accessed: 2025-03-18, 2024. [Online]. Available: https://aicompetence.org/particle-swarm-optimization-vs-genetic-algorithm/.

[135] Y. Del Valle, G. K. Venayagamoorthy, S. Mohagheghi, J.-C. Hernandez, and R. G. Harley, "Particle swarm optimization: Basic concepts, variants and applications in

power systems," *IEEE Transactions on evolutionary computation*, vol. 12, no. 2, pp. 171–195, 2008, https://10.1109/TEVC.2007.896686.

[136] M. Hassan and M. Abido, "Optimal design of microgrids in autonomous and grid-connected modes using particle swarm optimization," *IEEE Transactions on power electronics*, vol. 26, no. 3, pp. 755–769, 2010, https://10.1109/TPEL.2010.2100101.

[137] J. Shang, J. Gao, X. Jiang, M. Liu, and D. Liu, "Optimal configuration of hybrid energy systems considering power to hydrogen and electricity-price prediction: A two-stage multi-objective bi-level framework," *Energy*, vol. 263, p. 126 023, 2023, http://doi.org/10.1016/j.energy.2022.126023, ISSN: 0360-5442.

[138] X. Hu, Z. Li, C. Pan, H. Li, and Y. Liang, "An adaptive virtual-impedance-based current-limiting method with the functionality of transient stability enhancement for grid-forming converter," *Electronics*, vol. 13, p. 2750, 14 2024, https://doi.org/10.3390/electronics13142750.

[139] A. Name, "Enhancing the small-signal stability of the island microgrids under the dynamic loading conditions," *International Journal of Low-Carbon Technologies*, 2023, https://academic.oup.com/ijlct/article/doi/10.1093/ijlct/ctaf035/8087326.

[140] M. Raeispour, H. Atrianfar, M. Davari, and G. B. Gharehpetian, "Fault-tolerant, distributed control for emerging, vsc-based, islanded microgrids—an approach based on simultaneous passive fault detection," *IEEE Access*, vol. 10, pp. 10 995–11 010, 2022, https://10.1109/ACCESS.2021.3132802.

[141] N. Chettibi, A. Mellit, G. Sulligoi, and A. Massi Pavan, "Adaptive neural network-based control of a hybrid ac/dc microgrid," *IEEE Transactions on Smart Grid*, vol. 9, no. 3, pp. 1667–1679, 2018, https://10.1109/TSG.2016.2597006.

[142] F. Hardan, R. Norman, and W. Leithead, "Model-based control of a vsc-based power generator with synthetic inertia provision in an isolated micro-grid," *IET Generation, Transmission & Distribution*, vol. 14, no. 22, pp. 5037–5046, 2020. DOI: 10.1049/iet-gtd.2020.0304.

[143] G. L. Rajora, M. A. Sanz-Bobi, L. B. Tjernberg, and J. E. Urrea Cabus, "A review of asset management using artificial intelligence-based machine learning models: Applications for the electric power and energy system," *IET Generation, Transmission & Distribution*, 2024. DOI: 10.1049/gtd2.13183.

[144] M. G. M. Abdolrasol, S. M. S. Hussain, T. S. Ustun, *et al.*, "Artificial neural networks based optimization techniques: A review," *Electronics*, vol. 10, no. 21, 2021, ISSN: 2079-9292. DOI: 10.3390/electronics10212689.

[145] T. Ansar and W. M. Ashraf, "Comparison of kolmogorov–arnold networks and multi-layer perceptron for modelling and optimisation analysis of energy systems," *Energy*

and AI, vol. 20, p. 100 473, 2025, https://doi.org/10.1016/j.egyai.2025.100473, ISSN: 2666-5468.

[146] S. Ding, C. Su, and J. Yu, "An optimizing bp neural network algorithm based on genetic algorithm," *Artificial intelligence review*, vol. 36, pp. 153–162, 2011. DOI: 10.1007/s10462-011-9208-z.

[147] P. Aivaliotis-Apostolopoulos and D. Loukidis, "Swarming genetic algorithm: A nested fully coupled hybrid of genetic algorithm and particle swarm optimization," *PLoS One*, vol. 17, no. 9, e0275094, 2022. DOI: 10.1371/journal.pone.0275094.

[148] C. Roy and D. K. Das, "A hybrid genetic algorithm (ga)–particle swarm optimization (pso) algorithm for demand side management in smart grid considering wind power for cost optimization," *Sādhanā*, vol. 46, no. 2, p. 101, 2021. DOI: 10.1007/s12046-021-01626-z.

[149] V. Shukla, V. Mukherjee, and B. Singh, "A hybrid optimization for coordinated control of distributed generations," *Engineering Applications of Artificial Intelligence*, vol. 136, p. 109 023, 2024, https://doi.org/10.1016/j.engappai.2024.109023, ISSN: 0952-1976.

[150] X. Shi, Y. Lu, C. Zhou, H. Lee, W. Lin, and Y. Liang, "Hybrid evolutionary algorithms based on pso and ga," in *The 2003 Congress on Evolutionary Computation, 2003. CEC '03.*, https://10.1109/CEC.2003.1299387, vol. 4, 2003, 2393–2399 Vol.4.

[151] J. Cohen, *Statistical Power Analysis for the Behavioral Sciences*. Routledge, 1988.

[152] S. S. Sawilowsky, *New effect size rules of thumb*. 2009, vol. 8, pp. 597–599.

[153] P. D. Ellis, *The Essential Guide to Effect Sizes: Statistical Power, Meta-analysis, and the Interpretation of Research Results*. Cambridge University Press, 2010.

[154] S. García, D. Molina, M. Lozano, and F. Herrera, "A study of statistical techniques and performance measures for genetics-based machine learning: Accuracy and interpretability," *Soft Computing*, vol. 13, no. 10, pp. 959–977, 2009.

[155] E. Zitzler, L. Thiele, M. Laumanns, C. M. Fonseca, and V. Grunert da Fonseca, "Performance assessment of multiobjective optimizers: An analysis and review," in *IEEE Transactions on Evolutionary Computation*, 2003, pp. 117–132.

[156] L. d. S. Coelho and V. C. Mariani, "Comparing metaheuristic methods for ac filter design," *IEEE Transactions on Magnetics*, vol. 45, no. 3, pp. 1600–1603, 2009.